PERMEABILITY ANALYSIS FOR THERMAL BINDER REMOVAL FROM GREEN CERAMIC BODIES

A Dissertation

Presented to

The Faculty of the Graduate School

University of Missouri-Columbia

In Partial Fulfillment

Of the Requirements for the Degree

Doctor of Philosophy

by

Jeong Woo Yun

Dr. Stephen J. Lombardo   Dissertation Supervisor

MAY 2007

The undersigned, appointed by the Dean of the Graduate School, have examined the dissertation entitled

PERMEABILITY ANALYSIS FOR THERMAL BINDER REMOVAL FROM GREEN CERAMIC BODIES

Presented by

Jeong Woo Yun

A candidate for the degree of

Doctor of Philosophy

And hereby certify that in their opinion it is worthy of acceptance

Dr. Stephen J. Lombardo   _____

Dr. Willian A. Jacoby   _____

Dr. Qingsong Yu   _____

Dr. Frank Z. Feng   _____

Dr. Sanjeev Khanna   _____

Acknowledgement

I sincerely wish to thank all people who contributed to my graduate studies in University of Missouri-Columbia. At first, I would like to express my deepest gratitude to Dr. Stephen J. Lombardo for his guidance and advice throughout my graduate study. Of the many things I learned from him, critical thinking and logical thinking made me understand the real research attitude and spirit. His advice and instruction will guide my future research and career. I would also like to thank my Doctoral Committee for their advice and effort in evaluating my work.

I would like to thank Dr. Lee for his support and advice about my life and research. His support and advice helped me to accommodate to new life as a graduate student in United State. I would also like to thank all my colleagues at University of Missouri-Columbia for emotional support and educational advice. They have provided great help and enriched my graduate studies. I thank Kuma Krishnamurthy, Matt Schurwanz, Young Jo Kim and Chang Soo Kim in Chemical Engineering Department. I also thank Suhan Chong, Duck Bong Seo, Yong Sik Lee and other Korean students.

Finally, I sincerely thank my family for their love, support, and encourage to my life.

Thank you so much.

PERMEABILITY ANALYSIS FOR THERMAL BINDER REMOVAL FROM GREEN CERAMIC BODIES

Jeong Woo Yun

Dr. Stephen J. Lombardo   Dissertation Supervisor

ABSTRACT

The permeability of ceramic green tapes influences the ceramic process steps such as binder removal in which the permeability partially controls the decomposition rate in order to avoid failure of the body, because the permeability relieves the internal pressure build up. The tapes are comprised of barium titanate as the dielectric materials, and poly(vinyl butyral) and dioctyl phthalate as the main binder mixture.

The flow though single capillary in the tape was analyzed in terms of models for describing Knudsen, slip, and Poiseuille flow as transport mechanisms.   An analytical solution was derived, and compared to an approximate solution.   The relative contributions of these three flow mechanisms were then analyzed for different ratios of the mean free path to pore size and for different pressure driving forces.

The permeability of green tapes which are unlaminated and laminated was determined as a function of binder content for binder removed by air oxidation.   The flow in porous media through the tapes was analyzed in terms of models for describing Knudsen, slip, and Poiseuille flow mechanisms. With measurement of flow, the characteristic pore size was determined to be 1-2 μm for unlaminated and 0.5-1 μm for laminated samples as a function of binder loading.   Poiseuille flow was thus the

dominant transport mechanism contributing to the flux in both the unlaminated and laminated samples and therefore Darcy's Law was used to determine the permeability. The number of tapes strongly affects to the permeability for the laminated samples. The permeability was also determined from micro-structural attributes in terms of the specific surface, the pore fraction, and terms of the specific surface, the pore fraction, and terms to account for tortuosity and constrictions.

The permeability and adhesion strength of laminated green ceramic tapes were determined. Both the flow in porous media and the adhesion strength were seen to depend on the lamination conditions of time, temperature, and pressure. The adhesion strength was seen to increase with increasing lamination conditions of time, temperature and pressure, whereas the permeability decreased.

TABLE OF CONTENTS

LIST OF TABLES

TABLE

LIST OF FIGURES

FIGURE

CHAPTER 1

GENERAL INTRODUCTION

1.1 PERMEABILITY IN THERMAL DEBINDING

Polymeric binders are widely used in both the powder metallurgy and ceramic industries, such as in the fabrication of multilayered ceramic capacitors as shown in Fig. 1.1. Such binders need to be removed from the powder compact before it is sintered into a final product. The most commonly used method of binder removal is thermolysis, or thermal debinding, which is simply the oxidation of the binder in air or the pyrolyis of binder in nitrogen. If binder removal is incomplete, the trapped polymeric residues will be a contamination source and may affect the final physical or electrical properties of the product [1,2]. If the binder removal is conducted too quickly, defects such as cracks and large voids may affect the micro-structural evolution of the component during sintering [3]. The successful removal of binder occurs without disrupting the packing of the particles or producing any defects in the green ceramic body.

BaTiO$_3$+PVB+DOP

Pt metal
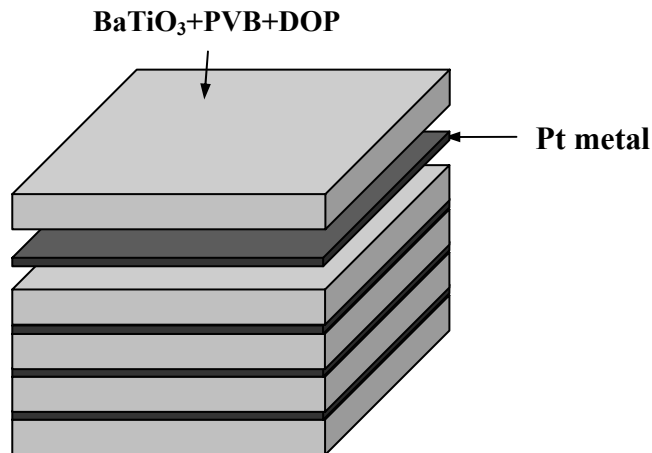
Figure 1. 1 Schematic of the ceramic green body with metal layer for the multilayer ceramic capacitor.

Thermal binder removal from green ceramic bodies is a complex process that is influenced by both chemical and physical factors, such as heat transfer, mass transfer, kinetics of binder degradation, and stress. The basic processes of binder removal include the degradation of the polymer and the transport of the degradation products to the surface through open pores in the body, which is illustrated in Fig. 1.2. The polymeric binders are likely decomposed in air to oligomers, monomers, or smaller molecules, such as CO_2 and H_2O, at high temperature. The gas phase molecules thus created are then transported to the surface through open pores in the body. If the rate of binder decomposition is faster than the rate of transport to the surface, the pressure in the pores in the green body increases, and then the resultant stress may cause body failure by blistering, cracking and delaminating, as is shown in Fig. 1.3. To avoid failure, binder removal must be done slowly and steadily. In practice, thermal binder removal takes 4~10 days, and is thus one of the most time and energy consuming steps in the fabrication of multilayer ceramic capacitors.
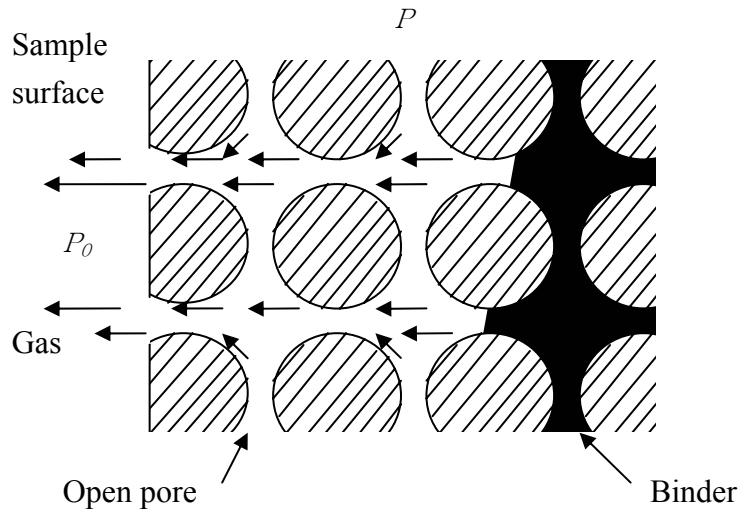
Figure 1. 2 Schematic diagram of thermal binder removal from the ceramic green body. The decomposed gas-phase products flow through the open pores

(a)
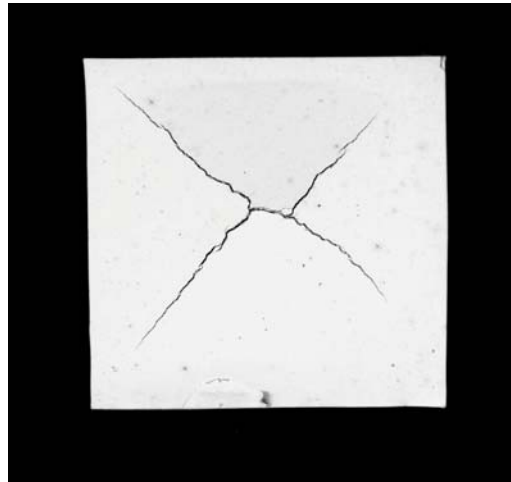
(b)
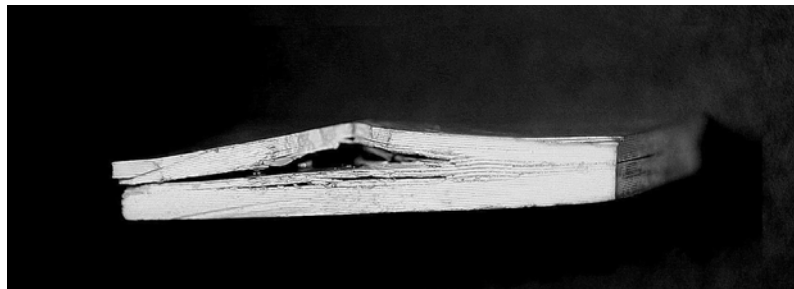
(c)
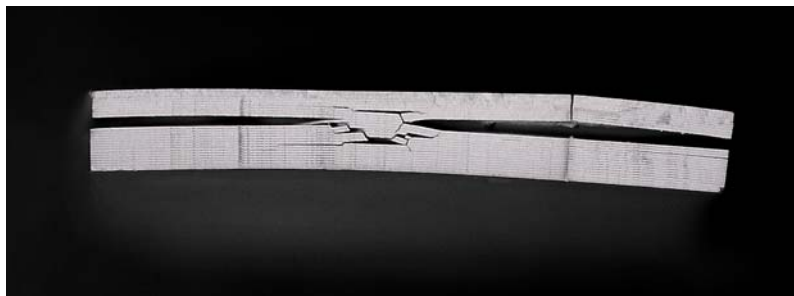
(d)

Figure 1. 3   Photos of binder removal failure in multilayer ceramic capacitors. The samples are failed by delaminating (a, d) and bloating (b, c).

A number of models have been developed in the literature to describe the thermal removal of binder from fine ceramic powder compacts [4-7].   German proposed three different mechanisms in the green body for binder transport: diffusion, permeation, and wicking, and these mass transport models of binder removal were simulated with simple, 1-dimensional models.   Stangle and Aksay developed a theoretical model to describe the simultaneous momentum, heat, and mass transfer phenomena in porous media.   This model, however, has a large number of input data which are usually difficult to obtain. Calvert and Cima proposed a model to predict the kinetics of binder removal for a polymer which degrades by unzipping.   This model, unfortunately, did not take into consideration the effect of volume expansion from solid phase binder to gas phase products due to pyrolysis, which is the major phenomena occurring during thermal debinding.

In earlier work, we have analyzed and modeled the kinetic parameters of binder degradation during thermal binder removal with TGA and DSC [8,9].   We then derived an analytical solution to the pressure driven flow problem for 3-D bodies [10,11,12]. The model can treat anisotropic permeability within the green body, which has been observed in multilayer ceramic capacitors where the binder product gases flow preferentially parallel to the metal layers.   We also have analyzed the heat transfer in porous green bodies during binder removal.   Based on these kinetic, heat transfer, and mass transfer analyses, approximate analytical equations have been derived for the minimum time heating cycle for binder removal from porous green bodies [13-16]. These analytical equations can be applied in practice to real ceramic green bodies.

The equations for predicting the minimum time heating cycle during thermal

debinding, however, were derived for a theoretical permeability model, namely the Kozeny-Carmen equation, which may not rigorously agree to the permeability evolution during thermal debinding for multilayered ceramic capacitors. It is thus the major aim of this work to determine how the permeability varies with binder content during thermal debinding, as the permeability may strongly control the heating rate of the sample in order to avoid failure of the body. The permeability varies with time, because the loss of binder may be expected to increase the porosity and to change the surface area per unit volume.

In addition to the role the permeability plays during thermal debinding, lamination of the single tapes is a necessary process to get sufficient strength to maintain the green body. Lamination, however, also leads to decrease in the permeability and as a result of that, the binder removal time increases. Therefore less aggressive lamination conditions, which mean less pressure, lower temperature, or shorter time, are preferred to reduce the cycle time without sacrificing interlayer adhesion.

In this thesis, we analyze different flux mechanisms in porous media in order to obtain a measure of the permeability. As part of this analysis, we also determine the pore size as a function of binder loading. Finally, we examine the effects of lamination time, temperature, and pressure on the permeability and adhesion strength of green ceramic tapes.

1.2   THESIS ORGANIZATION

In chapter 2, the flow of gases in narrow capillaries was simulated for different contributions from Knudsen, Poiseuille, and slip flow mechanisms.   An analytical solution was derived, and compared to an approximate solution presented by others. The relative contributions of these three flow mechanisms to the overall flux were then analyzed for different ratios of the mean free path to pore size and for different pressure drop driving forces.

In chapter 3, the permeability of unlaminated green tapes was determined as a function of binder content for binder removed by air oxidation.   The tapes are comprised of barium titanate as the dielectric, and polyvinyl butyral and dioctyl phthalate are the main components of the binder mixture.   The flow in porous media through the tapes was analyzed in terms of models for describing Knudsen, slip, and Poiseuille flow mechanisms.

In chapter 4, the permeability of laminated green ceramic tapes was determined as a function of binder loading for binder removed by air oxidation.   These tapes also consisted of barium titanate as the dielectric, and the binder consisted again primarily of poly(vinyl butyral) and dioctyl phthalate.

In Chapter 5, the permeability and adhesion strength of laminated green ceramic tapes were determined for tapes comprised of barium titanate as the dielectric, and poly(vinyl butyral) and dioctyl phthalate as the main components of the binder mixture. Both the flow in porous media and the adhesion strength were seen to depend on the lamination conditions of time, temperature, and pressure.

1.3   REFERENCES

1. S. Masia, P. D. Calvert, W. E. Rhine, and H. K. Brown, "Effect of Oxides on Binder Burnout During Ceramics Processing," *J. Mater. Sci.*, **24** 1907 (1989)

2. W. Malinowski, and A. Withop, "Organic Sources of Voids in Ceramics," *Ceram. Bull.*, **57** 523 (1978)

3. C. Dong, and H. K. Bowen, "Hot-Stage Study of Bubble Formation During Binder Burnout," *J. Am. Ceram. Soc.*, **72** 1082 (1989)

4. R. M. German, "Theory of Thermal Debinding," *Int. J. Powder. Metall.*, **23**[4] 237-245 (1987)

5. G. C. Stangle, and I. A. Aksay, "Simultaneous Momentum, Heat and Mass Transfer with Chemical Reaction in a Disordered Porous Medium: Application to Binder Removal from a Ceramic Green Body," *Chem. Eng. Sci.*, **45** 1719 (1990)

6. P. Calvert and M. J. Cima, "Theoretical Models for Binder Burnout," *J. Am. Ceram. Soc.*, **73** 575 (1990)

7. J. A. Lewis, "Binder Removal From Ceramics," *Annual Rev. Mater. Sci.*, **27** 147-173 (1997).

8. R. V. Shende and S. J. Lombardo, "Determination of Binder Decomposition Kinetics for Specifying Heating Parameters in Binder Burnout Cycles," *J. Am. Ceram. Soc.*, **85** [4] 780-786 (2002).

9. S. J. Lombardo, J. W. Yun, and D. S. Krueger "The Influence of Binder Degradation Kinetics on Rapid Binder Removal Cycles"; pp. 191-204 in Ceramic Transactions Vol. 166, *Innovative Processing and Synthesis of Ceramics, Glasses, and Composites, VII.* Edited by N. P. Bansal. American Ceramic Society, Westerville, OH, 2004.

10. Z. C. Feng, B. He, and S. J. Lombardo, "Stress Distribution in Porous Ceramic Bodies During Binder Burnout," *J. of Appl. Mech.*, **69**, 497-501 (2002).

11. S. J. Lombardo and Z. C. Feng, "Pressure Distribution during Binder Burnout in Three-Dimensional Porous Ceramic Bodies with Anisotropic Permeability," *J. Mat. Res.,* **17**, 1434-1440 (2002).

12. K. Feng and S. J. Lombardo, "Modeling of the Pressure Distribution in Three-Dimensional Porous Green Bodies during Binder Removal," *J. Am. Ceram. Soc.,* **86** [2] 234-240 (2003).

13. S. J. Lombardo and Z. C. Feng, "Determination of the Minimum Time for Binder Removal and Optimum Geometry for Three-Dimensional Porous Green Bodies," *J. Am. Ceram. Soc.,* **6** [12] 2087-2092 (2003).

14. S. J. Lombardo and Z. C. Feng, "Analytic Method for the Minimum Time for Binder Removal from Three-Dimensional Porous Green Bodies," *J. of Mat. Res.,* **18,** 2717-2723 (2003).

15. S. J. Lombardo and R. V. Shende, "Determination of Polymer Decomposition Kinetics to Specify Ramps and Holds for Binder Burnout Cycles for Multilayer Ceramic Capacitors"; pp. 23-31 in Ceramic Transactions, Vol. 131, *Advances in Dielectric Materials and Multilayer Electronic Devices, American Ceramic Society.* Edited by K. M. Nair, A. S. Bhalla, and S.-I. Hirano. American Ceramic Society, Westerville, OH, (2002).

16. J. W. Yun and S. J. Lombardo, "Heat Transfer Effects in Porous Green Bodies During Binder Removal by Minimum Time Heating Cycles," *J. Am. Ceram. Soc.,* **89** [4] 1193-1199 (2006).

CHAPTER 2

FLUXES FROM SLIP, KNUDSEN, AND POISEUILLE FLOW IN

NARROW CAPILLARIES

2.1 INTRODUCTION

The flow of gases in narrow capillaries and porous media [1-6] can be analyzed in terms of fluid transport models that describe Knudsen, slip, and Poiseuille flow. The particular type of flow behavior depends on whether the motion of a molecule consists primarily of either collisions with the walls (Knudsen flow) or collisions with other molecules (Poiseuille flow) or a combination thereof (slip flow). The contribution of each mechanism to the total flux depends on the ratio of the pore size to the mean free path of gas molecules, which in turn depends on the pressure. Earlier research has focused on quantifying the contributions of each of these individual flow types to the overall flow in a capillary [7-13].

For the specific case of binder removal from open pore compacts [14-21], the permeability is expected to change as binder is removed and the pore space becomes more open. Both the void fraction and the pore size are expected to increase as the products of binder degradation exit the porous green body. In order to be able to describe the evolution of permeability with binder volume loading, it is first necessary to understand how the three flow mechanisms contribute to the total flow in a porous medium. In this study, we obtain the exact analytical solution for flow in a narrow capillary and then compare it with an approximate analytical solution obtained by others [13].

2.2   RESULT AND DISCUSSION

For a single capillary of radius, r, the molar flux, N, in the x-direction at temperature, T, is given by [12]

$$N = -\frac{K_T}{RT}\frac{dP}{dx}$$

2-1

where R is the gas constant and P is the pressure.   The quantity K_T consists of contributions from Knudsen, slip, and Poiseuille flow as [12]

$$K_T = \phi\left[\frac{2}{3}r\bar{v}\right]_{Knudsen} + (1-\phi)\left[\left(\frac{\pi r\bar{v}}{6}\right)_{Slip} + \left(\frac{r^2P}{8\mu}\right)_{Poiseuille}\right]$$

2-2

where μ is the viscosity of the gas and the average velocity of the gas molecules is $\bar{v} = (8RT/\pi M)^{1/2}$ in terms of M, the molecular weight of the gas-phase species.   The contributions of the individual flow mechanisms to K_T are determined by the probability, $\phi = 1/(1+2r/\lambda)$, which is terms of the ratio of the pore size to the mean free path, $\lambda = RT/\sqrt{2}\,\pi d^2 N_A P$ of the gas phase species.   The molecule diameter of the gas molecule is d, and N_A is Avogadro's number.   In Fig. 2.1, the dependence of ϕ is shown on the ratio of the pore size to the mean free path.   When the ratio of $2r/\lambda$ is small, i.e., when the pore size is much smaller than the mean free path, then ϕ approaches unity and Knudsen flow dominates.   Conversely, when the ratio of $2r/\lambda$ is large, i.e., when the pore size is much larger than the mean free path, then ϕ approaches zero and Poiseuille flow dominates.

1.2

1.0

0.8

0.6

0.4

0.2

0.0

Probability (-)

0.01   0.1   1   10   100

2r/λ (−)
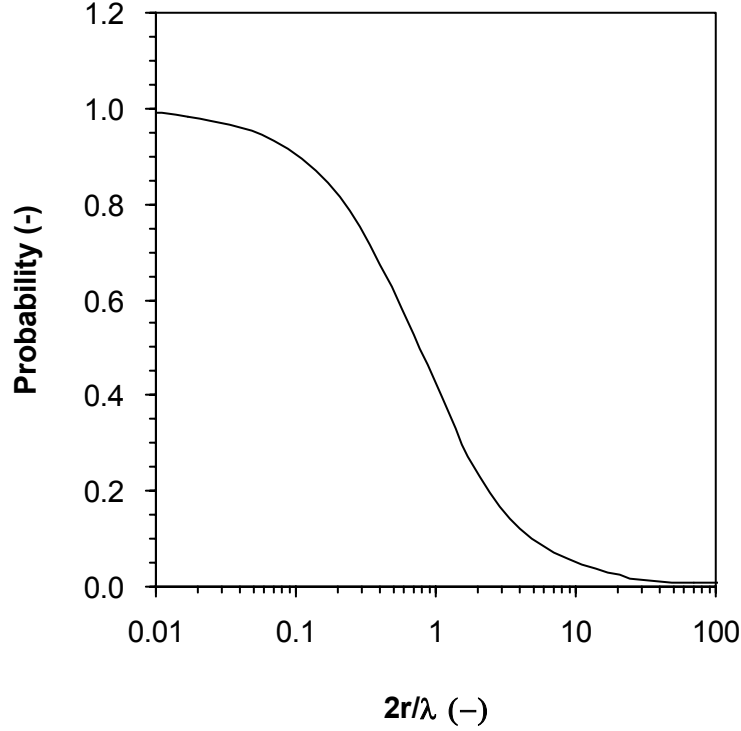
Figure 2. 1   Probability function, ϕ, for weighting Knudsen, slip, and Poiseuille flow mechanisms versus $2r/\lambda$.

In light of Eqs. 2-1 and 2-2, the total flux can be represented by three terms as

$$N = N_{Knudsen} + N_{Slip} + N_{Poiseuille} \qquad\qquad 2\text{-}3$$

corresponding to the three flow mechanisms.   When obtaining the solution to Eqs. 2-1 and 2-2 by integrating from P_1 to P_2 over the length, L, terms arise in the solution because of the explicit dependence on the pressure driving force and also because of the dependence of the probability terms on pressure via the mean free path.   To obtain the exact analytical solution, we introduce the constants $C_1 = r\bar{v}/RT$, $C_2 = 2\sqrt{2}r\pi d^2 N_A/RT$, and $C_3 = r^2/8\mu RT$. The total flux can then be rewritten as

$$N = -\left[\frac{2}{3}C_1\left(\frac{1}{1+C_2P}\right)_{Knudsen} + \frac{\pi}{6}C_1\left(\frac{1}{1+1/(C_2P)}\right)_{Slip} + C_3\left(\frac{P}{1+1/(C_2P)}\right)_{Poiseuille}\right]\frac{dP}{dx} \quad \text{2-4}$$

The exact analytical solution to Eq. 2-4, in terms of each flow mechanism, is thus

$$N_{Knudsen} = \frac{2}{3}\frac{C_1}{C_2L}\left[\ln\left(\frac{1+C_2P_1}{1+C_2P_2}\right)\right] \quad \text{2-5}$$

$$N_{Slip} = \frac{\pi}{6}\frac{C_1}{L}\left[(P_1-P_2)-\frac{1}{C_2}\ln\left(\frac{1+C_2P_1}{1+C_2P_2}\right)\right] \quad \text{2-6}$$

$$N_{Poiseuille} = \frac{C_3}{2L}\left[(P_1^2-P_2^2)-\frac{2}{C_2}(P_1-P_2)+\frac{2}{C_2^2}\ln\left(\frac{1+C_2P_1}{1+C_2P_2}\right)\right] \quad \text{2-7}$$

To obtain an approximate analytical solution to Eq. 2-4 [13], Eq. 2-1 can be rewritten in terms of a linear pressure drop $\Delta P = P_1 - P_2$ as

$$N_{Approx.} = \frac{\overline{K_T}}{RT}\frac{\Delta P}{L} \quad \text{2-8}$$

where $\overline{K_T}$ is given in terms of an average mean free path, $\overline{\lambda} = RT/\sqrt{2}\pi d^2 N_A \overline{P}$, where $\overline{P} = (P_1+P_2)/2$ is the arithmetic average pressure. The expression for $\overline{K_T}$ is

$$\overline{K_T} = \frac{1}{1+2r/\overline{\lambda}}\left[\frac{2}{3}r\overline{v}\right]_{Knudsen} + \frac{1}{1+\overline{\lambda}/2r}\left[\left(\frac{\pi r \overline{v}}{6}\right)_{Slip} + \left(\frac{r^2\overline{P}}{8\mu}\right)_{Poiseuille}\right] \quad \text{2-9}$$

With these substitutions into Eq. 2-8, the approximate flux from each mechanism is then given by [13]

$$\tilde{N}_{Knudsen} = \frac{2C_1}{3}\left(\frac{1}{1+C_2\overline{P}}\right)\frac{\Delta P}{L} \quad \text{2-10}$$

$$\tilde{N}_{Slip} = \frac{\pi C_1}{6}\left(\frac{1}{1+1/C_2\overline{P}}\right)\frac{\Delta P}{L} \quad \text{2-11}$$

$$\widetilde{N}_{Poiseuille} = C_3 \left(\frac{1}{1+1/C_2 \overline{\overline{P}}} \right) \frac{\overline{P} \Delta P}{L} = \frac{C_3}{2} \left(\frac{1}{1+1/C_2 \overline{\overline{P}}} \right) \frac{\left(P_1^2 - P_2^2 \right)}{L}$$ 2-12

The flux from each of the mechanisms thus depends via the constants C_1, C_2, C_3, and $\overline{P}$ on $2r/\overline{\lambda}$, the ratio of the pore size to the average mean free path, which in turn depends on the average pressure.

We next compare the approximate and analytical solutions for high and low pressure for $\mu=1.76\times10^4$ g/cm-s and $d=0.4$ nm, e.g., values appropriate for nitrogen gas. Figure 2.2 shows how the approximate analytical solution for the flux as a function of the pore size differs from the exact solution for each of the three flow mechanisms and for the total flux. For these simulations at high pressure with $P_1=0.79$ MPa and $\Delta P=0.69$ MPa, when the pore size is much smaller than mean free path, e.g., *2r/λ* is much less than 1, the dominant transport mechanism is Knudsen flow. For *2r/λ* much larger than 10, Poiseuille (laminar) flow is the dominant transport mechanism. In between the two regions of Knudsen and Poiseuille dominated flow, slip flow prevails. In general, at these high pressures, the approximate solutions for slip and Poiseuille flow agree well with their exact solutions, whereas the approximate solution for Knudsen flow diverges from the exact solution at larger pore diameters. This difference is small, however, and in addition does not influence the total flux by much because Knudsen flow is such a small portion of the overall flux at high pressures and for large pore sizes.

Figure 2.3 treats the same case as in Fig. 2.2 but now for lower pressures where $P_1=0.14$ MPa and $\Delta P=0.04$ MPa. The approximate solutions for all three flow mechanisms agree well with the exact solution for all pore sizes, and thus the total flux is well represented for all pore sizes.
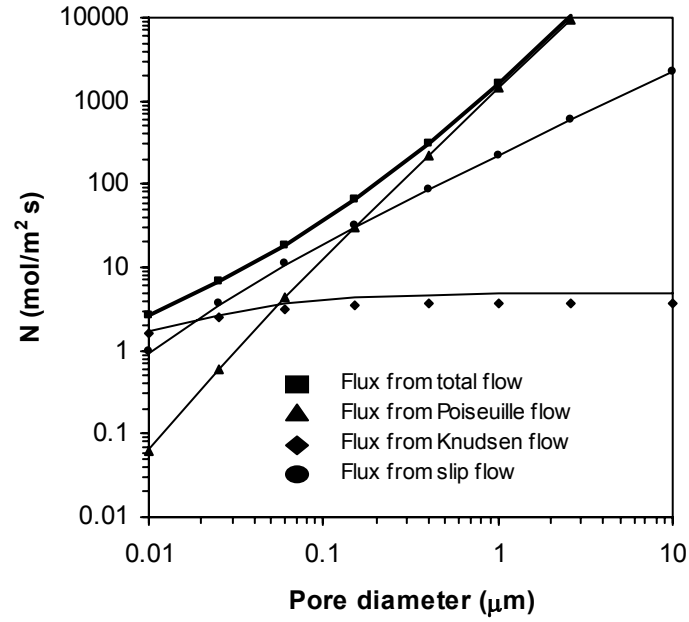
Figure 2. 2 **Contributions of Knudsen, slip, and Poiseuille flow to the total flux versus pore diameter for P_1=0.79 MPa and ΔP=0.69 MPa. The exact solutions are given by the lines and the approximate solutions are given by the symbols**
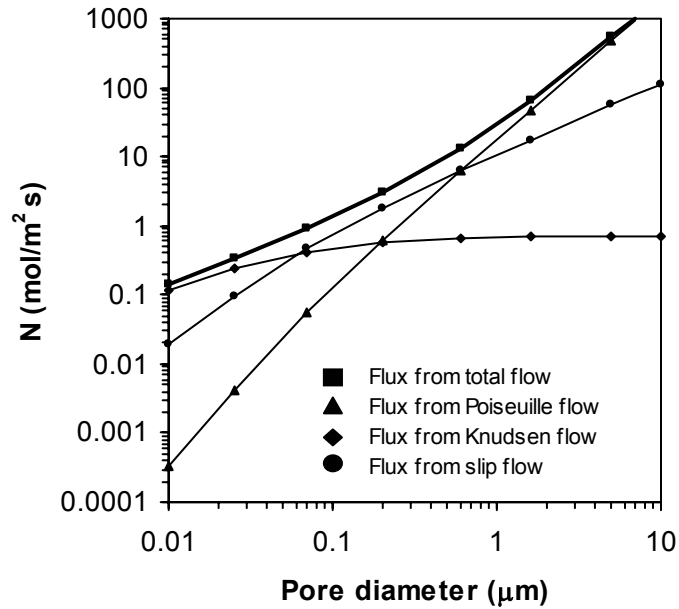
Figure 2. 3 **Contributions of Knudsen, slip, and Poiseuille flow to the total flux versus pore diameter for P_1=0.14 MPa and ΔP=0.04 MPa. The exact solutions are given by the lines and the approximate solutions are given by the symbols.**

As a final comparison of the two solutions, Figure 2.4 shows a comparison of the approximate and exact solutions for a pore size of 1 μm as a function of P_1 at fixed P_2=0.1 MPa. The total flux from the approximate solution agrees well with the exact solution as P_1, and thus ΔP, increases, because for Poiseuille flow, the approximate solution is always close to the exact solution, and Poiseuille flow is the dominant transport mechanism in pores of 1 μm size. In contrast, Knudsen flow from the approximate solution is slightly less than the exact solution as P_1 increases.
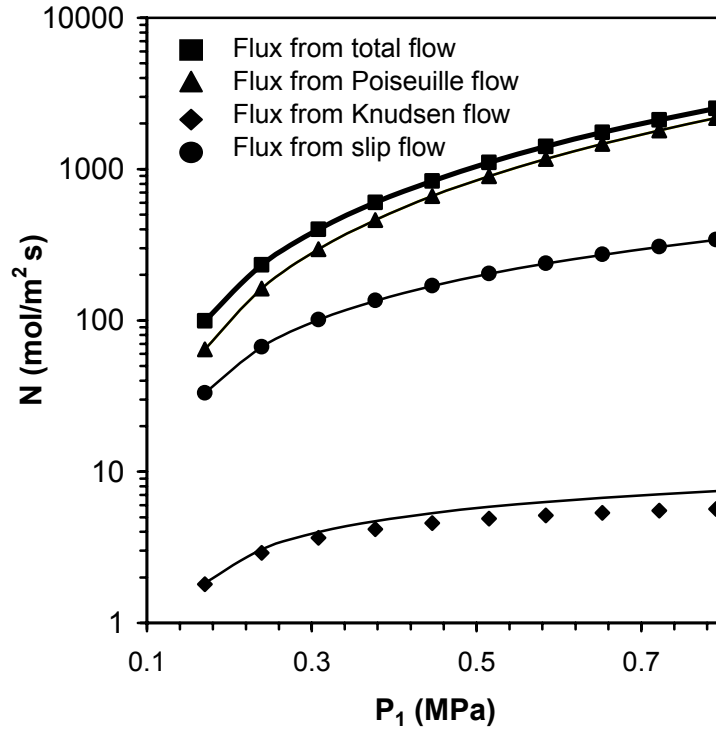
Figure 2. 4   Contributions of Knudsen, slip, and Poiseuille flow to the total flux versus upstream pressure for a pore diameter of 1 μm and P_2=0.1 MPa.   The exact solutions are given by the lines and the approximate solutions are given by the symbols.

The differences between the approximate and exact solution arise because of the use of an average pressure in the approximate solution for the probability term. For a

compressible fluid, the pressure profile as a function of position is given by [1],

$$P = \left[\left(\frac{P_2^2 - P_1^2}{L} \right) x + P_1^2 \right]^{1/2} \qquad\qquad 2\text{-}13$$

This contrasts to the linear relation which arises for an incompressible fluid, where the pressure varies as

$$P = \left(\frac{P_2 - P_1}{L} \right) x + P_1 \qquad\qquad 2\text{-}14$$

Figure 2.5 shows the difference between these two pressure distributions as a function of distance in the sample. At higher pressure differences, the difference between the two pressure profiles becomes larger, and thus the linear representation of the pressure profile becomes a worse approximation. When ΔP is thus large, the difference between the approximate and exact solutions for Knudsen flows is larger than for smaller ΔP. This difference appears mathematically in terms of a ΔP driving force for the approximate solution compared to the natural logarithm pressure driving force in the exact solution; the difference between the two, however, becomes smaller as ΔP decreases.

The above analysis illustrates how Knudsen, slip, and Poiseuille flow contribute to the total flux in narrow capillaries of different sizes. In general, the approximate solution is quite accurate and thus can be used for describing flow in narrow capillaries.
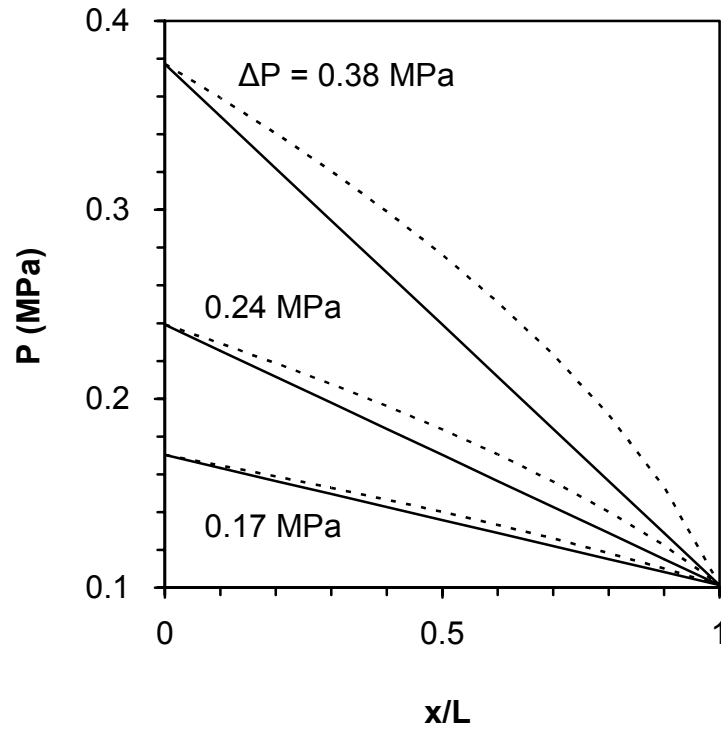
Figure 2. 5   Comparison of the pressure profiles with normalized position, *x/L*, for a compressible fluid (dashed lines) and for a linear pressure drop (solid lines) for three values of the total pressure difference.

2.3   CONCLUSIONS

Flow in narrow capillaries is analyzed in terms of mechanisms for describing Knudsen, slip, and Poiseuille flow. An approximate solution proposed earlier is compared to the exact solution and found to be very accurate, especially at low pressure over a range of pore sizes.

2.4   REFERENCES

1.   A.E. Scheidegger, *The Physics of Flow Through Porous Media* (University of Toronto Press, Toronto, 1974).

2.   F. A. L. Dullien, *Porous Media: Fluid Transport and Pore Structure* (Academic Press, New York, 1979).

3.   J. Bear, and J.-M. Buchlin, *Modelling and Applications of Transport Phenomena in Porous Media* (Kluwer Academic Publishers, Dordrecht, 1991).

4.   M. Sahimi, *Flow and Transport in Porous Media and Fractured Rock* (VCH, Weinheim, 1995).

5.   R. D. Boer, "Development of Porous Media Theories - a Brief Historical Review," *Transp. Porous Media,* **9** 155-64 (1992).

6.   H. David, "A Review of Terminology Pertaining to Darcy's Law and Flow through Porous Media," *Journal of Porous Media*, **6** 87-97 (2003).

7.   L. J. Klinkenberg, "The Permeability of Porous Media to Liquids and Gases*," Drill. Prod. Prac. API*, 200-13 (1941).

8.   G. P. Brown, A. DiNardo, G. K. Cheng, and T. K. Sherwood, "The Flow of Gases in Pipes at Low Pressures," *J. Appl. Phys.,* **17** 802-13 (1946).

9.   D. S. Scott and F. A. L. Dullien, "Diffusion of Ideal Gases in Capillaries and Porous Solids," *AIChE J.*, **8** 113-17 (1962).

10.   D. S. Scott and F. A. L. Dullien, "The Flow of Rarefied Gases," *AIChE J.*, **8** 293-97 (1962).

11.   N. Wakao and J. M. Smith, "Diffusion in Catalyst Pellets," *Chem. Eng. Sci.*, **17** 825-34 (1962).

12.   N. Wakao, S. Ontani, and J. M. Smith, "Significance of Pressure Gradients in Porous Materials: Part 1. Diffusion and Flow in Fine Capillaries," *AIChE J.*, **11** 435-39 (1965).

13.   S. Ontani, N. Wakao, and J. M. Smith, "Significance of Pressure Gradients in Porous Materials: Part 2. Diffusion and Flow in Porous Catalysts," *AIChE J.*, **11** 439-45 (1965).

14.   R. M. German, "Theory of Thermal Debinding," *Int. J. Powder Metall.*, **23** 237-45 (1987).

15. J. A. Lewis, "Binder Removal From Ceramics," *Annual Rev. Mater. Sci.*, **27** 147-173 (1997).

16. G. Y. Stangle, and I. A. Aksay, "Simultaneous Momentum, Heat and Mass Transfer With Chemical Reaction in a Disordered Porous Medium: Application to Binder Removal From a Ceramic Green Body," *Chem. Eng. Sci.,* **45** 1719-1731 (1990).

17. D-S. Tsai, "Pressure Buildup and Internal Stresses During Binder Burnout: Numerical Analysis ," *AIChE J.*, **37** 547-54 (1991).

18. S. A. Matar, M. J. Edirisinghe, J. R. G. Evans, and E. H. Twizell, "Effect of Porosity Development on the Removal of Organic Vehicle from Ceramic or Metal Moldings," *J. Mater. Res.,* **8** 617-625 (1993).

19. J. H. Song, M. J. Edirisinghe, J. R. G. Evans, and E. H. Twizell, "Modeling the Effect of Gas Transport on the Formation of Defects during Thermolysis of Powder Moldings," *J. Mater. Res.,* **11** 830-840 (1996).

20. S. J. Lombardo and Z. C. Feng, "Determination of the Minimum Time for Binder Removal and Optimum Geometry for Three-Dimensional Porous Green Bodies," *J. Am. Ceram. Soc.,* **6** 2087-2092 (2003).

21. S. J. Lombardo and Z. C. Feng, "Analytic Method for the Minimum Time for Binder Removal from Three-Dimensional Porous Green Bodies," *J. of Mat. Res.,* **18** 2717-2723 (2003).

CHAPTER 3

PERMEABILITY OF GREEN CERAMIC TAPES AS A FUNCTION

OF BINDER LOADING

3.1 INTRODUCTION

In the fabrication of ceramic components, the permeability [1-6] of the green body influences or governs a number of processing steps such as slip casting, drying, and binder removal. For the specific case of binder removal from open pore compacts, the permeability may strongly control the rate at which the sample can be heated in order to avoid failure of the body [7-15].   The permeability is also not a constant characteristic of the green body, but evolves in time as solid binder is removed.   The loss of binder is expected to both increase the porosity and to change the surface area to volume ratio within the porous medium; both effects will lead to changes in the permeability.

For porous bodies in which large pores are present, *e.g.*, the mean free path is much smaller than the pore size, such that pressure-driven convective flow dominates, a large number of models have appeared for describing the permeability [1-6,16-22]. Complications that may arise include whether or not viscous or inertial effects are controlling the flow behavior.   In addition, no commonly accepted model has appeared that describes the permeability in terms of no adjustable parameters.   In many treatments, however, a common feature is that both the porosity (or void fraction) within the green body and some characteristic dimension or distribution of dimensions appears as model parameters.   This length aspect of the permeability is most often related to some controlling pore size or surface area per unit volume; these latter two quantities can be interpreted in terms of a hydraulic resistance which governs the pressure drop, and hence flow rate, within the pores in the green body.   In addition, a term is often included to account for tortuosity and constriction in the pore space.

For small pore sizes where the mean free path is comparable or larger than the pore size, both Knudsen and slip flow contribute to the total observed flux [23-29]. This aspect of the problem for flow in narrow capillaries was treated successfully a number of years ago [28,29], but the extension of these results to porous media is again difficult, and several models have appeared which relate flow in narrow capillaries to flow in porous bodies [10,27,29]. These models either were strictly theoretical and not compared to experiment, or when compared to experiment, required the inclusion of adjustable parameters in order to obtain good agreement.

Recently, we have developed a method for determining the minimum time for binder removal from porous green bodies where convective flow is the dominant transport mechanism by which the degradation products exit the pore space of the green component [13-15]. The model thus requires values for the permeability as a function of binder content. Thus, the difficulty in describing the permeability is now compounded in that we are seeking a unique function for the permeability, preferably with no or at most one adjustable parameter.

In this work, the measurement of the flux through green bodies as a function of binder content is reported. We then describe an approach for obtaining from such flux data the pore diameter and the permeability as a function of binder content. The permeability is then related to other microstructural characteristics of the green body.

3.2 EXPERIMENTAL

The tape samples used in this study were prepared from barium titanate powder (Tamtron X7R 412H, Ferro Electronic Materials, Niagara Falls, NY), which has a mean particle diameter of 1.2 μm and specific surface area of 3.3 m^2/g.   The powder at 55.6 wt% was ball milled with 44.6 wt% binder solution (B73305 Ferro Corp., San Marcos, CA), which contains approximately 14 wt% poly(vinyl butyral), 8 wt% dioctyl phthalate, 60 wt% toluene, and 18 wt% ethanol.   After milling, the slurry was de-aired and then filtered through a 53 μm nylon mesh.   The slurry was then tape cast, dried, and cut to obtain samples.   The thickness of the dried tapes was approximately 125 μm.   The total organic content of the substrates was 10.9% by weight, as determined by weight loss based on the total sample weight.   To prepare samples with up to two-thirds lower binder content, oxidation in air was used at temperatures between 150-200°C for times of 0.5-24 h.   Below approximately 4 wt% binder, the samples were brittle and fractured during testing.

To perform the permeability measurements, green tapes of disk geometry were inserted into a sample holder (see Fig. 3.1, Millipore, MA) with an open area of 1.56 cm in diameter and sealed with a flexible o-ring.   An upstream pressure of nitrogen was set by a pressure regulator, and the downstream pressure could be adjusted by the valve before the flow meter.   The volumetric flow rate, V_f, in the flow meter was monitored and then converted to a molar flow rate, n, via

$$n = \frac{P_f V_f}{RT_f}$$

3-1

where P is the pressure, R is the gas constant, T is the temperature, and the subscript f

denotes the conditions at the flow meter.   The measured molar flux, N_m, through the

area, A, of the substrate is then given by

$$N_m = n/A = u_o \rho \hspace{5cm} \text{3-2}$$

where u_o is the superficial velocity and $\rho = P/RT$ is the molar density.   The flux

given by Eq. 3-2 is a quantity determined solely by experiment and contains no

microstructural features of the porous green body.
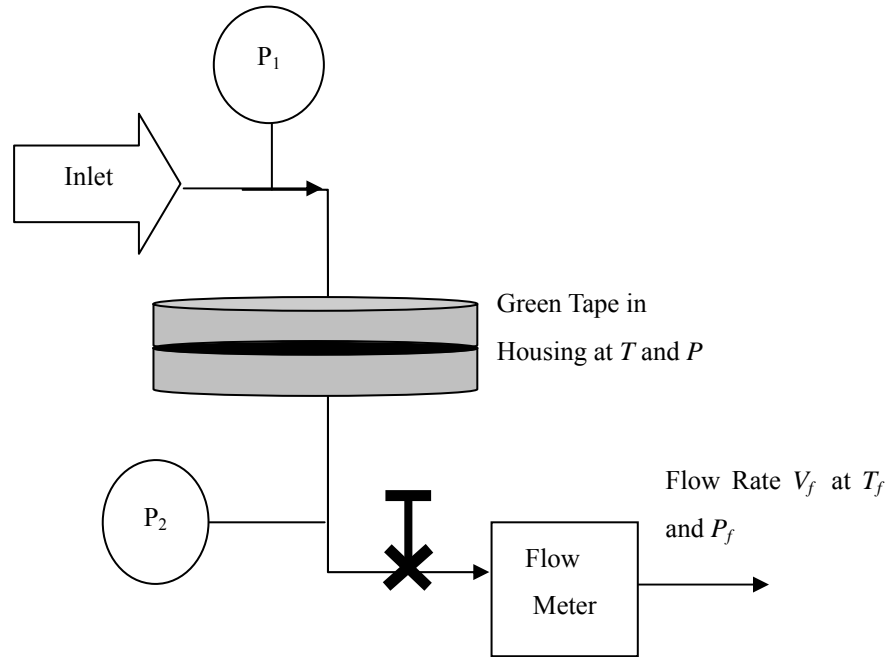
Figure 3. 1   Schematic of the flow cell used to measure the permeability of green ceramic tapes.

3.3 RESULTS AND DISCUSSION

The microstructures of green tape samples at high (10.9 wt%), medium (6.2 wt%), and low (0 wt%) binder contents are shown in Fig. 3.2.   These samples were prepared by freezing substrates in liquid nitrogen and then fracturing them.   For the tape with 10.9 wt% binder, regions of sample rich and poor in binder content are observed.   Large pores or channels of micron size and irregular shape appear throughout the sample, and many of these pores are separated by distances of many multiples of the ceramic particle diameter.   No clear characteristic single pore dimension is evident, but rather a distribution of pore dimensions is seen.   For the sample of intermediate binder loading, more pores of smaller size are evident with smaller separation distances between them. For the sample with no binder, pores appear to be located between almost every individual ceramic particle.   Large sized channels, however, are still evident.
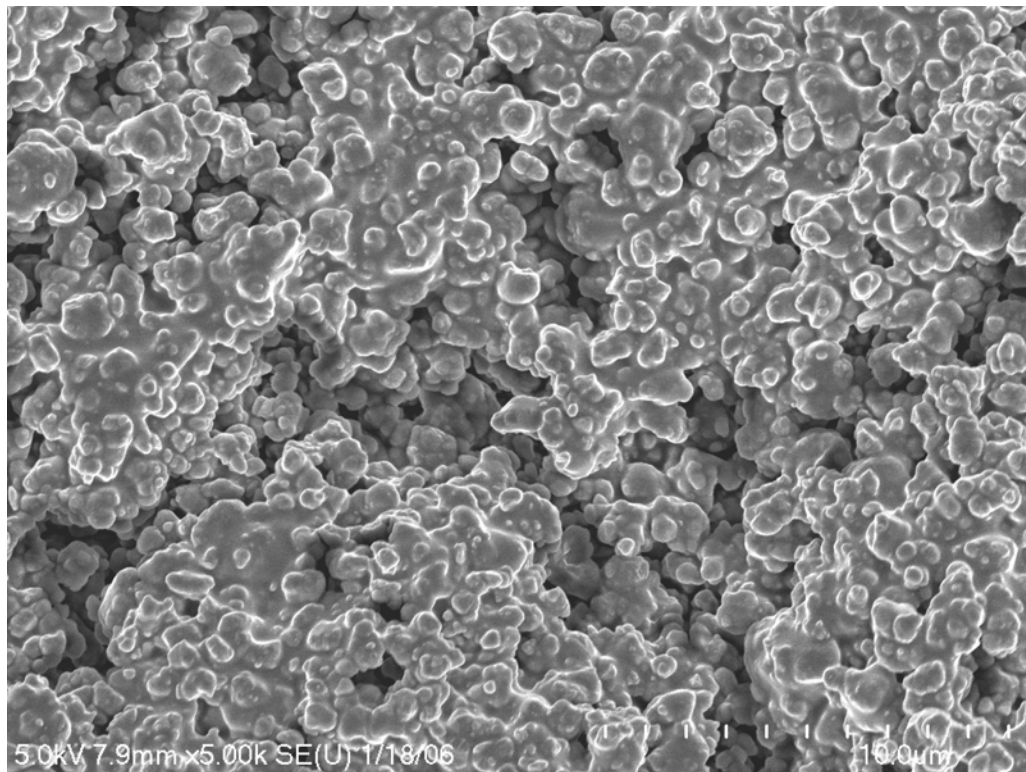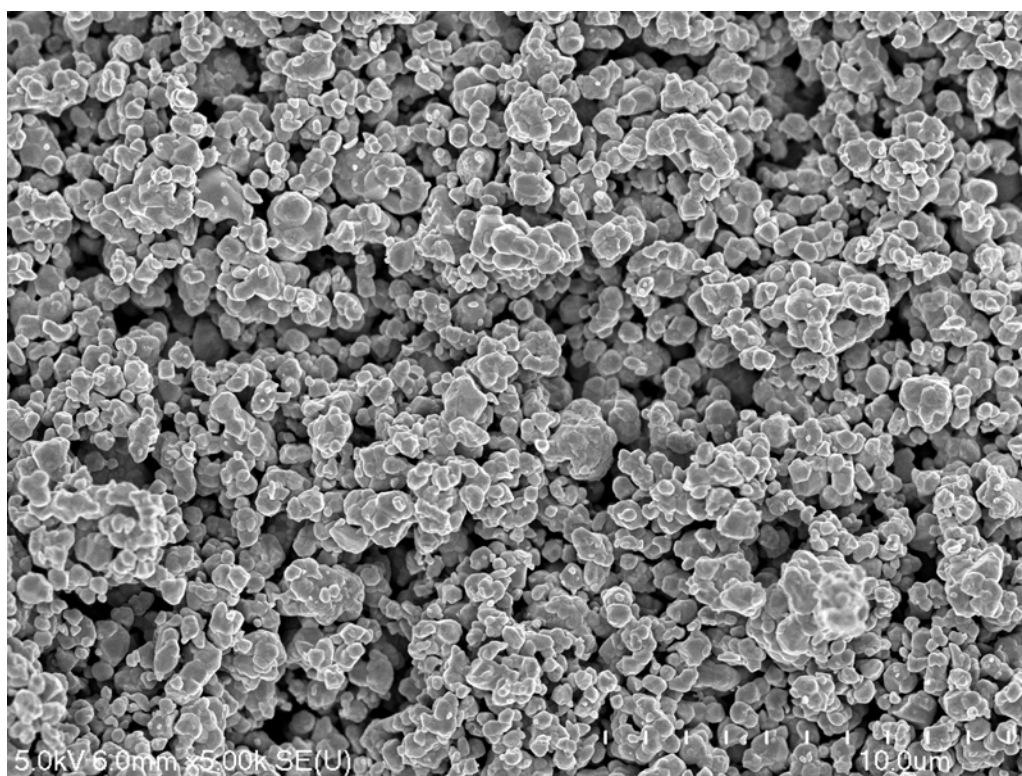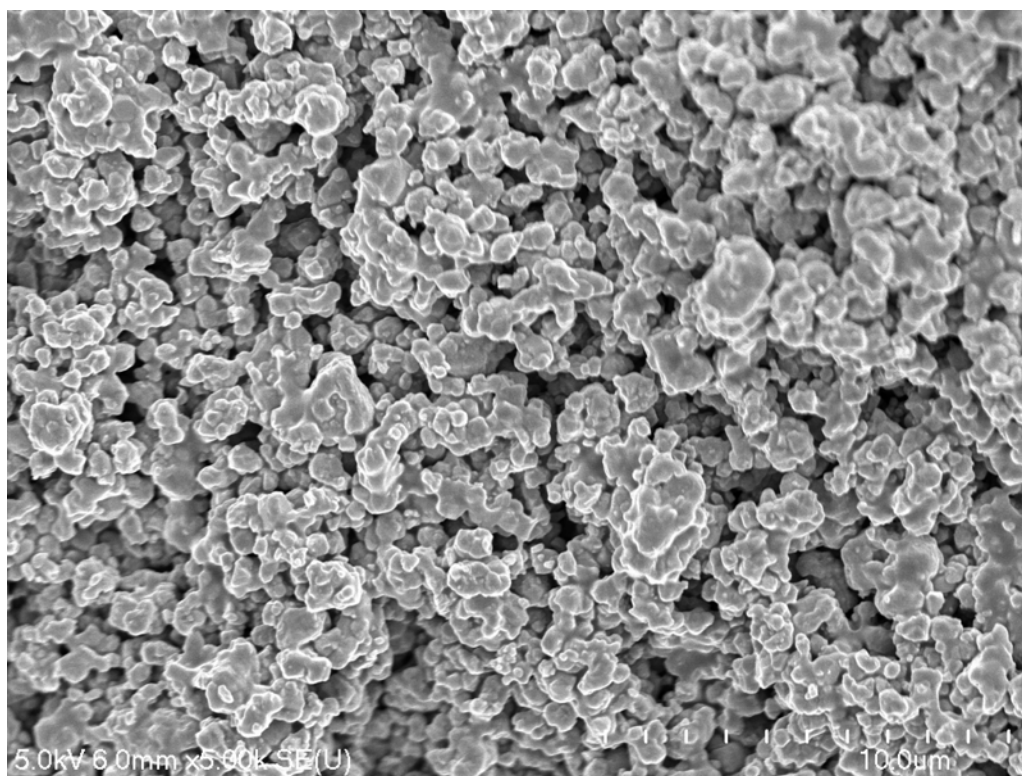
Figure 3. 2 Scanning electron micrographs of green tape samples at high (10.9 wt%, the first panel, P.28), medium (6.2 wt%, the second panel, P.29), and low (0 wt%, the third panel, P.29) binder contents.

For a single capillary of radius, r, the molar flux, N, in the x-direction can be represented by [10,28]

$$N = -\frac{\kappa_T}{RT}\frac{dP}{dx}$$ 3-3

The quantity κ_T depends on the flow regime, which is determined by the ratio of the pore diameter, $D=2r$, to the mean free path, $\lambda = RT/2^{1/2}\pi d^2 PN_A$, of the gas-phase species, where d is the molecular diameter and N_A is Avogadro's number. The term κ_T can be expressed as the weighted summative contributions from Knudsen, C, slip, B, and Poiseuille, A, flow mechanisms as

$$\kappa_T = \frac{2r\bar{v}/3}{1+2r/\lambda} + \frac{1}{1+\lambda/2r}\left[\frac{\pi r\bar{v}}{6} + \frac{r^2 P}{8\mu}\right] = \frac{C}{1+2r/\lambda} + \frac{1}{1+\lambda/2r}[B+A]$$ 3-4

with $C = 2/3r\bar{v}$, $B = \pi r\bar{v}/6$, $A = r^2 P/8\mu$, where μ is the viscosity of the gas. The quantity $\bar{v} = (8RT/\pi M)^{1/2}$ is the average velocity in terms of the molecular weight, M, of the gas-phase species. Equations 3 and 4 can be integrated from P_1 to P_2 over the sample thickness, L, to yield the total flux for a compressible fluid as

$$N = N_{Knudsen} + N_{Slip} + N_{Poiseuille}$$ 3-5

where

$$N_{Knudsen} = -\frac{2}{3}\frac{C_1}{C_2 L}\left[\ln(1+C_2 P_2) - \ln(1+C_2 P_1)\right]$$ 3-6

$$N_{Slip} = \frac{\pi}{6}\frac{C_1}{C_2 L}\left[-C_2 P_2 + \ln(1+C_2 P_2) + C_2 P_1 - \ln(1+C_2 P_1)\right]$$ 3-7

$$N_{Poiseuille} = \frac{C_3}{2C_2^2 L}\left[-C_2^2 P_2^2 + 2C_2 P_2 - 2\ln(1+C_2 P_2) + C_2^2 P_1^2 - 2C_2 P_1 + 2\ln(1+C_2 P_1)\right]$$

3-8

with $C_1 = r\bar{v}/RT$, $C_2 = 2r\sqrt{2}\pi d^2 N_A /RT$, and $C_3 = r^2/8\mu RT$.

The relative fluxes from each of the three mechanisms thus depend on the ratio of the pore diameter to the mean free path, which in turn depends on the pressure. Figure 3.3 shows how the three mechanisms contribute to the total flux as a function of the pore size for $P_1 = 0.38$ MPa and $\Delta P = 0.28$ MPa. For small pores, where the ratio $2r/\lambda$ is much less than unity, Knudsen flow is the dominant transport mechanism. For intermediate pore sizes, where $2r/\lambda \approx 1\text{-}10$, slip flow is the largest contributor to the observed flux although both Knudsen and Poiseuille flow also make significant contributions. For larger pore sizes, where $2r/\lambda$ is much greater than unity, Poiseuille flow dominates.
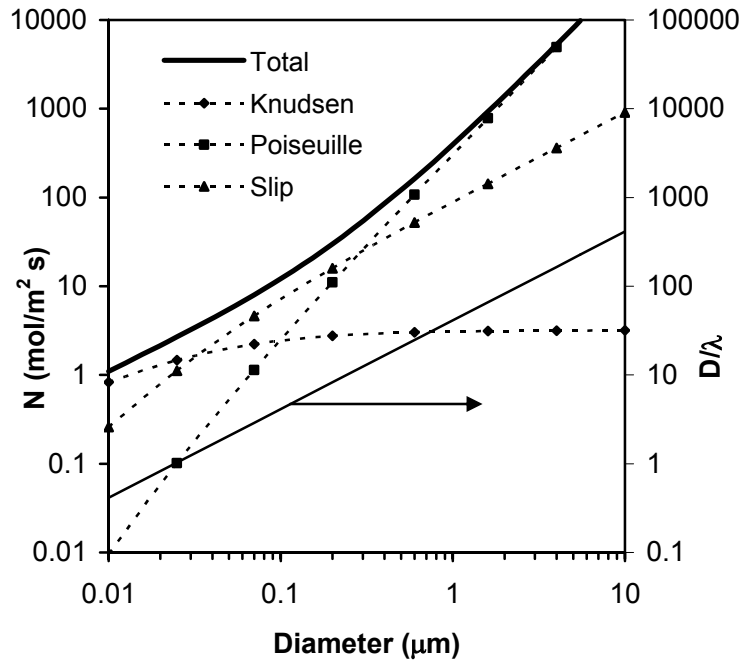
Figure 3. 3   Left-hand axis) Contributions of Knudsen, slip, and Poiseuille flow to the total flux versus pore size. Right-hand axis) Ratio of pore diameter to the mean free path of the gas molecule versus pore diameter.

To determine the characteristic pore size which governs the observed flow behavior, we adopt the procedure proposed in Ref. [26], whereby we obtain the flux as a function of the arithmetic mean pressure, P_{ave}. At higher pressures, where Knudsen flow can be neglected, a plot of the normalized flux, $N / \Delta P$ versus P_{ave} yields a linear relation

$$\frac{N}{\Delta P} = A P_{ave} + B \qquad\qquad\qquad 3\text{-}9$$

where A is the slope and B is the intercept. The ratio of

$$\frac{A}{B} = \frac{3\bar{r}}{4\pi\mu\bar{v}} \qquad\qquad\qquad 3\text{-}10$$

can then be used to determine the characteristic pore diameter, $D = 2\bar{r}$.

Figure 3.4 shows the linear relationships obtained as a function of binder loadings between 10.9-6.9 wt%. Below 6.9 wt% binder, the normalized flux did not vary linearly with the mean pressure, and the origin of this non-linearity is unclear. Equation 3-10 was then used to determine, as seen in Fig. 3.5, that the average characteristic pore size increases from approximately 1 to 2 μm as the fractional porosity, ε, in the sample increases from 0.2 to 0.3. Extrapolation of this curve to 0.4 fractional porosity, which corresponds to zero binder content, suggests a maximum characteristic pore size of ~2.3 μm. The variability in the pore size determined by this method is estimated as less than 15%.

For a pore size of 1 μm, which corresponds to the lowest level of porosity, Fig. 3.3 shows that Poiseuille flow contributes more than 95% of the total flux, and we can therefore neglect the Knudsen and slip flow terms. We note that the results shown in

Fig. 3.3 are based on equations derived for a single capillary. We use these results, however, to determine that the permeability in a porous body with a characteristic pore diameter of 1 μm arises mainly from Poiseuille flow. For the given range of pore sizes, the Reynolds number is less than 1×10^{-3}, and thus inertial effects are also not significant.
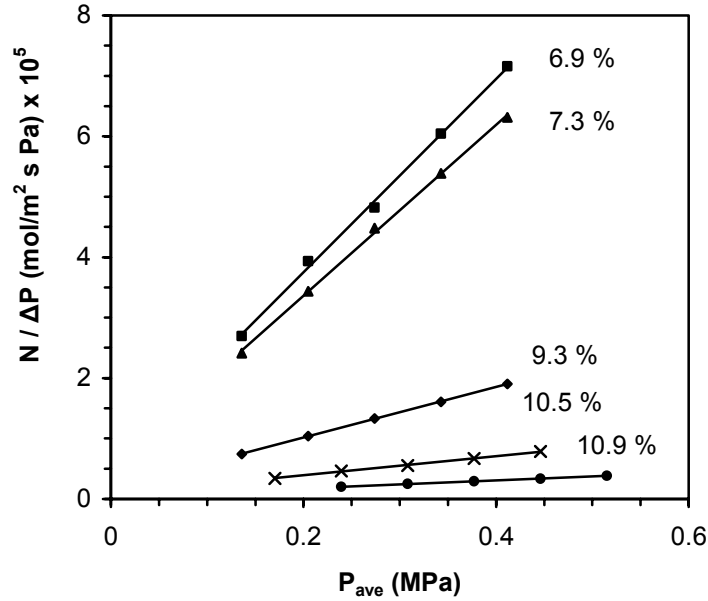
Figure 3. 4 Normalized flux versus average pressure for samples containing different binder loadings.
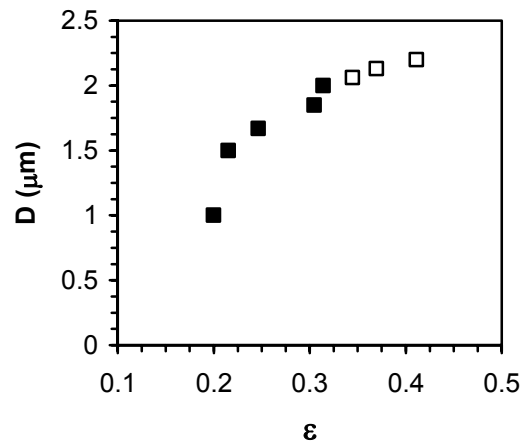
Figure 3. 5 Characteristic pore diameter versus porosity. The closed symbols were determined from experiment and the open symbols are extrapolated values.

Based on the above analysis, we are then left with the equivalent of Darcy's law for flow in porous media and can thus express the superficial velocity in Eq. 3-2 as

$$u_o = -\frac{\kappa}{\mu}\frac{dP}{dx} \qquad\qquad 3\text{-}11$$

where κ is the permeability arising from Poiseuille flow. Combining Eqs. 3-2 and 3-11 leads to the permeability as

$$\kappa = -\mu\frac{N_m}{\rho}\left(\frac{dP}{dx}\right)^{-1} \qquad\qquad 3\text{-}12$$

At steady state flow conditions, the pressure across the sample varies from P_1 to P_2 for a compressible fluid as [1]

$$P = \left[\frac{P_2^2 - P_1^2}{L}x + P_1^2\right]^{1/2} \qquad\qquad 3\text{-}13$$

When the ideal gas law is used to describe the molar density, Eq. 12 simplifies to

$$\kappa = -2RTN_m\mu\frac{L}{P_2^2 - P_1^2} \qquad\qquad 3\text{-}14$$

For κ to be a useful quantity, *e.g.*, an intrinsic material property, then it is desirable that changing the flow conditions or the sample thickness should not influence its value. To determine if these latter two conditions for the permeability, as given by Eq. 3-14, are satisfied, two types of experiments were conducted. In the first type, different upstream and downstream pressures of nitrogen were set to obtain a constant pressure drop of 0.28 MPa, and the flux and the permeability were then determined as described above.

Figure 3.6 shows that with increasing upstream pressure, the flux and gas density, determined at the center of the sample, both increase, whereas the superficial velocity is nearly constant. These three quantities vary in such a manner, however, that

the permeability is nearly constant.   For a given sample and set of flow conditions, the flux, and thus also the permeability, varied by less than 5%.   The variability between individual tape samples, however, was estimated at 15%.
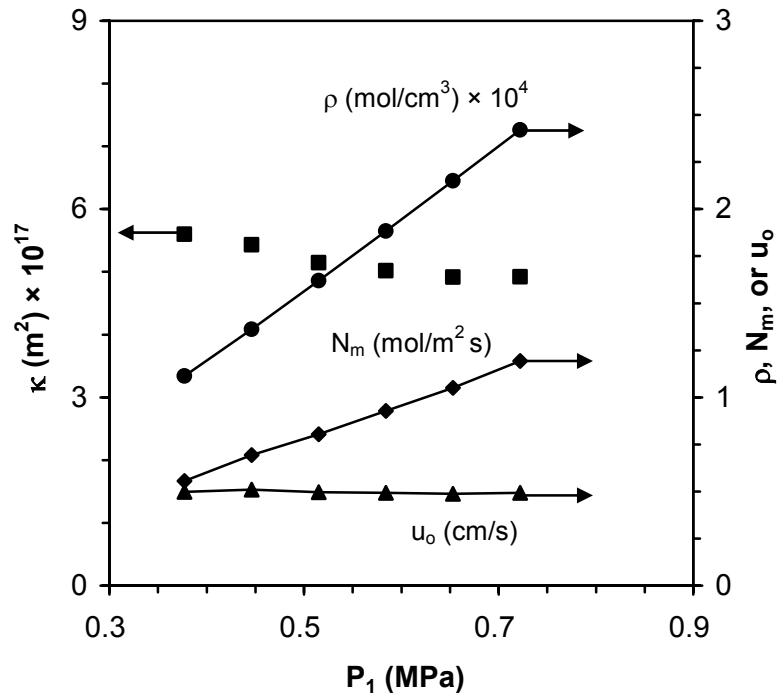
Figure 3. 6   Permeability, flux, gas density, and superficial velocity versus upstream pressure for a constant pressure drop of 0.28 MPa.

Figure 3.7 also illustrates the permeability as a function of upstream pressure, but now includes samples over a range of binder loadings.   The permeability of the tapes, which increases with decreasing binder loading as expected, is relatively constant versus the upstream pressure, and is thus independent of the specific values of the upstream and downstream pressures and gas density.
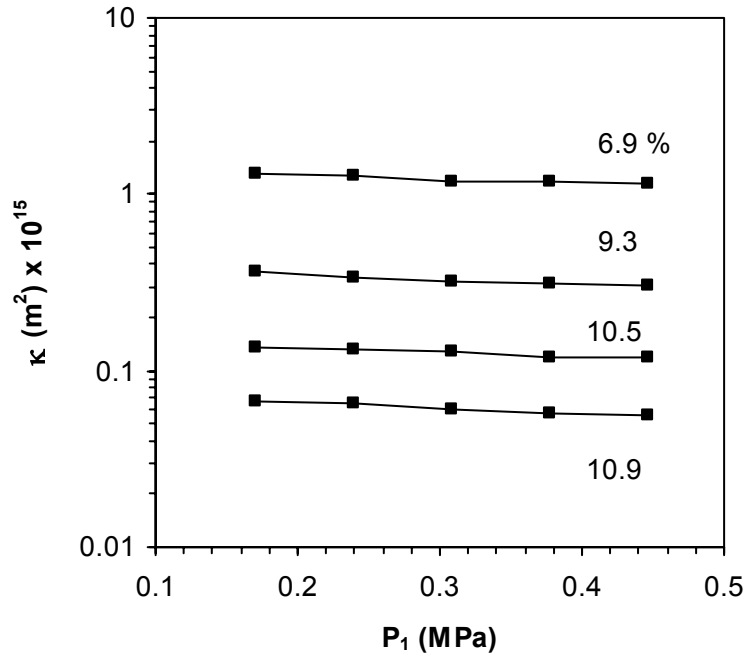
Figure 3. 7   Permeability versus upstream pressure for a constant pressure drop of 0.07 MPa as a function of binder loading.

In the second type of experiment, tapes were stacked to different total thicknesses in the sample holder, and then the permeability was determined for a fixed upstream pressure and different pressure drops.   As seen in Fig. 3.8, the permeability is again nearly constant and is thus independent of the total thickness and pressure drop. Taken together, the results in Figs. 3.7 and 3.8 indicate that analyzing the flux data obtained here in terms of Eq. 3-14 leads to permeabilities that are not strongly dependent on the flow conditions or sample thickness.

The permeability of individual tape substrates was then measured as a function of binder loading for binder removed by air oxidation.   Figure 3.9 shows that the permeability increases by a factor of 30 with decreasing binder content.   Below about one-third of the initial organic content, very few data points are evident because of the

brittle nature, and hence fracture during testing, of the samples low in binder. It appears, however, that the permeability is not varying as strongly over the last one-third of binder loading, as compared to the variation in the permeability for the initial amounts of binder removed.
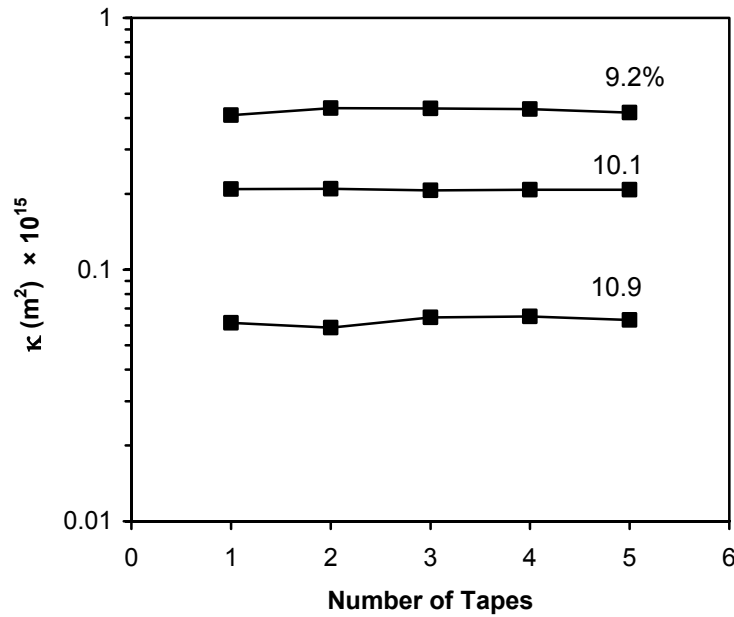
Figure 3. 8   Permeability versus number of stacked green ceramic tapes as a function of binder loading.

The permeabilities determined in the experiments in Figs. 3.6 through 3.9 are based only on Darcy's law for flow in porous media and make no mechanistic assumptions about what microstructural features of the porous medium are governing the flow behavior.   Many different approaches [1-6,10,16,27] have been proposed to account for the permeability in terms of such microstructural attributes as the porosity, characteristic pore size, and tortuosity and constrictions.   The large number of models, which were primarily developed for porous media consisting of one type of particle,

attests to the difficulty in accounting for the effects of different morphological features of the pore space on the permeability.   In this work, this difficulty is now compounded by having the need for a model that accounts for the permeability of a two-component porous medium as one phase is removed.
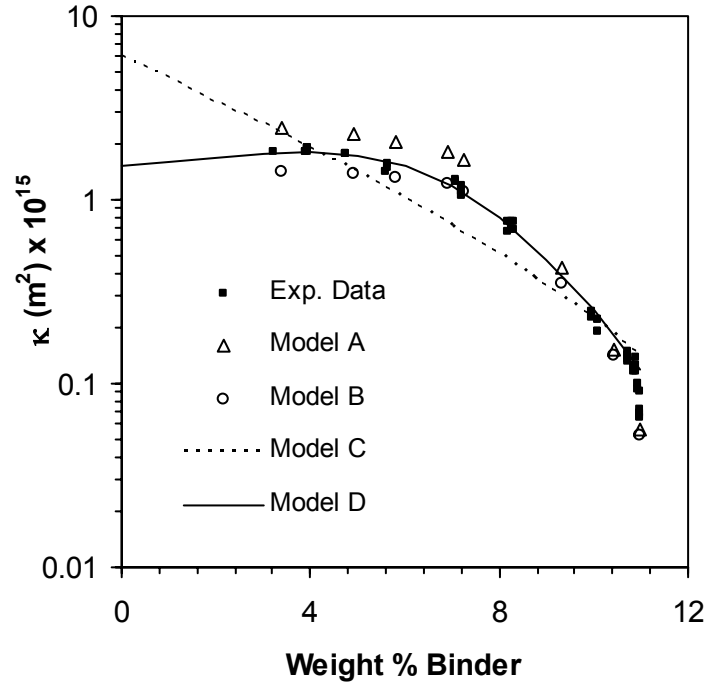
Figure 3. 9   Permeability of green ceramic tapes as a function of binder loading for binder removal by air oxidation.   The predictions of Models A-D are also shown.

In this work, we first relate the measured flux from an experiment to the flux from single capillary, modified by some function of the porosity as

$$N_m = u_o \rho = N \cdot f(\varepsilon) \qquad\qquad 3\text{-}15$$

The function $f(\varepsilon)$ is not generally known, but has alternatively been represented as proportional to the porosity, ε, in Ref. [10] and as ε^2 in Ref. [27].   We adopt, and

slightly modify, these approaches and let $f(\varepsilon) = 2\varepsilon^{\alpha+1}/k$, where k is a constant to account for tortuosity and constrictions. We further proceed to define an effective specific surface per unit solid volume, S, in terms of a hydraulic pore diameter, $D=4r$, as

$$S = \frac{4\varepsilon}{(1-\varepsilon)D} \qquad\qquad 3\text{-}16$$

With this definition for S combined with the term for Poiseuille flow from Eq. 3-4, we then obtain that the permeability is given by

$$\kappa = \frac{\varepsilon^{3+\alpha}}{k(1-\varepsilon)^2 S^2} \qquad\qquad 3\text{-}17$$

For $\alpha=0$, we obtain the Kozeny-Carman equation. Meyer and Smith [16] observed, however, that for bodies consisting of a single type of particle, the tortuosity increased with decreasing porosity as $k = 1.25\varepsilon^{-1.1}$. An expression of this type thus leads to $\alpha=1.1$, which leads to approximately the same dependence of ε^2 derived for a random pore model [27].

We can thus calculate the permeability in Eq. 3-17 in terms of four approaches related to how we determine the quantities S and k:

Model A: Obtain S from D (Eq. 16) and fit k from N_m versus P_{ave} data for $\alpha=0$;

Model B: Obtain S from D (Eq. 16) and fit k from N_m versus P_{ave} data for $\alpha=1$;

Model C: Obtain S fitted from permeability data with constant $k=5$ for $\alpha=0$;

Model D: Obtain S fitted from permeability data with a 2nd order polynomial with constant $k=5$ for $\alpha=0$.

Models A and B thus use the measured flux data to obtain both S and k, but do not directly use the permeability data in Fig. 3-9.   Models C and D, on the other hand, are

fitted directly to the permeability data in Fig. 3-9 with assumed conventional values of k.

Values of k for Model A were thus determined by fitting the measured fluxes versus average pressure for different binder loadings, as seen in Fig. 3.10.   In general, the level of agreement is quite good, and similarly good agreement was obtained with Model B.   Table 3.1 summarizes the values of k and S that arise by fitting the fluxes determined in the experiments for the first two models.   For Models A and B, k first decreases with increasing porosity and then increases slightly; S, however, varies only weakly in a nonmonotonic fashion with binder volume fraction.   For Model C, with constant $k=5$, the best fit for constant S is 4.18×10^{-6} m^{-1}.   For Model D, with constant $k=5$, the best fit variation in S in Table I spans 20%.   Figure 3.9 shows the level of agreement between the permeability and the predictions of the four models.   Both Models A and B describe the permeability reasonably well, in spite of not being fit directly to the permeability data.   Model C, which is the Kozeny-Carman equation with constant values of k and S, gives the poorest level of agreement.   Model D provides the best level of agreement, which is not surprising in that it is fitted to the permeability data by allowing S to be a function rather than a constant.

The values of k and S given in Table 3.1 deserve further comment.   As seen from the form of Eq. 3-17, the product kS^2 is the effective fitting parameter, and thus, depending on the model, changes in k are necessarily reflected in changes in S.   With Models A and B, S is determined directly from D, and then k is determined by fitting the flux data, as seen in Fig. 3.10.   For Model A, very large values of k are determined, which suggests a very tortuous path or small constrictions, or some combination thereof. The microstructures of Fig. 3.2 are consistent with this latter idea, in that the presence of

high binder loading appears to have occluded the pore space between clusters of individual ceramic particles. Use of Model B leads to values of k of the order of 20-50, which is a factor of ~2 larger than the largest values reported in Ref. [18] for systems containing particulates only. The nonmonotonic variation in k is less clear. This may arise as smaller pores begin to conduct more flow as binder is removed. Although in principle Eq. 3-3 can describe this effect, knowledge of the distribution of radii responsible for each flow regime are required. For Models C and D, in which k is fixed at a conventional value of 5, the values of S now obtained appear somewhat unrealistic in that if these are converted to an equivalent pore diameter via Eq. 3-16, pore diameters of $D \approx 0.2$-0.7 μm result. Under these circumstances, slip and Knudsen flow will contribute substantially more to the flux, and thus analyzing the flux data in terms of only Poiseuille flow is incorrect. The results in Figs. 3.7 and 3.8, however, indicate that Poiseuille flow, as represented by Darcy's Law, reasonably represents the permeability as an intrinsic material property.

In spite of the uncertainty in the actual values of the microstructural parameters governing the permeability, the method of analysis adopted here does lead to good representation of the permeability. Models A, B and D all describe reasonably well the permeability versus binder loading in terms of microstructural attributes of the porous medium. To do this, however, requires some experimental flux data and the inclusion of fitted or adjustable parameters, as is typically the case for describing the permeability of porous media.
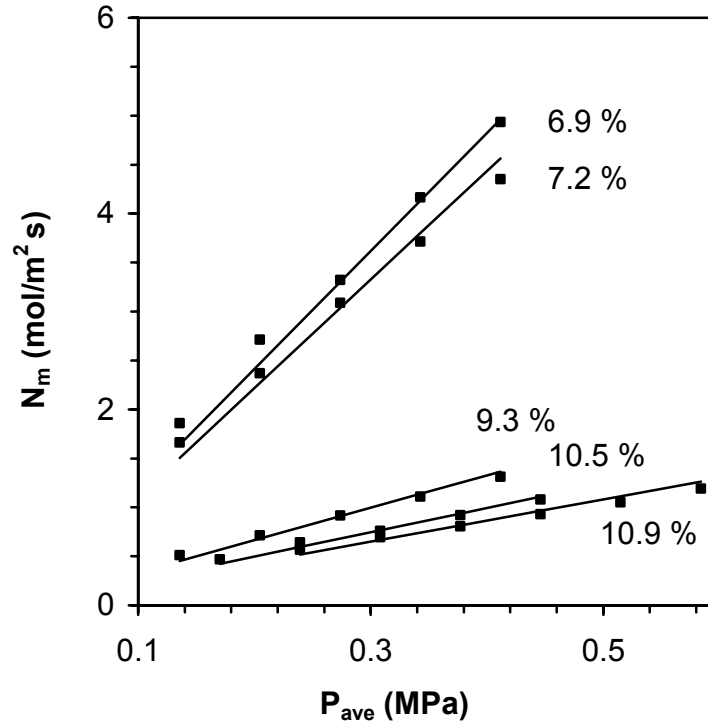
Figure 3. 10   Flux versus average pressure as a function of binder loadings.   The symbols are the values determined in the experiments and the lines are the best fits as a function of *k*.

Table 3. 1   Comparison of the values of the parameters comprising Models A-D for describing the permeability of green ceramic tapes

Binder Weight %	ε (-)	D (μm)	Model A		Model B		Model C		Model D	
			k (-)	$S\times10^{-6}$ (m^{-1})	k (-)	$S\times10^{-6}$ (m^{-1})	k (-)	$S\times10^{-6}$ (m^{-1})	k (-)	$S\times10^{-6}$ (m^{-1})
10.9	0.20	1.00	220	1.00	48	1.00	5	4.18	5	4.60
10.5	0.22	1.50	200	0.73	46	0.73	5	4.18	5	4.23
9.3	0.25	1.67	100	0.78	30	0.78	5	4.18	5	3.67
7.2	0.30	1.85	40	0.95	18	0.95	5	4.18	5	3.27
6.9	0.31	2.00	43	0.91	20	0.91	5	4.18	5	3.28
5.8	0.34	2.05	44	1.03	24	1.03	5	4.18	5	3.48
4.9	0.37	2.13	46	1.10	28	1.10	5	4.18	5	3.81
3.4	0.41	2.20	50	1.27	36	1.27	5	4.18	5	4.71

3.4 CONCLUSIONS

The permeability of green ceramic tapes as a function of binder loading has been determined. A method of analysis was used to determine the relative contributions from Knudsen, slip, and Poiseuille flow. Because the characteristic pore size was found to be of the order of 1-2 μm, the flux through the green tapes was attributed as arising mainly from Poiseuille flow. The permeability was related to a microstructural model in terms of a characteristic pore size or equivalently specific surface, the porosity, and a term to account for tortuosity and constrictions. For the different types of models evaluated, the specific surface was not strongly dependent on the binder loading, whereas the term accounting for tortuosity and constrictions depended more strongly on the binder loading.

3.5   REFERENCES

1. A.E. Scheidegger, *The Physics of Flow Through Porous Media,* University of Toronto Press, Toronto, 1974.

2. F. A. L. Dullien, *Porous Media: Fluid Transport and Pore Structure,* Academic Press, New York, 1979.

3. J. Bear, and J.-M. Buchlin, *Modelling and Applications of Transport Phenomena in Porous Media*, Kluwer Academic Publishers, Dordrecht, 1991.

4. M. Sahimi, *Flow and Transport in Porous Media and Fractured Rock*, VCH, Weinheim, 1995.

5. P.C. Carman, *Flow and Transport Through Porous Media*, Academic Press, New York, 1956.

6. H. David, "A Review of Terminology Pertaining to Darcy's Law and Flow through Porous Media," *Journal of Porous Media*, **6** [2] 87-97 (2003).

7. R. M. German, "Theory of Thermal Debinding," *Int. J. Powder Metall.*, **23** [4] 237-245 (1987).

8. J. A. Lewis, "Binder Removal From Ceramics," *Annual Rev. Mater. Sci.*, **27**, 147-173 (1997).

9. G. Y. Stangle, and I. A. Aksay, "Simultaneous Momentum, Heat and Mass Transfer With Chemical Reaction in a Disordered Porous Medium: Application to Binder Removal From a Ceramic Green Body," *Chem. Eng. Sci.,* **45**, 1719-1731 (1990).

10. D-S. Tsai, "Pressure Buildup and Internal Stresses During Binder Burnout: Numerical Analysis ," *AIChE J.*, **37** [4] 547-554 (1991).

11. S. A. Matar, M. J. Edirisinghe, J. R. G. Evans, and E. H. Twizell, "Effect of Porosity Development on the Removal of Organic Vehicle from Ceramic or Metal Moldings," *J. Mater. Res.,* **8**, 617-625 (1993).

12. J. H. Song, M. J. Edirisinghe, J. R. G. Evans, and E. H. Twizell, "Modeling the Effect of Gas Transport on the Formation of Defects during Thermolysis of Powder Moldings," *J. Mater. Res.,* **11**, 830-840 (1996).

13. S. J. Lombardo and Z. C. Feng, "Determination of the Minimum Time for Binder Removal and Optimum Geometry for Three-Dimensional Porous Green Bodies," *J. Am. Ceram. Soc.,* **6** [12] 2087-2092 (2003).

14. S. J. Lombardo and Z. C. Feng, "Analytic Method for the Minimum Time for Binder Removal from Three-Dimensional Porous Green Bodies," *J. of Mat. Res.,* **18,** 2717-2723 (2003).

15. J. W. Yun and S. J. Lombardo, "Heat Transfer Effects in Porous Green Bodies During Binder Removal by Minimum Time Heating Cycles," *J. Am. Ceram. Soc.,* **89** [4] 1193-1199 (2006).

16. B. A. Meyer, and D. W. Smith, "Flow through Porous Media: Comparison of Consolidated and Unconsolidated Materials," *Ind. Eng. Chem. Fundam.*, **23**, 360-68 (1985).

17. S. J. Lukasiewicz and J. S. Reed, "Specific Permeability of Porous Compacts as Described by a Capillary Model," *J. Am. Ceram. Soc.,* **71** [11] 1008-1014 (1988).

18. K. B. Lee, and J. R. Howell, "Theoretical and Experimental Heat and Mass Transfer in Highly Porous Media," *Int. J. Heat Mass Trans.*, **34** [8] 2123-2132 (1991).

19. Y. Bao, and J. R. G. Evans, "Kinetics of Capillary Extraction of Organic Vehicle from Ceramic Bodies. Part 1: Flow in Porous Media ," *J. Eur. Ceram. Soc.*, **8**, 81-89 (1991).

20. J. S. Reed, "Liquid Permeability of Packed Particles: Why Perpetuate the Carmen-Kozeny Model?" *J. Am. Ceram. Soc.,* **76** [2] 547-548 (1993).

21. M. D. M. Innocentini, A. R. F. Pardo, V. R. Salvini, and V. C. Pandolfelli, "How Accurate is Darcy's Law for Refractories," *Am. Ceram. Soc. Bull.*, **78** [11] 64-68 (1999).

22. M. D. M. Innocentini, and V. C. Pandolfelli, "Permeability of Porous Ceramics Considering the Klinkenberg and Inertial Effects," *J. Am. Ceram. Soc.,* **84**, 941-944 (2001).

23. L. J. Klinkenberg, "The Permeability of Porous Media to Liquids and Gases*," Drill. Prod. Prac. API*, 200-213 (1941).

24. G. P. Brown, A. DiNardo, G. K. Cheng, and T. K. Sherwood, "The Flow of Gases in Pipes at Low Pressures," *J. Appl. Phys.,* **17**, 802-813 (1946).

25. D. S. Scott and F. A. L. Dullien, "Diffusion of Ideal Gases in Capillaries and Porous Solids," *AIChE J.*, **8** [1] 113-117 (1962).

26. D. S. Scott and F. A. L. Dullien, "The Flow of Rarefied Gases," *AIChE J.*, **8** [3] 293-297 (1962).

27. N. Wakao and J. M. Smith, "Diffusion in Catalyst Pellets," *Chem. Eng. Sci.*, **17**, 825-834 (1962).

28. N. Wakao, S. Ontani, and J. M. Smith, "Significance of Pressure Gradients in Porous Materials: Part 1. Diffusion and Flow in Fine Capillaries," *AIChE J.*, **11** [3] 435-439 (1965).

29. S. Ontani, N. Wakao, and J. M. Smith, "Significance of Pressure Gradients in Porous Materials: Part 2. Diffusion and Flow in Porous Catalysts," *AIChE J.*, **11** [3] 439-445 (1965).

CHAPTER 4

PERMEABILITY OF LAMINATED GREEN CERAMIC TAPES AS A

FUNCTION OF BINDER LOADING

4.1   INTRODUCTION

During binder removal from ceramic components, the permeability [1-6] of open pore green compacts may strongly control the rate at which the sample can be heated in order to avoid failure of the body [7-15].   The removal of binder with time both increases the porosity and changes the solid surface area to solid volume ratio within the porous medium; both effects will lead to changes in the permeability.   For multilayer ceramic structures, which are subjected to a lamination step, the permeability of laminated tapes will likely be different from that of the unlaminated tapes.

In previous work [16], we have developed a methodology for analyzing the permeability of porous green bodies as a function of binder loading. The methodology is based on analyzing flux data through a porous medium in order to determine which flow mechanisms—Knudsen, slip, or Poiseuille flow—are predominantly contributing to the flow behavior [17-23]. For the ceramic tapes analyzed therein, we showed that the controlling pore size was greater than 1 μm, and thus Poiseuille flow was the dominant transport mechanism. In light of this result, we could then analyze the flux data in terms of Darcy's law to obtain a permeability that was insensitive to the flow conditions, *i.e.*, was an intrinsic property of the composite ceramic-binder body.

In this work, we report the measurement of the flux through laminated green tapes as a function of binder content and then compare these results to what was obtained on unlaminated tapes.   As expected, the process of lamination changes attributes of the microstructure, and hence permeability of the tapes, as compared to unlaminated tapes. The permeability determined as a function of binder content is then related to other

microstructural characteristics of the green body such as the specific surface and tortuosity.

4.2   EXPERIMENTAL

The tape samples used in this study were prepared from barium titanate powder (Tamtron X7R 412H, Ferro Electronic Materials, Niagara Falls, NY), which has a mean particle diameter of 1.2 μm and specific surface area of 3.3 m^2/g.   To prepare slurries, 55.4 wt% barium titanate powder was mixed with 44.6 wt% of a binder solution (B73305 Ferro Corp., San Marcos, CA), which consists of 22 wt% poly(vinyl butyral) (PVB) and dioctyl phthalate (DOP) in a 6:4 weight ratio in a solvent mixture.   The slurry was ball milled, filtered, and then tape cast.   The tapes, which after drying had a thickness of approximately 125 μm, were then cut into samples.   The tape samples were then laminated in a press with heated platens at 7 MPa at 85°C for 10 minutes.   Mylar films of 75 μm thickness were used to prevent sticking to the top and bottom metal faces of the platens.   The initial volume fraction of porosity of the tapes was determined by the Archimedes's method, and was 0.20 ± 0.02 for unlaminated tapes and decreased to 0.15 ± 0.03 after the lamination step.

The total initial organic content of the substrates was 10.9% by weight, as determined by weight loss.   To prepare samples with lower binder contents, the laminated tapes were subjected to oxidation in air at temperatures between 150-200°C for times of 0.5-24 h.   Below 4 wt% binder, the samples were brittle and fractured during testing.   As binder was progressively removed by heating, the volume fraction of porosity was calculated from the known initial porosity and the weight loss.

The permeability measurements were performed by placing green tapes of disk geometry into a sample holder with an open area of 1.56 cm in diameter and sealing them

with a flexible o-ring.   The upstream pressure of nitrogen, P_1, was set by a pressure regulator, and the downstream pressure, P_2, could be adjusted by a valve after the sample holder.   After the valve, a flow meter was used to measure the volumetric flow rate, V_f, which was then converted to a molar flow rate, n, via the ideal gas law

$$n = \frac{P_f V_f}{RT_f} \qquad\qquad 4\text{-}1$$

where P is the pressure, R is the gas constant, T is the temperature, and the subscript f denotes the conditions at the flow meter.   The measured molar flux, N_m, through the area, A, of the substrate is then given by

$$N_m = n/A = u_o \rho \qquad\qquad 4\text{-}2$$

where u_o is the superficial velocity and $\rho = P/RT$ is the molar density.

4.3   RESULTS AND DISCUSSION

The microstructures of unlaminated and laminated green tapes at high (10.9 wt%), medium (~6 wt%), and low (0 wt%) binder content are shown in Fig. 4.1.   These samples were prepared by fracturing substrates that had been first submerged in liquid nitrogen.   For the unlaminated tapes with 10.9 wt% binder, regions of sample rich and poor in binder are evident.   Large pores or channels of micron size and irregular shape appear throughout the sample, and many of these pores are separated by distances of many multiples of the ceramic particle diameter.   No clear characteristic single pore dimension is evident, but rather a distribution of pore sizes is seen.   For the tapes of intermediate binder loading, more pores of smaller size are evident with smaller separation distances between them.   For the tapes with no binder, pores appear to be located between almost every individual ceramic particle.   Large sized channels, however, are still evident.   For the laminated tapes, the same progression in the appearance of the pore space with binder loading occurs, but both the volume fraction of pores and the pore size may be slightly smaller for the laminated tapes as compared to the unlaminated tapes, although this is difficult to say with certainty based on the appearance of the microstructures alone.
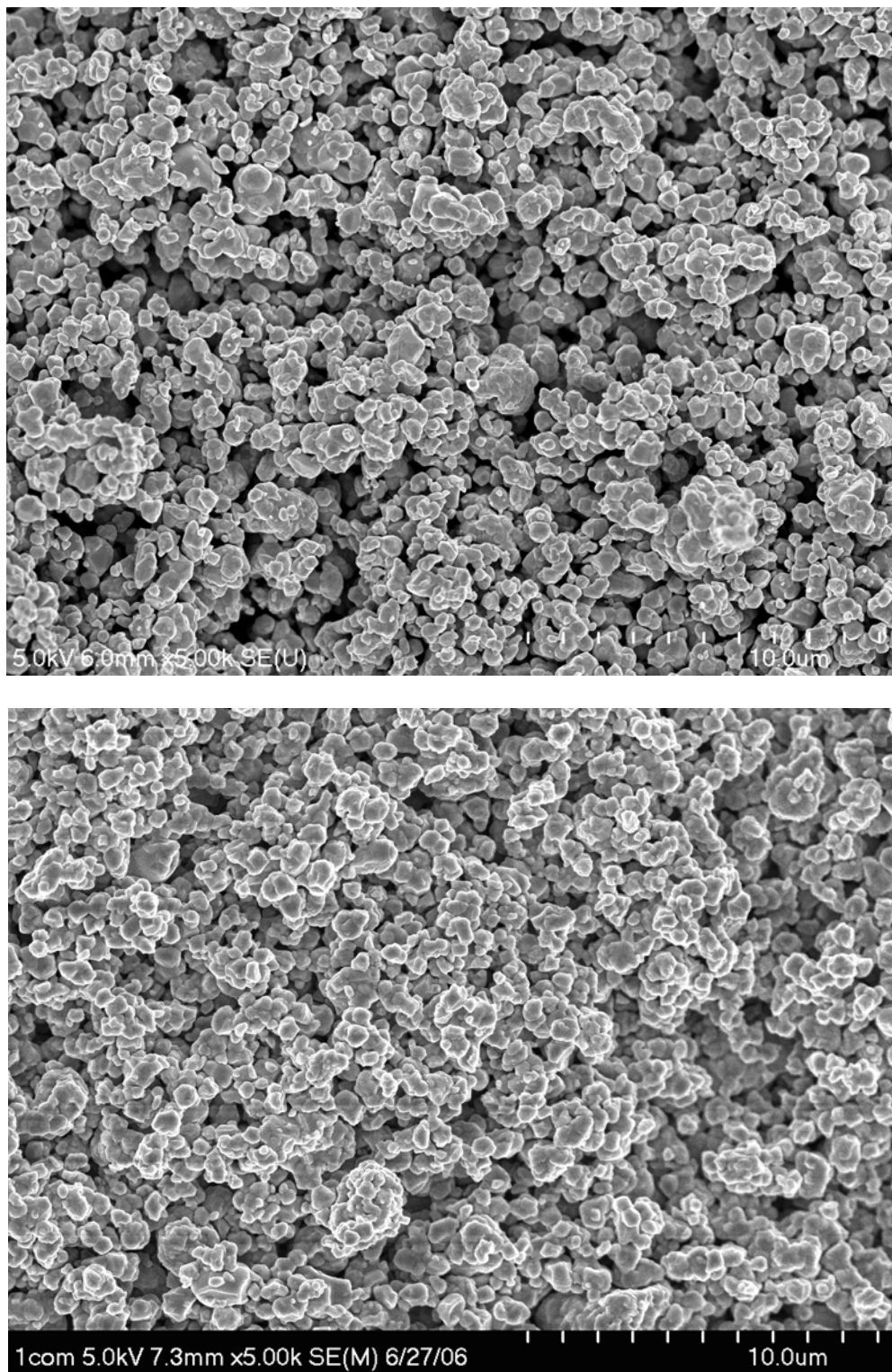
Figure 4.1 a) Scanning electron micrographs of the cross sections of unlaminated (top) and laminated (bottom) tapes at low (0 wt%) binder loadings.
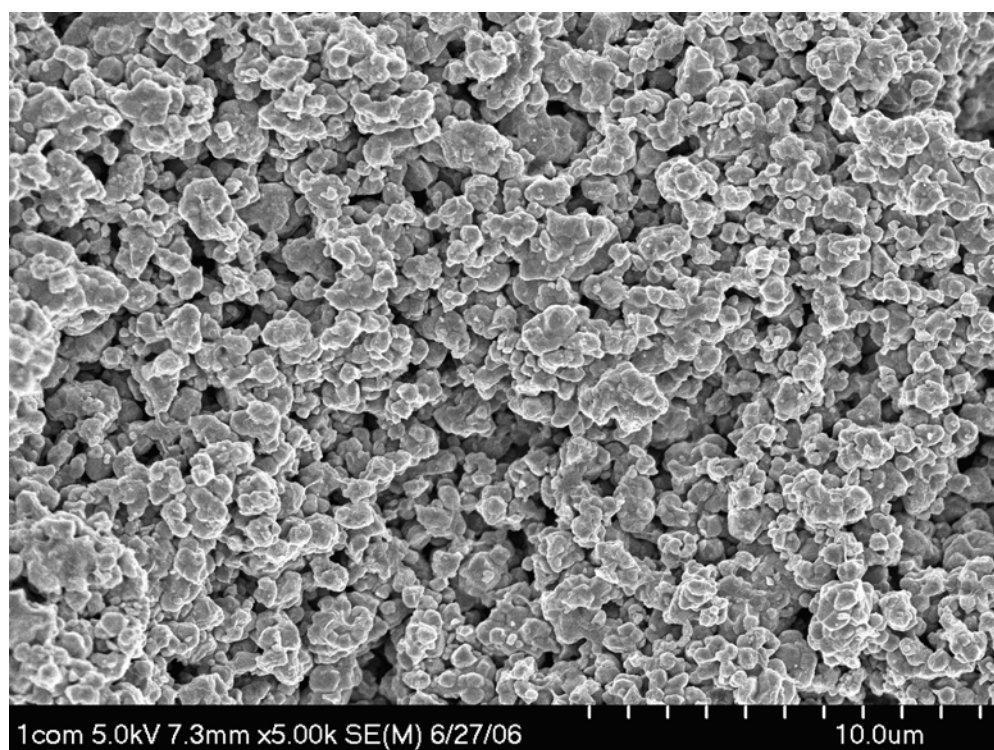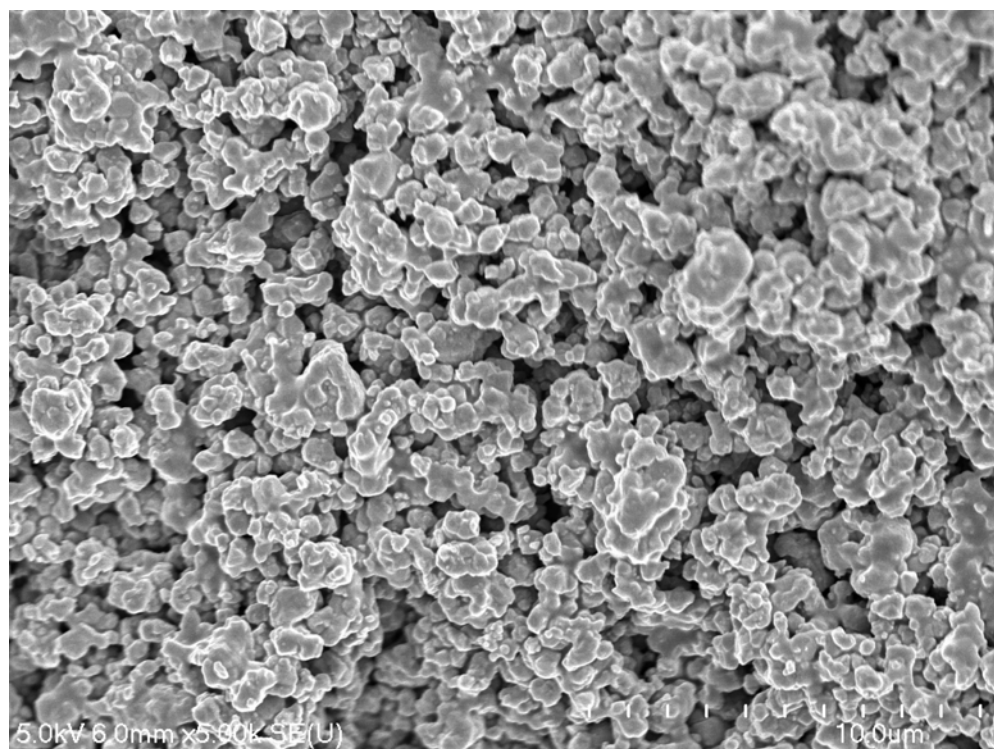
Figure 4.1 b) Scanning electron micrographs of the cross sections of unlaminated (top) and laminated (bottom) tapes at intermediate (~6 wt%) binder loadings.
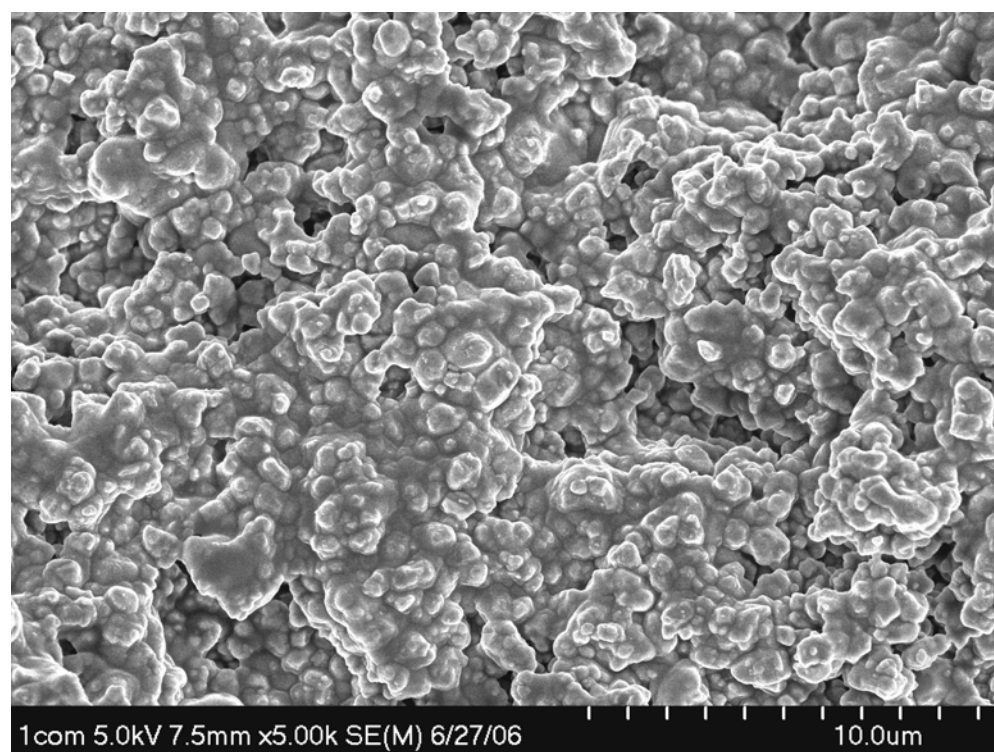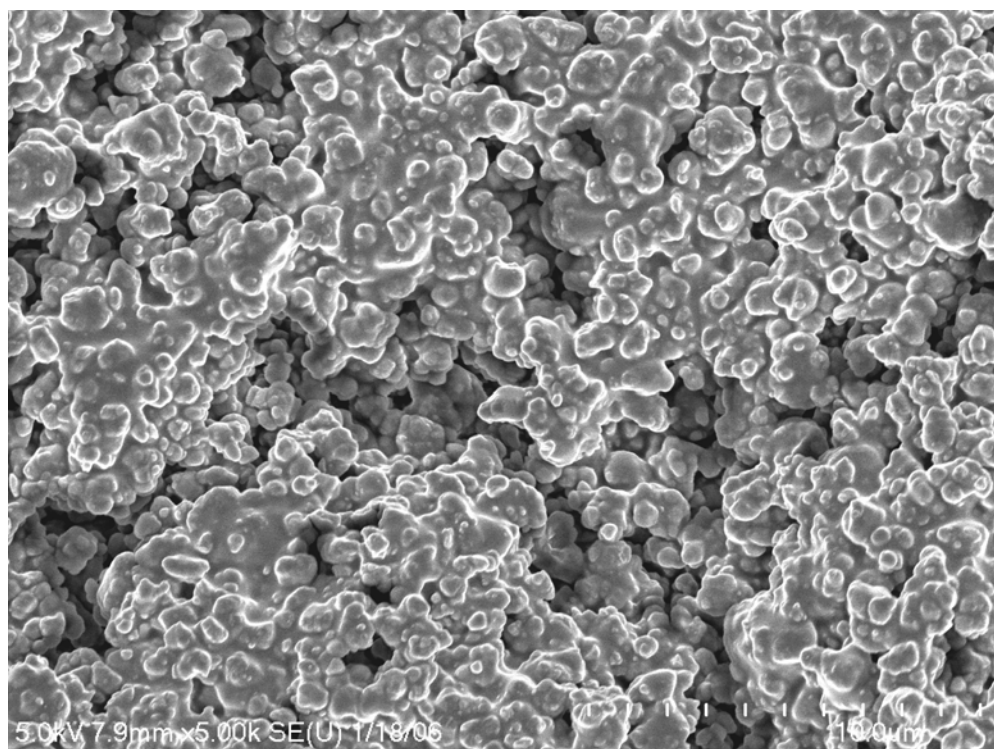
Figure 4.1 c) Scanning electron micrographs of the cross sections of unlaminated (top) and laminated (bottom) tapes at high (10.9 wt%) binder loadings.

For flow in narrow capillaries at low Reynold's number, Knudsen, slip, and Poiseuille flow may all occur. The relative contributions of each of these flow mechanisms depends on the ratio of the pore size to the mean free path of the gas-phase molecules:

$$\lambda = RT / \sqrt{2} \, \pi d^2 N_A P \qquad\qquad\qquad 4\text{-}3$$

where d is the molecular diameter and N_A is Avogadro's number.

For a single capillary of radius, r, the molar flux, N, in the x-direction is given by [22]

$$N = -\frac{K_T}{RT} \frac{dP}{dx} \qquad\qquad\qquad 4\text{-}4$$

The quantity K_T consists of contributions from Knudsen, slip, and Poiseuille flow as

$$K_T = \left(\frac{1}{1+2r/\lambda}\right) \left[\frac{2}{3} r \bar{v}\right]_{Knudsen} + \left(\frac{1}{1+\lambda/2r}\right)\left[\left(\frac{\pi r \bar{v}}{6}\right)_{Slip} + \left(\frac{r^2 P}{8\mu}\right)_{Poiseuille}\right] \qquad 4\text{-}5$$

where μ is the viscosity of the gas. The average velocity of the gas-phase species is

$$\bar{v} = (8RT/\pi M)^{1/2} \qquad\qquad\qquad 4\text{-}6$$

where M is the molecular weight. Upon integration of Eqs. 4-5 from P_1 to P_2 over the length, L, the total flux can be represented by three terms

$$N = N_{Knudsen} + N_{Slip} + N_{Poiseuille} \qquad\qquad\qquad 4\text{-}7$$

which are given by [16]

$$N_{Knudsen} = \frac{2}{3} \frac{C_1}{C_2 L} \left[\ln\left(\frac{1+C_2 P_1}{1+C_2 P_2}\right)\right] \qquad\qquad\qquad 4\text{-}8$$

$$N_{Slip} = \frac{\pi}{6} \frac{C_1}{L} \left[(P_1 - P_2) - \frac{1}{C_2} \ln\left(\frac{1+C_2 P_1}{1+C_2 P_2}\right)\right] \qquad\qquad\qquad 4\text{-}9$$

$$N_{Poiseuille} = \frac{C_3}{2L} \left[(P_1^2 - P_2^2) - \frac{2}{C_2}(P_1 - P_2) + \frac{2}{C_2^2} \ln\left(\frac{1+C_2 P_1}{1+C_2 P_2}\right)\right] \qquad 4\text{-}10$$

where $C_1 = r\bar{v}/RT$, $C_2 = 2\sqrt{2}r\pi d^2 N_A/RT$, and $C_3 = r^2/8\mu RT$.

Figure 4.2 shows a plot of the three contributions to the total flux from Eq. 4-7 as a function of the pore size for $\mu = 1.76 \times 10^4$ g/cm-s and $d=0.4$ nm, *e.g.*, values appropriate for nitrogen gas. Depending on the pore size, Knudsen, slip, or Poiseuille flow can dominate the flow behavior. As the pore size increases from 0.1 μm to 1 μm, a transition takes place from slip-dominated to Poiseuille-dominated flow.
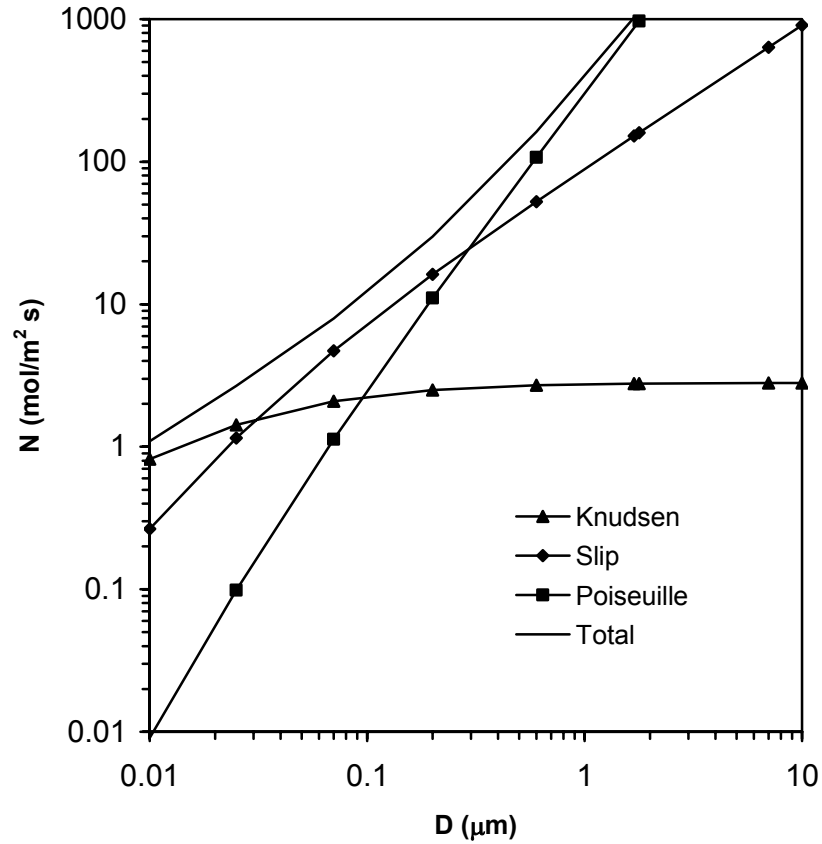
Figure 4. 1 Contributions of Knudsen, slip, and Poiseuille flow to the total flux versus pore diameter for nitrogen gas in a single capillary.

To determine the characteristic pore size which governs the flow in a porous medium, the normalized flux, $N/\Delta P$, can be plotted versus the average pressure, P_{ave}. When such experiments are conducted at higher pressures where Knudsen flow can be neglected, a linear relation is obtained [20]

$$\frac{N}{\Delta P} = AP_{ave} + B \qquad\qquad 4\text{-}11$$

where A is the slope and B is the intercept.   The ratio of

$$\frac{A}{B} = \frac{3\bar{r}}{4\pi\mu\bar{v}} \qquad\qquad 4\text{-}12$$

can then be used to determine the characteristic pore diameter, $D = 2\bar{r}$.

Figure 4.3a shows a plot of the normalized flux versus P_{ave} for 1-5 tapes with 10.9 weight% binder laminated at 7 MPa at 85°C for 10 minutes.   For each number of laminated tapes, a linear relationship is obtained with different slopes and intercepts, which suggests that the characteristic pore size is changing as well.   As the number of laminated tapes increases, however, the normalized flux appears to approach a constant value for four or more laminated tapes.   This effect may arise because as more tapes are stacked, the load during lamination becomes more evenly distributed.

Figure 4.3b shows the characteristic pore size determined by Eq. 4-12.   As the number of laminated tapes increases, the characteristic pore size decreases from 0.8 μm to 0.5 μm.   For the smallest pore size, the results in Fig.4.2 indicate that Poiseuille flow is responsible for more than two-thirds of the total flux, a contribution which increases rapidly as the pore size increases.
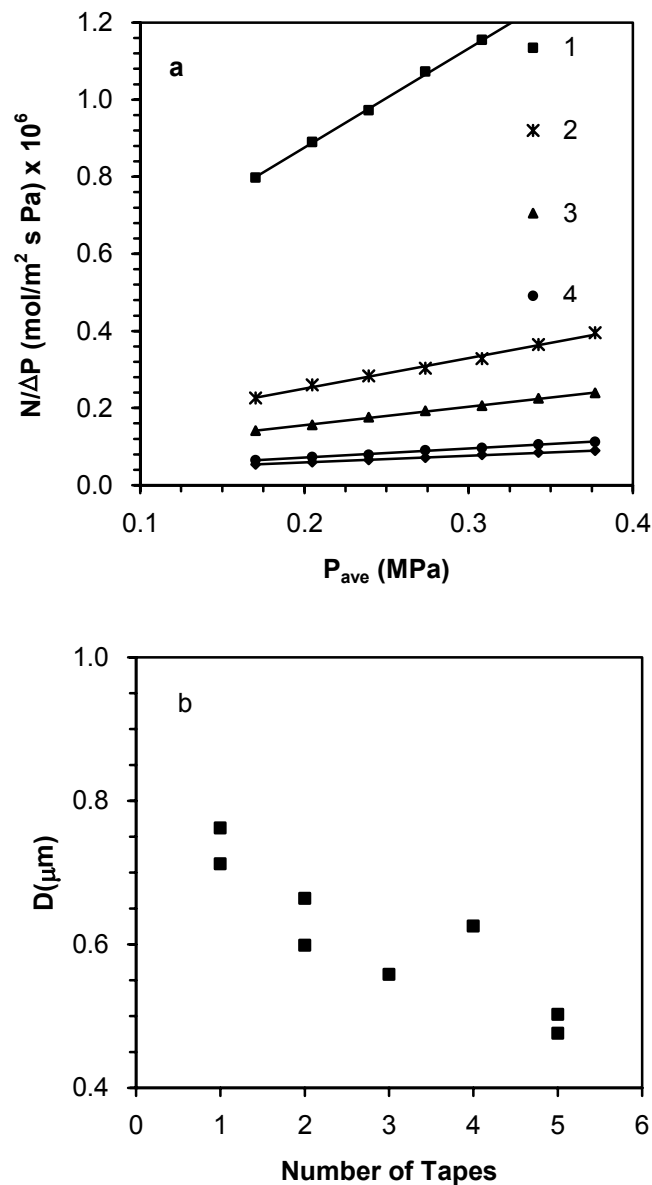
Figure 4. 2   a) Normalized flux versus average pressure at 10.9 wt% binder for 1-5 tapes laminated at 7 MPa at 85°C for 10 min. b) Characteristic pore diameter versus number of laminated tapes.

The normalized flux was then determined as a function of binder content for five laminated tapes.   Figure 4.4a shows that for all binder loadings, the normalized flux varies again linearly with the average pressure, and that the normalized flux increases with decreasing binder loading.   From this linear behavior, values of *A* and *B* were obtained in order to determine the characteristic pore size.   Figure 4.4b shows that the

characteristic pore size increases from 0.5 μm to above 1 μm as binder is removed. Below 6 weight% binder, no data are shown because of the brittle nature, and hence fracture during handling, of samples low in binder. Figure 4.4b also shows that characteristic pore size versus binder loading for five laminated tapes is smaller by 50-100% as compared to the pore size of a single unlaminated tape [16]. Thus, the process of lamination influences both the absolute characteristic pore size and how the characteristic pore size evolves as binder is removed.

The results for the pore size in Fig. 4.4b, when considered in light of the trends in Fig. 4.2, indicate that Poiseuille flow is the major contributor to the flux at all binder loadings. As a consequence, the permeability, κ, can be represented by Darcy's law for flow in porous media as

$$u_o = -\frac{\kappa}{\mu}\frac{dP}{dx} \qquad\qquad 4\text{-}13$$

Combining Eqs. 4-2 and 4-13 leads to the permeability as

$$\kappa = -\mu\frac{N_m}{\rho}\left(\frac{dP}{dx}\right)^{-1} \qquad\qquad 4\text{-}14$$

At steady state flow conditions for a compressible fluid, the pressure across the sample varies from P_1 to P_2 as [1]

$$P = \left[\frac{P_2^2 - P_1^2}{L}x + P_1^2\right]^{1/2} \qquad\qquad 4\text{-}15$$

When the ideal gas law is used to describe the molar density, Eqs. 4-14 and 15 simplify to

$$\kappa = -2RTN_m\mu\frac{L}{P_2^2 - P_1^2} \qquad\qquad 4\text{-}16$$

For κ to be a useful quantity, *e.g.*, an intrinsic property of the ceramic-binder composite,

changing the flow conditions or the sample thickness should not influence its value.
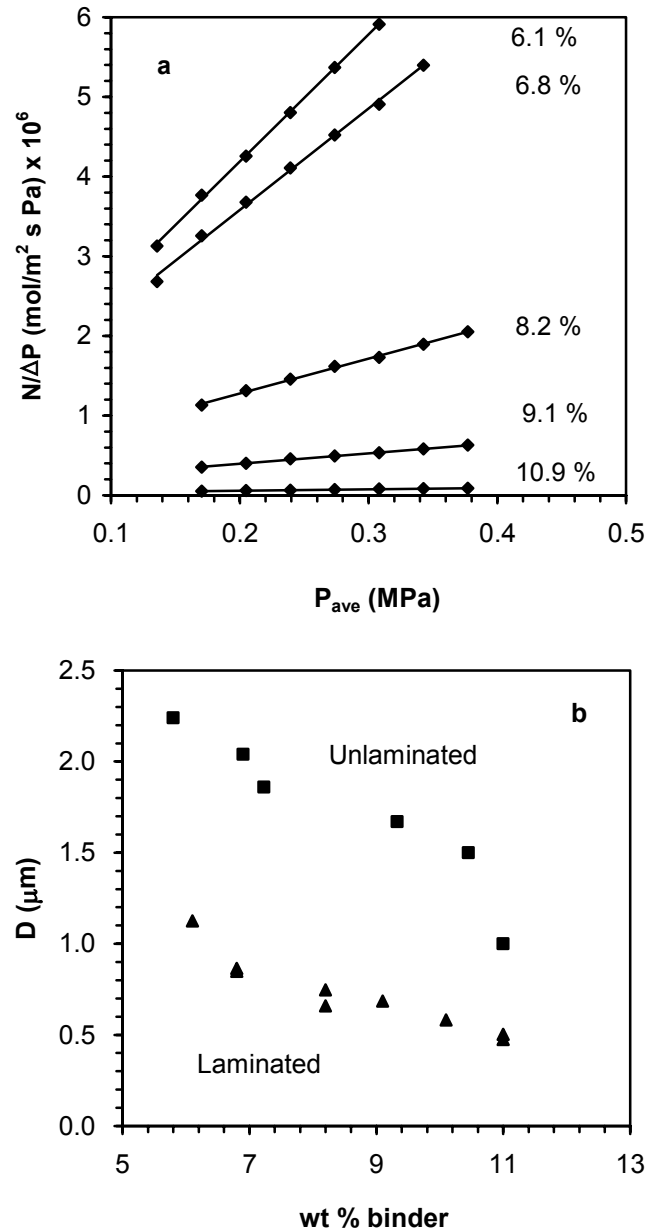
Figure 4. 3   a) Normalized flux versus average pressure at different binder loadings for five tapes laminated at 7 MPa at 85°C for 10 min.   b) Characteristic pore diameter versus binder loading for 5 laminated and 1 unlaminated tape.

To test the sensitivity of the permeability of tape samples to changes in flow conditions, the following types of experiments were conducted.   For the first type, the

permeability of unlaminated stacks of tapes was compared to that of laminated stacks of tapes at different binder loadings. Figure 4.5 shows that for unlaminated stacks of tapes, the permeability is independent of the number of stacked tapes, in spite of the fact that different pressures were used depending on the number of stacked layers. For laminated tapes, the permeability appears to be approaching a constant value with increasing number of tapes, which is a direct consequence of the limiting behavior seen in Figure 4.3a for the normalized flux with increasing number of laminated tapes. It also appears that the plateaus in permeability occur for different number of laminated tapes, depending on binder loading; this behavior may have as its origin either non-uniformity during lamination or during binder removal. We also can see that for a given binder loading, the permeability of five laminated tapes is less than 20% of the unlaminated tapes.
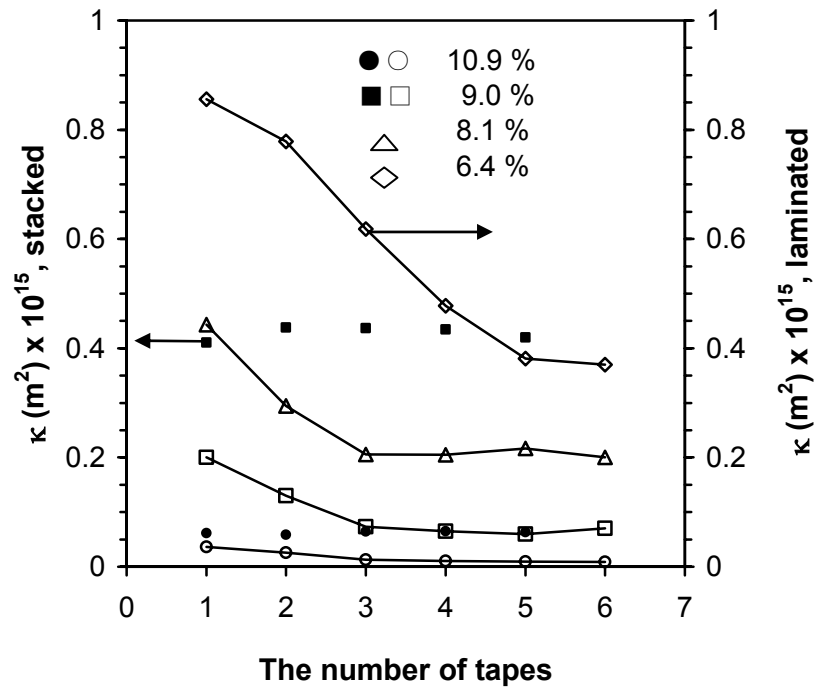
Figure 4. 4 Permeability comparison at different binder loadings of stacked tapes (filled symbols, left-hand axis) versus tapes laminated (open symbols, right-hand axis) at 7 MPa at 85°C for 10 min.

Figure 4.6 shows the permeability of five laminated tapes versus upstream pressure and for different pressure drops. The permeability is relatively insensitive to the upstream pressure and increases with decreasing binder loading. The results in Figs. 4.5 and 4.6 thus indicate that the permeability is not strongly dependent on the flow conditions after more than four tapes are laminated together.
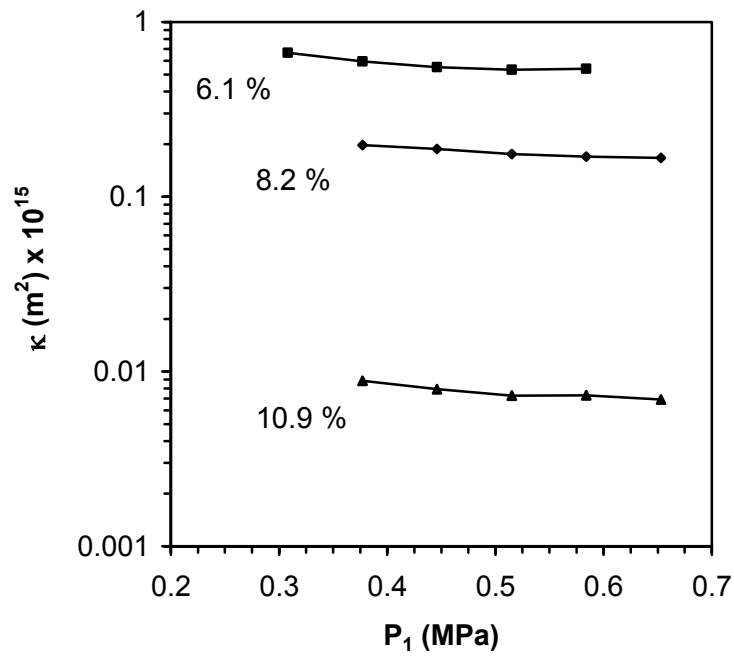
Figure 4. 5   Permeability versus upstream pressure of five tapes laminated at 7 MPa at 85°C for 10 min for 3 different binder loadings.   The pressure drop, ΔP, is 0.28 MPa for 10.9 and 8.2 wt% binder samples and 0.14 MPa for 6.1 wt % binder samples.

Figure 4.7 compares the permeability of 1-5 laminated tapes as a function of binder loading. As the binder loading decreases from 10.9 to 5 wt%, the permeability increases by a factor of approximately 50. We also see once again that the permeability decreases as the number of laminated tapes increases and approaches a constant value as

more than four tapes are laminated together. At low binder loadings, no data are again shown because of the brittle nature, and hence fracture, of the samples after a large amount of binder is removed.
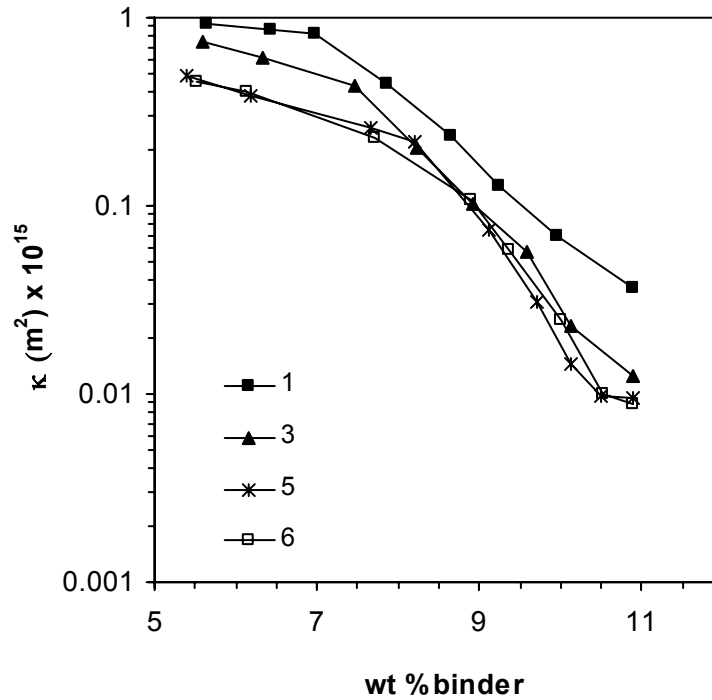
Figure 4. 6   Permeability versus binder loading for different numbers of tapes laminated at 7 MPa at 85°C for 10 min.

The permeability values presented above are determined solely from flux data. To relate these permeabilities to microstructural attributes of the tapes, we first relate the measured flux from an experiment to the flux from the single capillary model, modified by a function of the porosity as

$$N_m = u_o \rho = N \cdot f(\varepsilon) \qquad\qquad 4\text{-}17$$

Although the function $f(\varepsilon)$ is generally not known, it has alternatively been represented as proportional to ε in Ref. [10] and to ε^2 in Ref. [21].   As we have done earlier for

unlaminated tapes [16], we let $f(\varepsilon)=2\varepsilon^2/k$, where k is a constant to account for tortuosity and constrictions.   We further proceed to define a specific surface (surface area per unit solid volume), S, in terms of an equivalent pore diameter, $D=4r$, where r is the hydraulic radius, as

$$S = \frac{4\varepsilon}{(1-\varepsilon)D}$$
<div align="right">4-18</div>

With this definition for S combined with the term for Poiseuille flow from Eq. 4, we then obtain that the permeability is given by

$$\kappa = \frac{\varepsilon^4}{k(1-\varepsilon)^2 S^2}$$
<div align="right">4-19</div>

which is similar in form to the expression obtained by Meyer and Smith [24], who observed that for bodies consisting of a single type of particle, the tortuosity increased with decreasing porosity.

To calculate values of κ from the microstructural features in Eq. 4-19, values of k and S are thus required.   Values of S were obtained from Eq. 18 with the values of pore diameter, D, obtained from Fig. 4.4b.   Values of k were next determined by fitting measured flux data with Eq. 4-17 along with the proposed form of $f(\varepsilon)$.   Tables 4.1 and 4.2 summarize the values obtained in this manner for five laminated tapes as compared to the values obtained previously for unlaminated tapes.   The values of S determined are higher by approximately 50% for the laminated tapes as compared to the unlaminated tapes, and in both cases S does not vary strongly with binder content. The quantity k varies much more strongly, and nonmonotonically, with binder content for both types of tape samples and for a given binder content is larger for the unlaminated samples.   The

large *k* values determined suggest a very tortuous path or small constrictions between pores or some combination thereof; this behavior may be consistent with the appearance of the microstructures of the tapes seen in Fig. 4.1.

Table 4. 1   Porosity, pore size, specific surface, and tortuosity versus binder loading for laminated tapes.

Binder	ε	D	S $\times$ 10^{-6}	k
(wt%)	(-)	(μm)	(m^{-1})	(-)
10.9	0.15	0.48	1.47	35
10.1	0.17	0.58	1.41	32
9.1	0.20	0.68	1.47	20
8.2	0.23	0.74	1.61	10
6.8	0.27	0.86	1.72	7
6.1	0.29	1.12	1.46	10

Table 4. 2   Porosity, pore size, specific surface, and tortuosity versus binder loading for unlaminated tapes.

Binder	ε	D	S $\times$ 10^{-6}	k
(wt%)	(-)	(μm)	(m^{-1})	(-)
10.9	0.20	1.00	1.00	48
10.5	0.22	1.50	0.73	46
9.3	0.25	1.67	0.78	30
7.2	0.30	1.85	0.95	18
6.9	0.31	2.00	0.91	20
5.8	0.34	2.05	1.03	24
4.9	0.37	2.13	1.10	28
3.4	0.41	2.20	1.27	36

Figure 4.8 compares the permeabilities determined from Eq. 4-16 from flux data versus binder content to permeabilities calculated from Eq. 4-19 with the values of *S* and *k* from Tables 4.1 and 4.2. In general, the values of the permeabilities obtained from

microstructural attributes (Eq. 4-19) agree quite well with those obtained from measured flux data (Eq. 4-16), even though the permeability values from microstructural features were not directly fitted to the experimental values.   When directly fitted to each other, then even better agreement can be obtained [16].   Figure 4.8 also shows that laminated tapes are less permeable by a factor of about five as compared to unlaminated tapes.
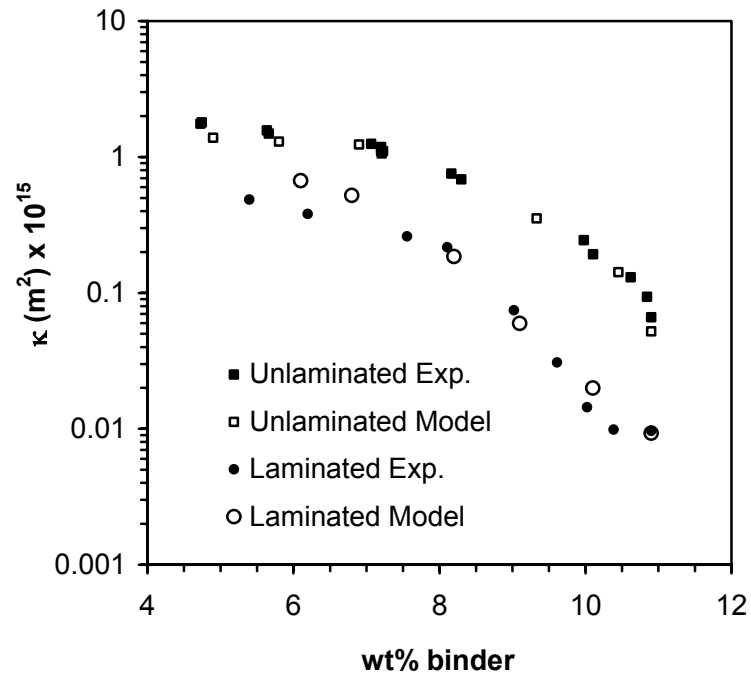
Figure 4. 7   Comparison of the permeability determined from flux data (Eq. 4-16) and from microstructural attributes (Eq. 4-19) for laminated and unlaminated tapes versus

Figure 4.9 compares the permeability of the laminated and unlaminated tapes as a function of volume fraction of porosity.   Although the general overall trends in permeability remain the same as compared to Fig. 4.8, the two sets of permeability data are now shifted relative to each other as a consequence of the difference in starting porosity arising from the lamination step.   These data show that in terms of the volume

fraction of porosity, the permeability of the laminated samples begins at lower volume

fractions of porosity, as compared to the unlaminated samples.   At intermediate void

fractions, the permeabilities of both types of tapes become more equivalent, and then

diverge as more binder is removed.
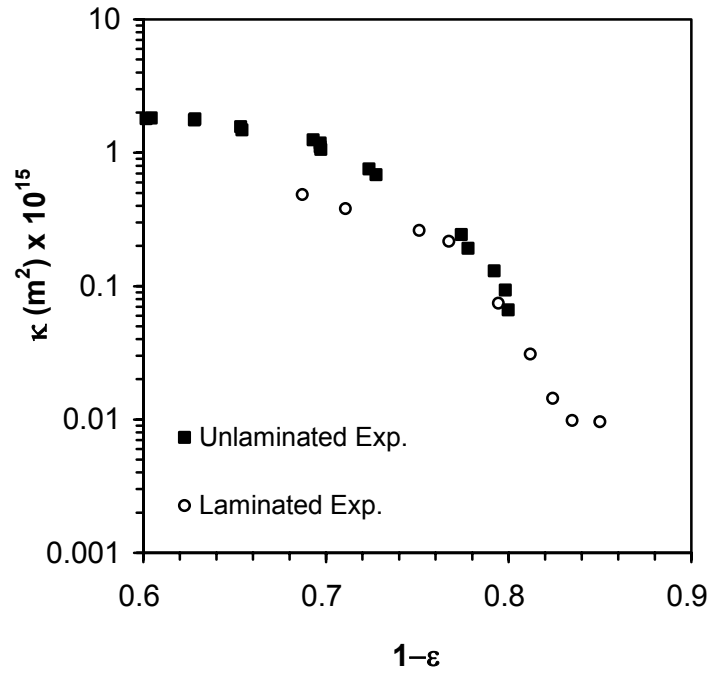
Figure 4. 8   Comparison of the permeability determined from flux data of laminated and unlaminated tapes versus pore volume fraction.

The results in Figs. 4.8 and 4.9 and in Tables 4.1 and 4.2 thus indicate that the

processing step of lamination has a pronounced effect on magnitude and on the evolution

of permeability within the green bodies as a function of binder content. These differences

can then be rationalized in terms of differences in the microstructural features of porosity,

specific surface, and tortuosity and constrictions.

4.4   CONCLUSIONS

The permeability of laminated green tapes as a function of binder loading has been determined.   The flux through the laminated tapes is seen to depend on the number of tapes laminated together, and is seen to approach a constant value for four or more laminated tapes.   The permeability of laminated tapes is approximately a factor of five smaller as compared to the unlaminated tapes.   The characteristic pore size governing the flow behavior through the laminated tapes was determined to be greater than $0.5 \ \mu\text{m}$, which indicates that Poiseuille flow is the dominant flow mechanism, and thus Darcy's law for flow in porous media can be used to describe the permeability. The permeability of the tapes was also expressed in terms of microstructural attributes in terms of the porosity, specific surface, and a term to account for tortuosity and constrictions.

4.5   REFERENCES

1. A.E. Scheidegger, *The Physics of Flow Through Porous Media,* University of Toronto Press, Toronto, 1974.

2. F. A. L. Dullien, *Porous Media: Fluid Transport and Pore Structure,* Academic Press, New York, 1979.

3. J. Bear, and J.-M. Buchlin, *Modelling and Applications of Transport Phenomena in Porous Media*, Kluwer Academic Publishers, Dordrecht, 1991.

4. M. Sahimi, *Flow and Transport in Porous Media and Fractured Rock*, VCH, Weinheim, 1995.

5. P.C. Carman, *Flow and Transport Through Porous Media*, Academic Press, New York, 1956.

6. H. David, "A Review of Terminology Pertaining to Darcy's Law and Flow through Porous Media," *Journal of Porous Media*, **6** [2] 87-97 (2003).

7. R. M. German, "Theory of Thermal Debinding," *Int. J. Powder Metall.*, **23** [4] 237-245 (1987).

8. J. A. Lewis, "Binder Removal From Ceramics," *Annual Rev. Mater. Sci.*, **27**, 147-173 (1997).

9. G. Y. Stangle, and I. A. Aksay, "Simultaneous Momentum, Heat and Mass Transfer With Chemical Reaction in a Disordered Porous Medium: Application to Binder Removal From a Ceramic Green Body," *Chem. Eng. Sci.*, **45**, 1719-1731 (1990).

10. D-S. Tsai, "Pressure Buildup and Internal Stresses During Binder Burnout: Numerical Analysis ," *AIChE J.*, **37** [4] 547-554 (1991).

11. S. A. Matar, M. J. Edirisinghe, J. R. G. Evans, and E. H. Twizell, "Effect of Porosity Development on the Removal of Organic Vehicle from Ceramic or Metal Moldings," *J. Mater. Res.*, **8**, 617-625 (1993).

12. J. H. Song, M. J. Edirisinghe, J. R. G. Evans, and E. H. Twizell, "Modeling the Effect of Gas Transport on the Formation of Defects during Thermolysis of Powder Moldings," *J. Mater. Res.,* **11**, 830-840 (1996).

13. S. J. Lombardo and Z. C. Feng, "Determination of the Minimum Time for Binder Removal and Optimum Geometry for Three-Dimensional Porous Green Bodies," *J. Am. Ceram. Soc.,* **6** [12] 2087-2092 (2003).

14. S. J. Lombardo and Z. C. Feng, "Analytic Method for the Minimum Time for Binder

Removal from Three-Dimensional Porous Green Bodies," *J. of Mat. Res.,* **18,** 2717-2723 (2003).

15. J. W. Yun and S. J. Lombardo, "Heat Transfer Effects in Porous Green Bodies During Binder Removal by Minimum Time Heating Cycles," *J. Am. Ceram. Soc.,* **89** [4] 1193-1199 (2006).

16. J. W. Yun and S. J. Lombardo, "Permeability of Green Tapes as a Function of Binder Loading," *J. Am. Ceram. Soc.,* 90 [2] 456-461 (2006).

17. L. J. Klinkenberg, "The Permeability of Porous Media to Liquids and Gases*," Drill. Prod. Prac. API*, 200-213 (1941).

18. G. P. Brown, A. DiNardo, G. K. Cheng, and T. K. Sherwood, "The Flow of Gases in Pipes at Low Pressures," *J. Appl. Phys.,* **17**, 802-813 (1946).

19. D. S. Scott and F. A. L. Dullien, "Diffusion of Ideal Gases in Capillaries and Porous Solids," *AIChE J.*, **8** [1] 113-117 (1962).

20. D. S. Scott and F. A. L. Dullien, "The Flow of Rarefied Gases," *AIChE J.*, **8** [3] 293-297 (1962).

21. N. Wakao and J. M. Smith, "Diffusion in Catalyst Pellets," *Chem. Eng. Sci.*, **17**, 825-834 (1962).

22. N. Wakao, S. Ontani, and J. M. Smith, "Significance of Pressure Gradients in Porous Materials: Part 1. Diffusion and Flow in Fine Capillaries," *AIChE J.*, **11** [3] 435-439 (1965).

23. S. Ontani, N. Wakao, and J. M. Smith, "Significance of Pressure Gradients in Porous Materials: Part 2. Diffusion and Flow in Porous Catalysts," *AIChE J.*, **11** [3] 439-445 (1965).

24. B. A. Meyer, and D. W. Smith, "Flow through Porous Media: Comparison of Consolidated and Unconsolidated Materials," *Ind. Eng. Chem. Fundam.*, **23**, 360-68 (1985).

CHAPTER 5

EFFECT OF LAMINATION CONDITIONS ON THE

PERMEABILITY AND ADHESION STRENGTH OF GREEN

CERAMIC TAPES

5.1   INTRODUCTION

During the processing of layered ceramic components which are formed from laminated tapes, the conditions of lamination are likely to influence the subsequent properties and thus processing of the ceramic green body.   Two such properties of the laminated tapes are the permeability [1-16] and adhesion strength [17-22].   High adhesion strength is desirable for avoiding delamination during the binder removal heating cycle and to allow for a high degree of bonding to form between layers during the sintering cycle.   From the viewpoint of permeability, high permeability is desirable after lamination so that the green body can be heated more quickly during the binder removal step.

In earlier work, we have shown how the permeability [23-26] of open pore green laminated tapes is substantially less than that of the unlaminated tapes at one set of lamination conditions. It is also likely that the adhesion strength between layers will depend on the lamination conditions.   In this work, we examine the effects of lamination time, temperature, and pressure on the permeability and adhesion strength of green ceramic tapes.   We also show the effect of tape orientation on both properties.   Finally, we show that the yield of multilayer ceramic structures depends on both the conditions of lamination and on the heating rate used in the binder removal heating cycle.

5.2   EXPERIMENTAL

Green ceramic tapes were prepared from barium titanate powder (Tamtron X7R 412H, Ferro Electronic Materials, Niagara Falls, NY), which has a mean particle diameter of 1.2 μm and specific surface area of 3.3 m^2/g.   The slurry preparation consisted of mixing 55.4 weight% barium titanate powder with 44.6 weight% of a binder solution (B73305 Ferro Corp., San Marcos, CA), which is 22% by weight poly(vinyl butyral) (PVB) and dioctyl phthalate (DOP) in a 6:4 weight ratio in a solvent mixture. The slurry was ball milled, filtered, and then tape cast.   The tapes after drying had a thickness of approximately 140 μm. The total organic content of the substrates was 10.9% by weight, as determined by weight loss.   To prepare samples with lower binder contents, oxidation in air was used at temperatures between 150-200°C for times of 0.5-7 h.

The tape samples were laminated using a 25 ton press (Model 2518, Carver, Inc., Wabash, IN) with heated platens over a range of times, temperatures, and loads.   A stack of tapes was placed on the lower platen, which was already at the desired temperature, and then the load was applied and held for a fixed amount of time.   The load was converted to a pressure by using the nominal area of the face of the tapes to which the load was applied.

The adhesion strength of the laminated tapes was determined in the following fashion from peel tests.   Green tapes of 2 cm width × 10 cm length × 0.01 cm thickness were partially separated with a layer of Mylar of 0.08 mm thickness, as indicated in Fig. 5.1, and then laminated.   The two parts of the T-shaped sample not laminated were then

placed in grips and and subjected to load with a tensile tester (TA TX Plus Texture Analyzer, Stable Micro Systems Ltd., Surrey, UK). During testing, the top crosshead moved and the load was measured as a function of displacement for a constant crosshead speed of 0.4 cm/s.
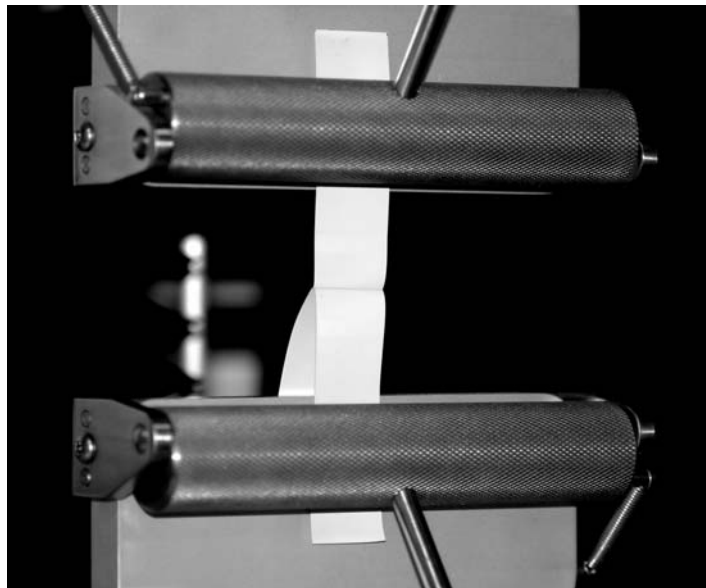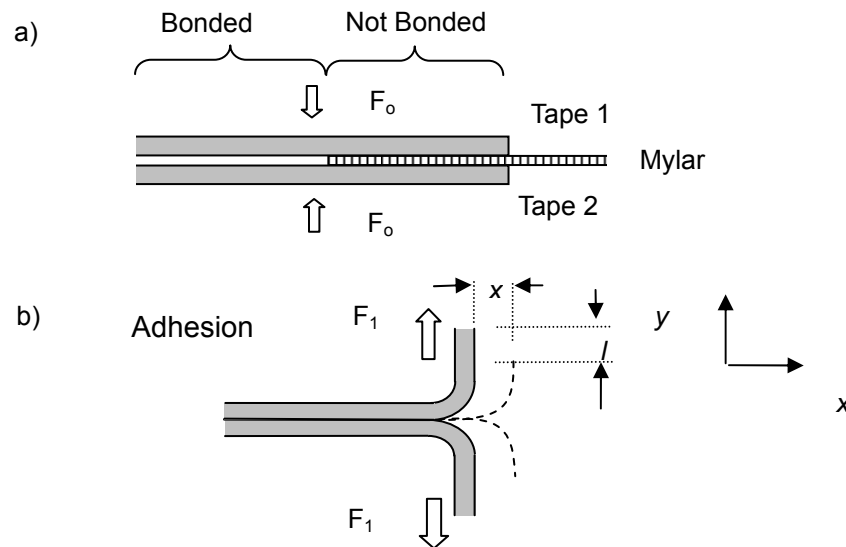
Figure 5. 1   a) Schematic diagram of the lamination procedure used to fabrication T-shaped samples and, b) schematic diagram of T-peel test, and photo of the tensile tester used to determine the peel force.

The peel energy for a T-peel test can be found from the work done by machine as

$$W_{machine} = 2F_1 l$$ 5-1

where F_1 is the applied force and l is the distance traveled by the crosshead. The total work done on the sample is given by the energy for peeling, E_{peel}, and the energy of straining, E_{strain}, as

$$W_{sample} = E_{peel} + E_{strain} = F_p bx + W_\lambda bxt$$ 5-2

where b is width of sample, t is thickness of sample, F_p is the peel force, and W_λ is the work of straining. Because of conservation of energy, the machine work and sample work are equal:

$$2F_1 l = F_p bx + W_\lambda bxt$$ 5-3

If the extension due to strain is negligible, l and x (see Fig. 5.1) will be equal and the strain energy will be negligible. The peel force, F_p, is then

$$F_p = \frac{2F_1}{b}$$ 5-4

and has units of N/m.

The permeability measurements were performed by placing green tapes of disk geometry into a sample holder with an open area of 1.56 cm in diameter and sealed with a flexible o-ring (see Fig. 5.2). The upstream pressure of nitrogen, P_1, was set by a pressure regulator, and the downstream pressure, P_2, could be adjusted by a valve after the sample holder. The volumetric flow rate, V_f, which was measured by a flow meter, was converted to a molar flow rate, n, via

$$n = \frac{P_f V_f}{RT_f}$$ 5-5

where P is the pressure, R is the gas constant, T is the temperature, and the subscript f denotes the conditions at the flow meter. The measured molar flux, N_m, through the area, A, of the substrate is then given by

$$N_m = n/A = u_o \rho \qquad \text{5-6}$$

where u_o is the superficial velocity and $\rho = P/RT$ is the molar density. For flux governed mainly by flow in porous media, which is the case here [16], Darcy's law for flow in porous media is valid:

$$u_o = -\frac{\kappa}{\mu} \frac{dP}{dx} \qquad \text{5-7}$$

where μ is the viscosity. The permeability κ for a compressible fluid can then be determined from

$$\kappa = -2RTN_m \mu \frac{L}{P_2^2 - P_1^2} \qquad \text{5-8}$$
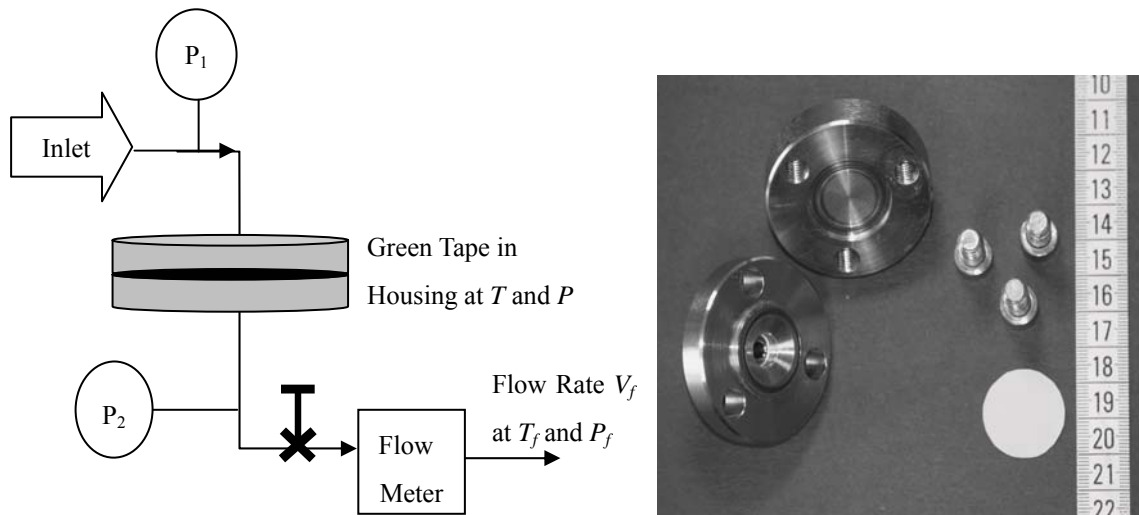
Figure 5. 2   Schematic of apparatus used to determine the permeability and photo of a tape and the sample holder for permeability measurements.

5.3   RESULTS AND DISCUSSION

The microstructures of the top and bottom surfaces of the green tapes are shown in Fig. 5.3.   No strong difference is observed in the microstructures, but slightly more binder may be present on the bottom face.

The microstructures of cross-sections of tapes laminated at the most aggressive conditions of 7 MPa at 85°C for 10 min, the intermediate conditions of 3.5 MPa at 65°C for 5 min, and the least agressive conditions of 1.8 MPa at 50°C for 2 min are shown in Fig. 5.4 for the green and sintered body.   The sintered samples were prepared by freezing substrates in liquid nitrogen and then fracturing and polishing them.   Large pores or channels of micron size and irregular shape appear throughout the sample, and many of these pores are separated by distances of many multiples of the ceramic particle diameter.   The presence of the lamination line is vaguely evident for the tapes laminated at the least aggressive conditions and not at all visible for the tapes laminated at the most aggressive conditions.
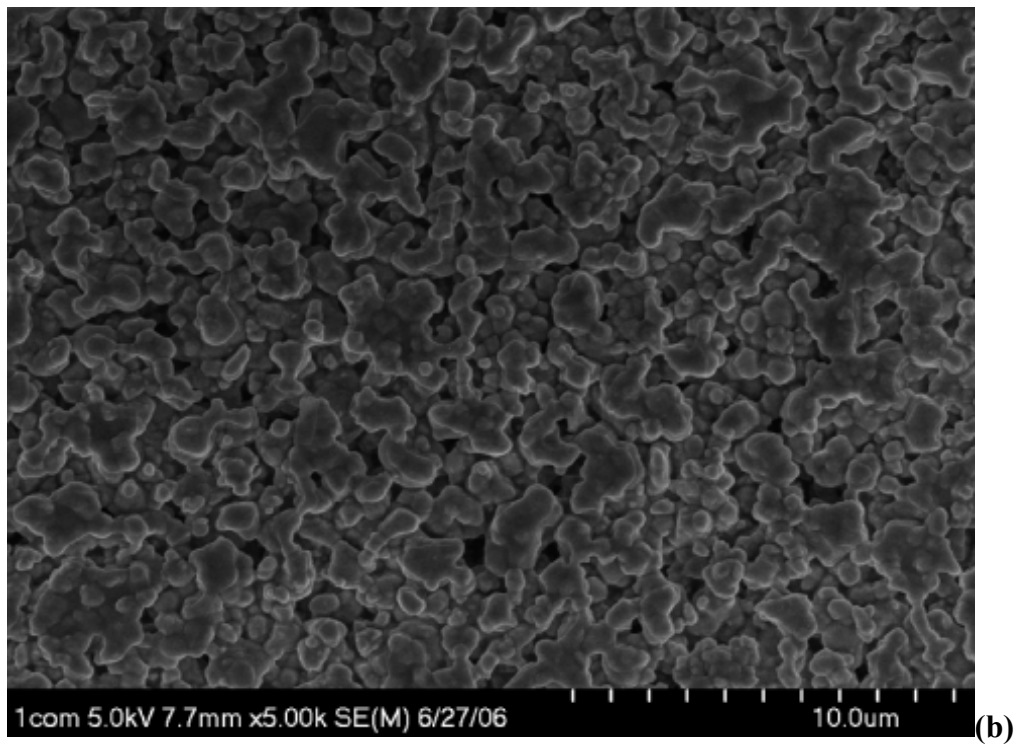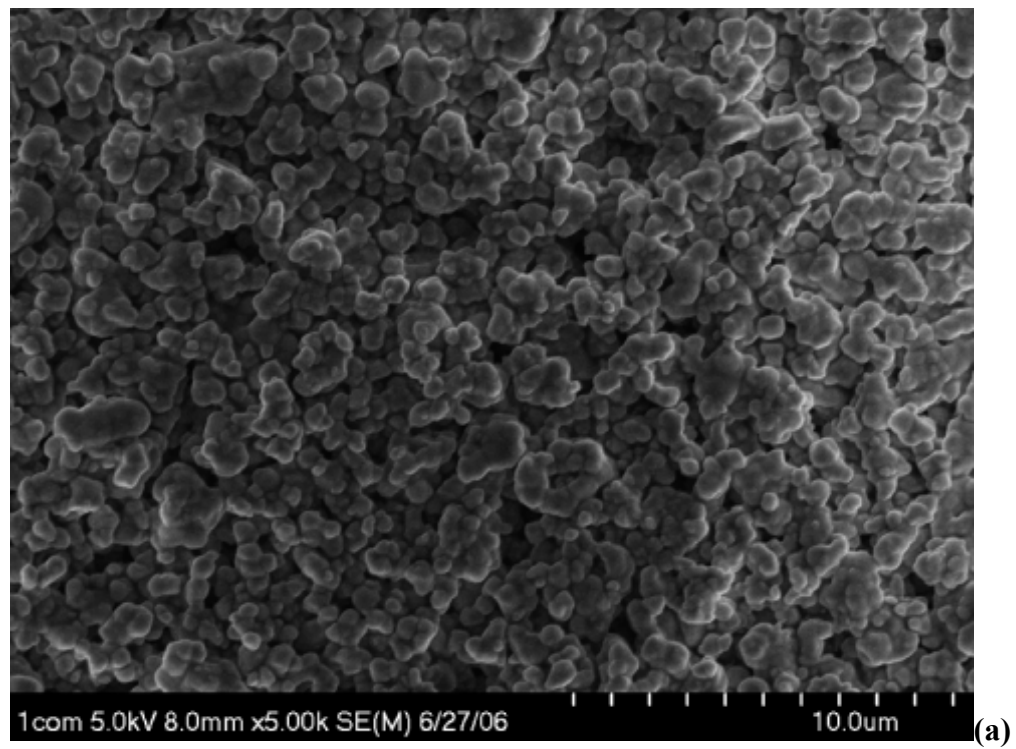
Figure 5. 3   Scanning electron micrographs of unlaminated green tapes a) top surface, b) bottom surface.

BaTiO3 5.0kV 9.2mm x400 SE(M) 7/6/06   100um **(a-1)**

BaTiO3 5.0kV 6.3mm x500 SE(M) 7/11/06   100um **(a-2)**

BaTiO3 5.0kV 9.4mm x400 SE(M) 7/6/06   100um   **(b-1)**

BaTiO3 5.0kV 6.4mm x500 SE(M) 7/11/06   100um   **(b-2)**

BaTiO3 5.0kV 8.7mm x400 SE(M) 7/6/06   100um   (c-1)

BaTiO3 5.0kV 6.4mm x500 SE(M) 7/11/06   100um   (c-2)
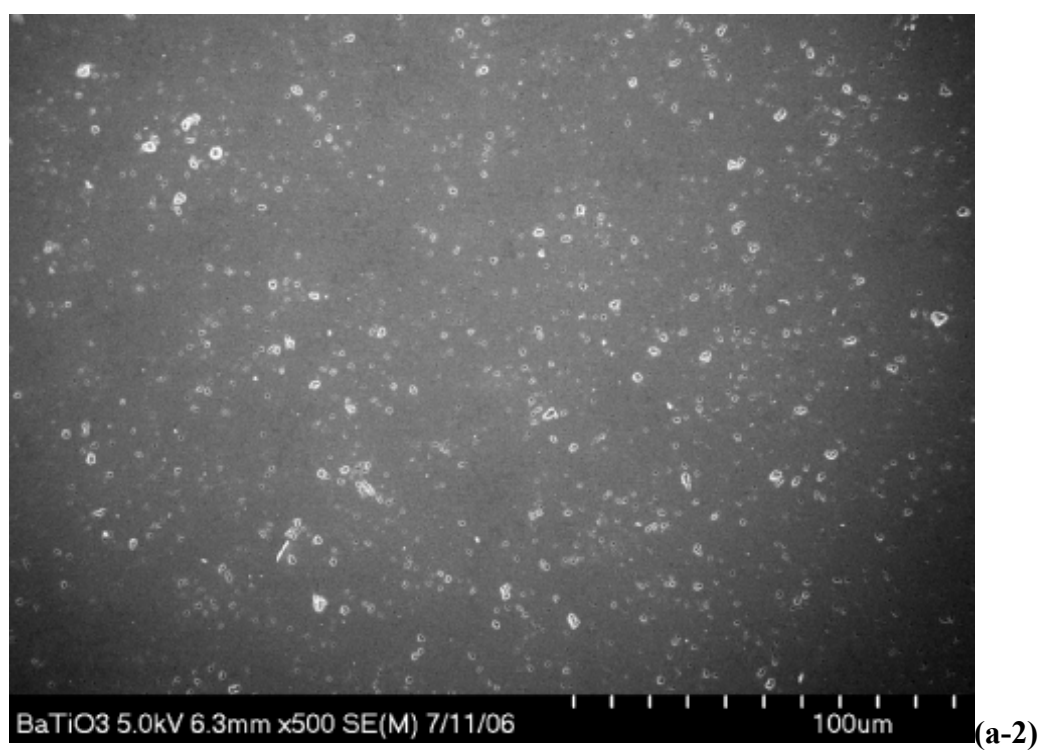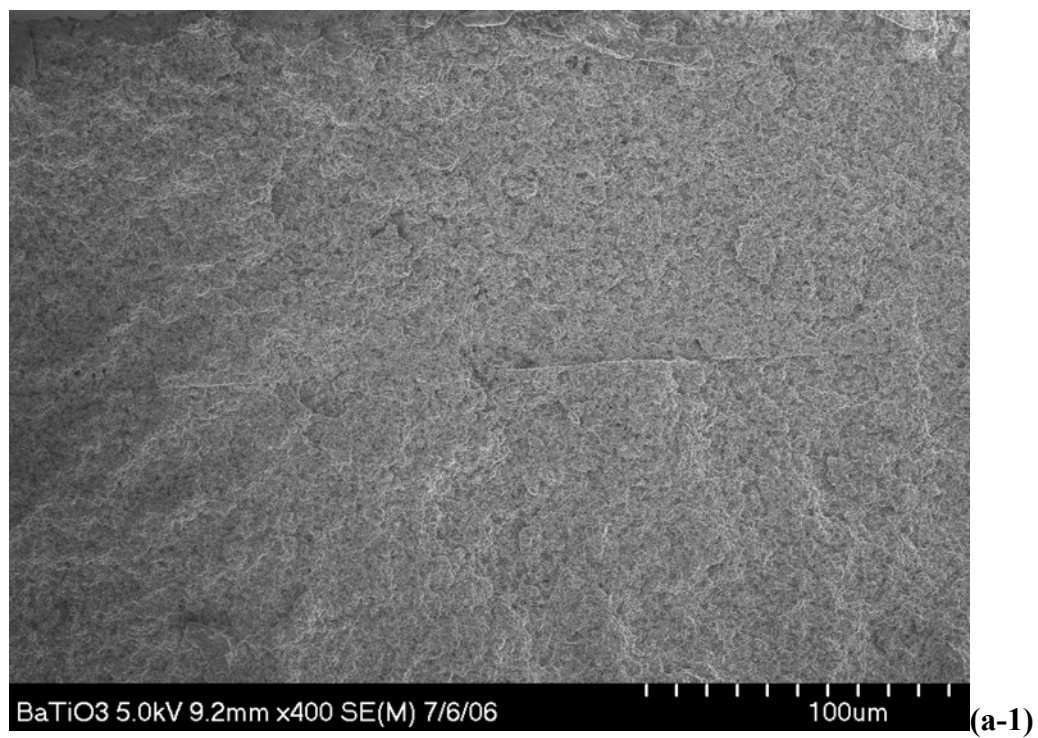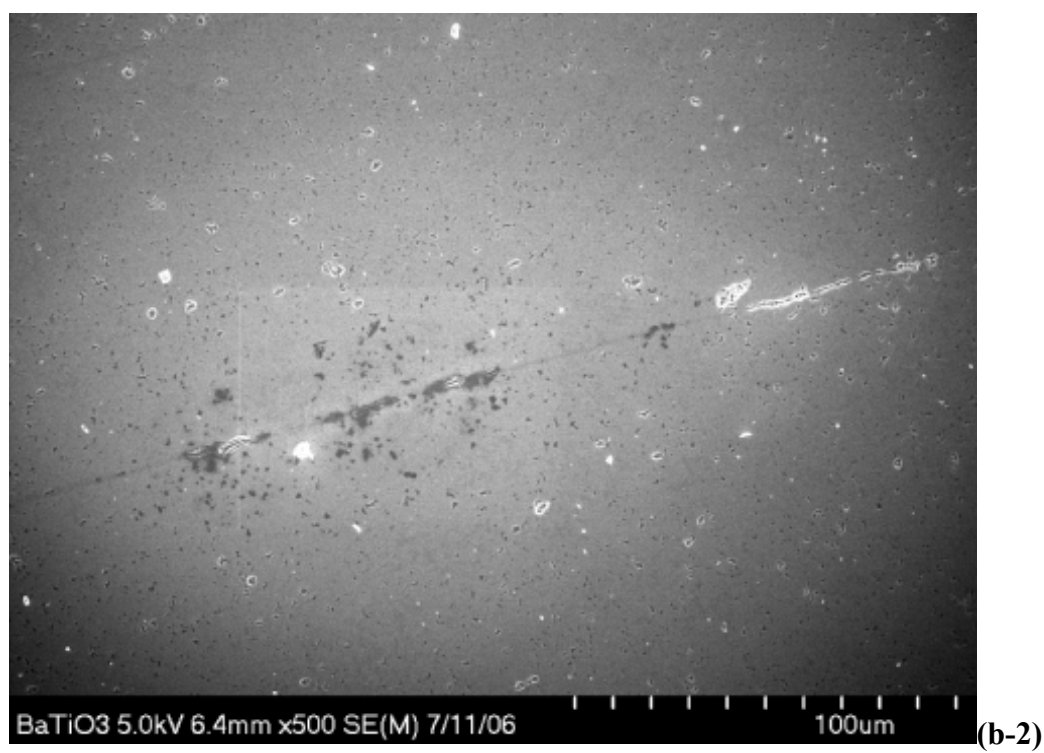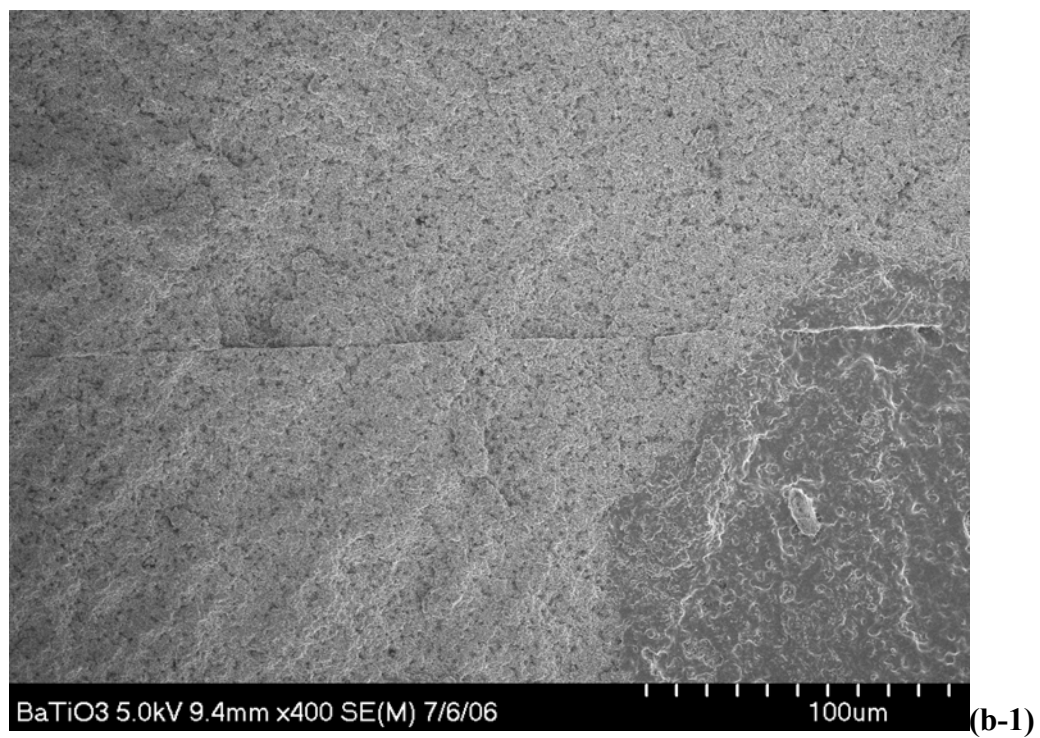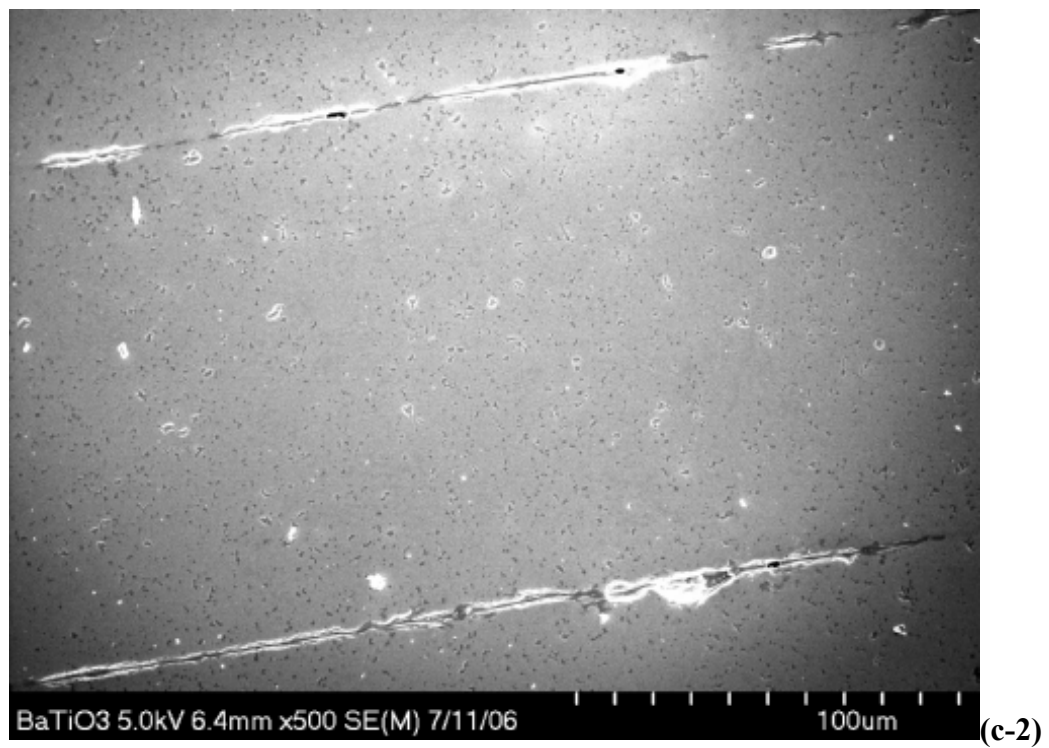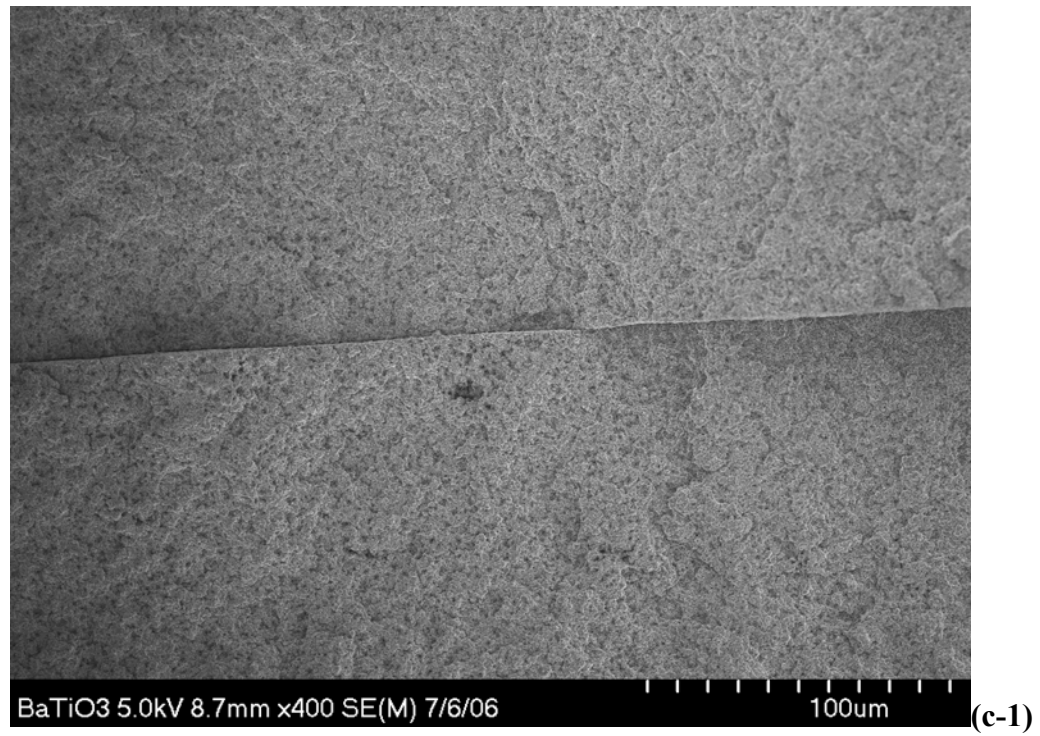
Figure 5. 4   Scanning electron micrographs of the cross view of green tapes(1) and sintered tapes(2) laminated at (a) maximum conditions (7MPa, 85 ^{o}C, 10 min, (b) intermediate conditions (3.5 MPa, 65 ^{o}C, 5 min), (c) lower conditions (1.8 MPa, 50 ^{o}C, 2 min).

The permeability of samples is shown in Fig. 5.5 for tapes with 10.9 weight% binder laminated at 7 MPa at 85°C for 10 minutes. Shown are the results of 5 specimens tested in different lamination orientations of top faces to top faces (t-t), top face to bottom face (t-b), and bottom face to bottom face (b-b). Although there is no strong dependence of the mean permeability on the orientation of the samples during lamination, the scatter in the mean permeability is less for the samples laminated in a top face to bottom face fashion.
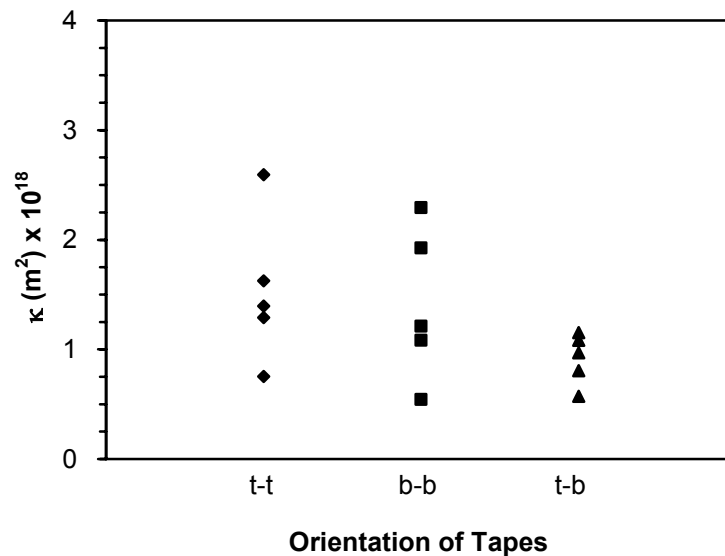
Figure 5. 5   Permeability versus tape orientation for two tapes laminated at 7 MPa at 85 °C for 10 min.

Figure 5.6a illustrates the room temperature permeability through tapes laminated at 7 MPa as a function of lamination temperature for different lamination times. At low lamination temperatures, the permeability does not depend strongly on the lamination temperature or time. With increasing lamination temperature above 35°C, the permeability begins to decrease, and a decrease by nearly three orders of magnitude is evident for tapes held for 10 minutes at the highest lamination temperature. Figure 5.6b

shows how the permeability varies with lamination temperature for different lamination pressures at 10 min. Once again, the permeability decreases strongly at higher temperatures, and this decrease is most pronounced at a lamination pressure of 7 MPa.
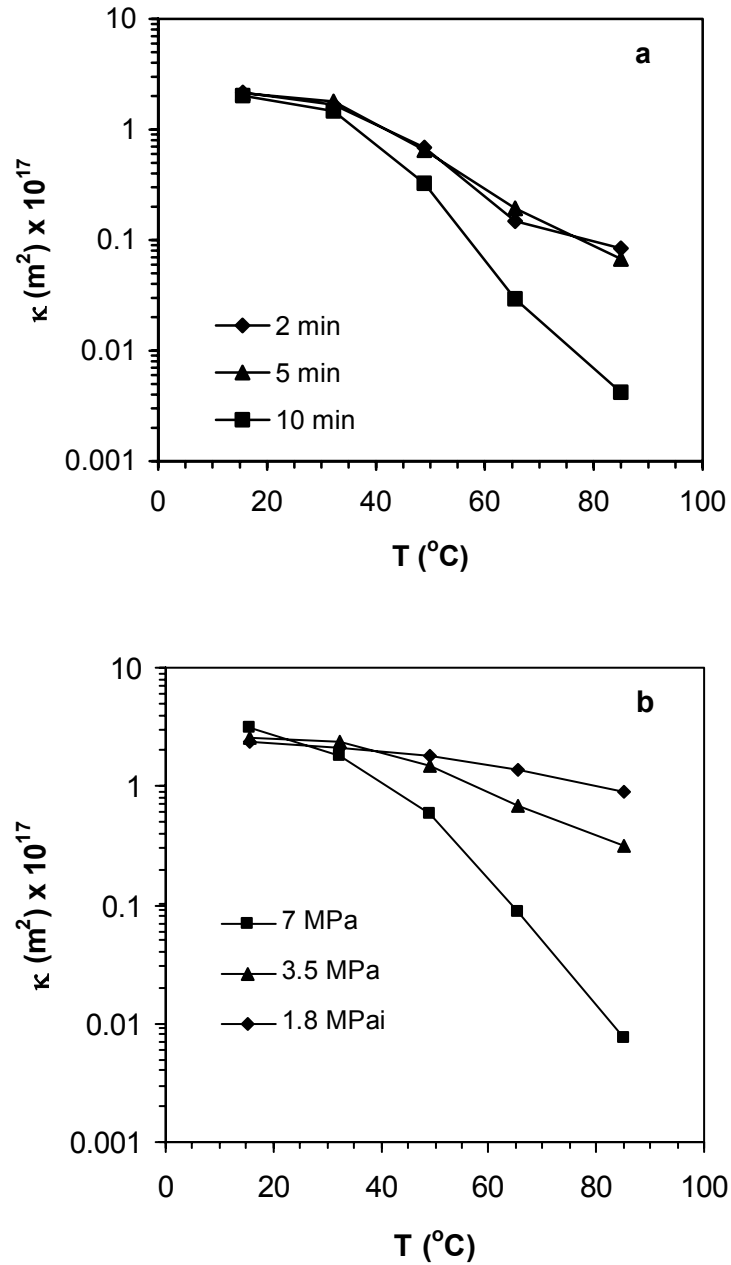
Figure 5. 6   a) Permeability versus temperature of two tapes laminated a) at 7 MPa for different times, and b) for 10 min at different pressures.

The peel force versus displacement curves are shown in Fig. 5.7 for tapes laminated at 7 MPa at 85°C for 10 minutes.   Each curve is the average of 3-5 specimens tested in different lamination orientations of t-t, t-b, and b-b. Initially, for all three lamination orientations, the force rises in a linear manner, reaches a local maximum, and then experiences a relatively constant peel force versus displacement.   Near the end of each test, local or global maxima or minima are also observed.   The adhesion strength is customarily taken as the initial maximum achieved, although the plateau regions are also indicative of the same ordering in adhesion strength in that the highest adhesion strength corresponds to the samples laminated in a b-b fashion, and the lowest adhesion strength arises for samples laminated t-t.
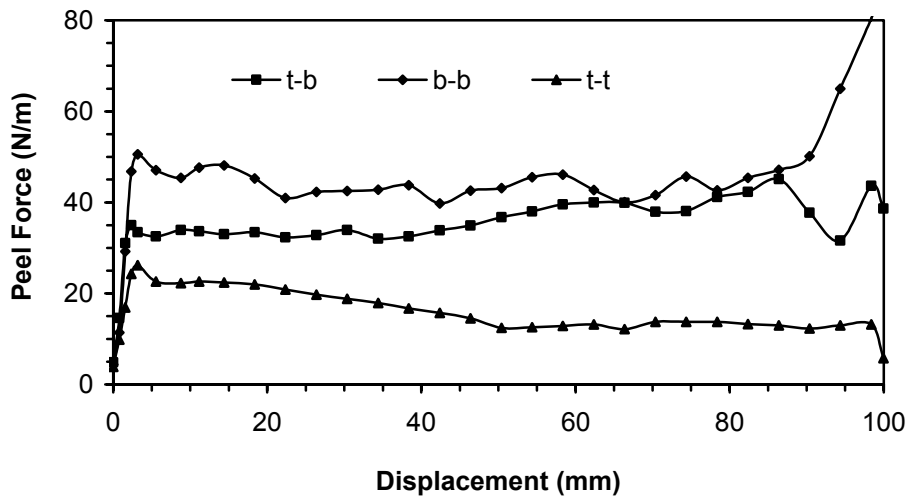
Figure 5. 7 Peel force versus displacement for two tapes laminated at 7 MPa at 85 °C for 10 min in different orientations.   The curves are the results of the averages of 3-5 samples

The average peel force versus displacement curves for samples laminated at different pressures at 85°C for 10 min are shown in Fig. 5.8a.   With increasing

lamination pressure, the peel force varies by approximately a factor of three over the range of conditions examined here. Figure 5.8b shows the effect of lamination temperature on the force versus displacement for samples laminated at 7 MPa for 10 minutes. With increasing lamination temperature, the peel force increases by a factor of three over the range of conditions examined here. The effect of lamination time is illustrated in Fig. 5.8c for samples laminated at 7 MPa at 85°C. With increasing lamination time, the peel force increases. The results in Fig. 5.8 thus indicate that observable differences arise in the adhesion behavior depending on the lamination conditions, and that the initial maximum in the peel force is a good indicator of the adhesion strength.

Figure 5.9 summarizes the adhesion strength and permeability versus lamination conditions. For all lamination conditions, the permeability decreases with increasing lamination time, temperature, and pressure, whereas the adhesion strength increases. The results in Fig. 5.9 thus indicate that a compromise exists in the selection of the lamination conditions. Higher lamination conditions of time, temperature, and pressure lead to better adhesion between layers, which may lead to improved yield during binder removal. These same lamination conditions, however, lead to less permeability in the green body, with concomitant slower heating cycles necessary to avoid pressure buildup and failure.
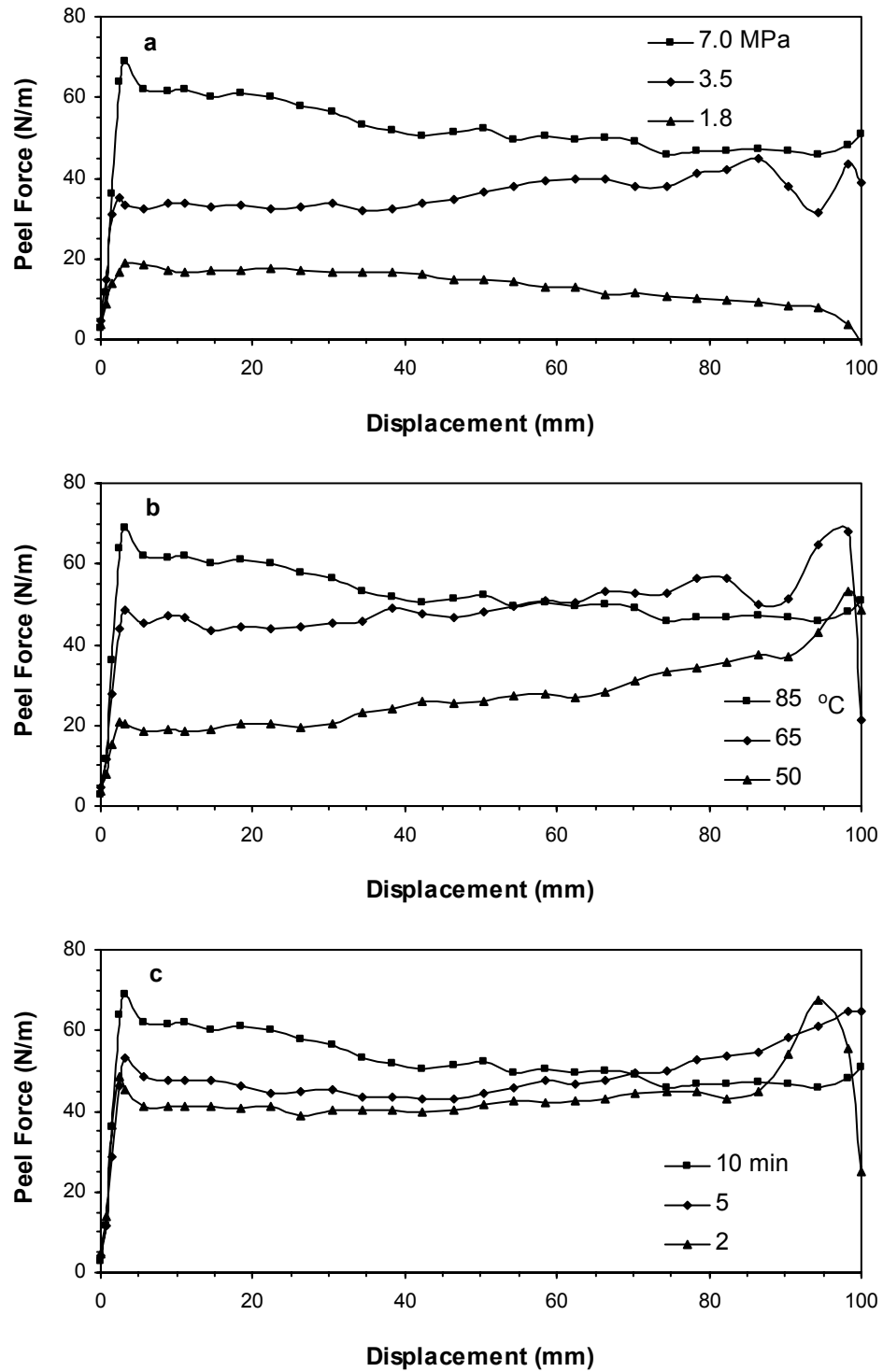
Figure 5. 8   Average peel force with displacement for tapes laminated at a) different pressures at 85°C for 10 min, b) at different temperatures at 7 MPa for 10 min, and c) at different times at 7 MPa at 85 °C.
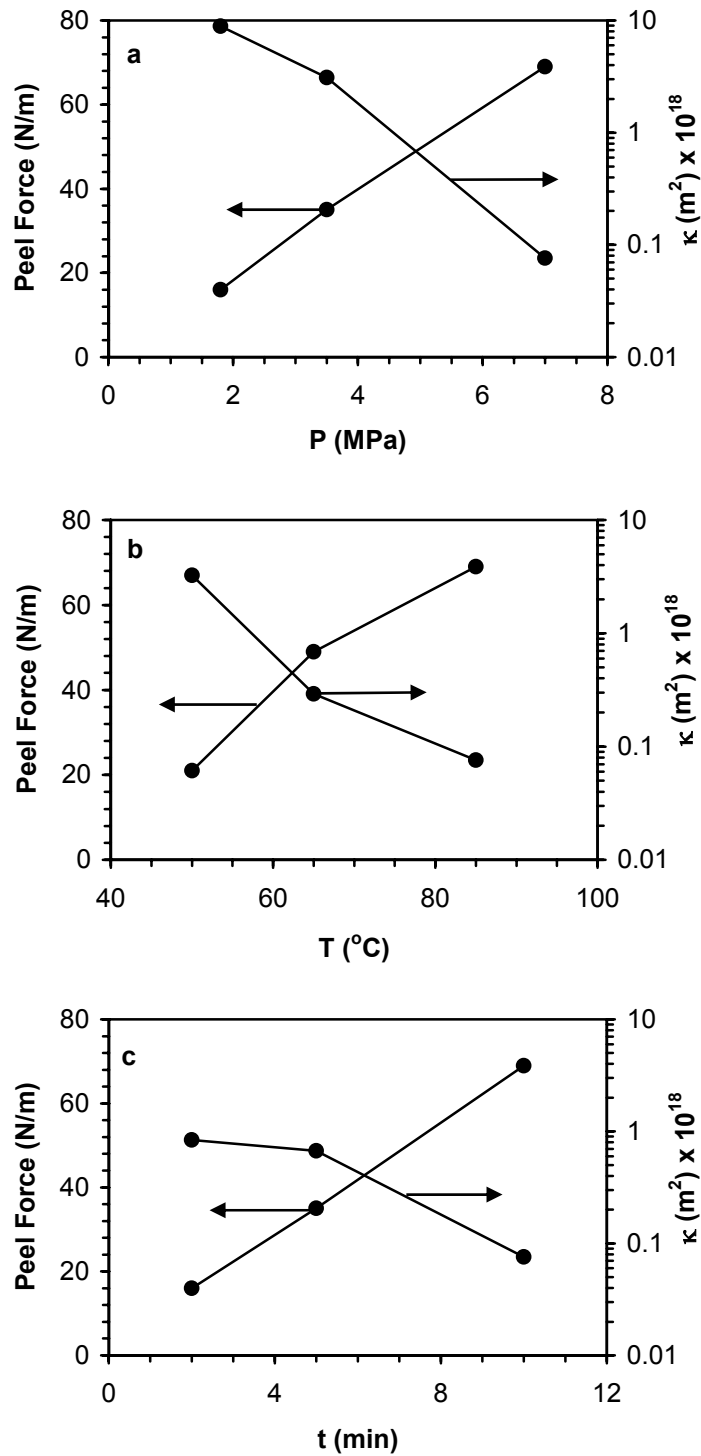
Figure 5. 9 Average peel force and permeability for tapes laminated at a) different pressures at 85°C for 10 min, b) at different temperatures at 7 MPa for 10 min, and c) at different times at 7 MPa at 85 °C.

To test this idea of a trade-off between lamination conditions, binder removal cycle time, and yield from binder removal, multilayer ceramic bodies were prepared by stacking 20 tapes of 3×3 cm in size. The tapes were then laminated at three sets of conditions (see Table 5.1), where Condition A corresponds to the most aggressive conditions for achieving high adhesion strength and low permeability. Conversely, Condition C represents lamination settings for obtaining low adhesion strength and high permeability, whereas Condition B is intermediate between Conditions A and C.

Table 5. 1   Lamination conditions for multilayer ceramic structures

Conditions	Pressure MPa	T ^{o}C	t min
A	7	85	10
B	3.5	65	5
C	1.8	50	2

Following lamination, substrates of size in 2×2×0.28 cm were cut from the center of the stacks. To determine process yield, samples laminated at Conditions A, B, and C were heated to 600°C and then held for 180 min. Six such experiments were conducted, in which the ramp rate to 600°C was varied from between 0.5 to 13°C/min. Table 5.2 contains the yield results from this study. At heating rates of 0.5-5°C/min, all of the samples survived. At heating rates above 5°C/min, samples laminated at Conditions A and B began to fail. At the highest heating rate of 13°C/min, all of the samples failed. A heating rate of 10°C/min represents the transition from survival to failure for all of the substrates examined here.

Table 5.2 also indicates the failure mode at each condition. For samples laminated at Condition A, which leads to high adhesion strength and low permeability, the failure mode was cracking and swelling, or in other words, the adhesion between layers was not the failure mechanism. For substrates laminated at conditions B and C, delamination became the failure mode, which is consistent with the less aggressive lamination conditions. These results suggest that beyond a threshold degree of lamination, less aggressive lamination may lead to increased process yield. Or in other words, the decrease in permeability obtained by laminating at more aggressive conditions is the more dominant factor in determining substrate yield during binder removal as compared to the adhesion strength.

Table 5. 2   Yield results and failure mode for substrates laminated at different conditions and then subject to different linear heating rates to 600°C.

Lamination	Heating Rates (^{o}C/min)					
Condition	0.5	1	5	10	10	13
A	OK	OK	OK	Fail swelling/crack	Fail swelling/crack	Fail cracked
B	OK	OK	OK	OK	Fail delamination	Fail delamination
C	OK	OK	OK	OK	OK	Fail delamination

In earlier work, we have examined how the permeability evolves as a function of binder loading for binder removed by air oxidation [25,26]. We thus show in Fig. 5.10 the adhesion strength versus binder loading of samples laminated at 7 MPa at 85°C for 10 min. The initial adhesion strength of the samples is approximately 25-30 N/m, and increases with decreasing binder loading to 50-60 N/m with removal of 25% of the initial

binder content.   Below 7.5 weight% binder, the samples were too brittle to test.   The

increase in adhesion strength with decreasing binder loading is somewhat surprising, but

the number of samples tested in Fig. 5.10 indicates that the trend is real.   One possible

explanation is that as binder is removed by thermal decomposition, bonds in the polymer

are broken, and new bonds may also form in and between the remaining polymeric

species and the ceramic particles.   These new bonds are likely to be of a chemical nature,

and thus may be stronger than the more physical types of interactions arising from the

lamination process.
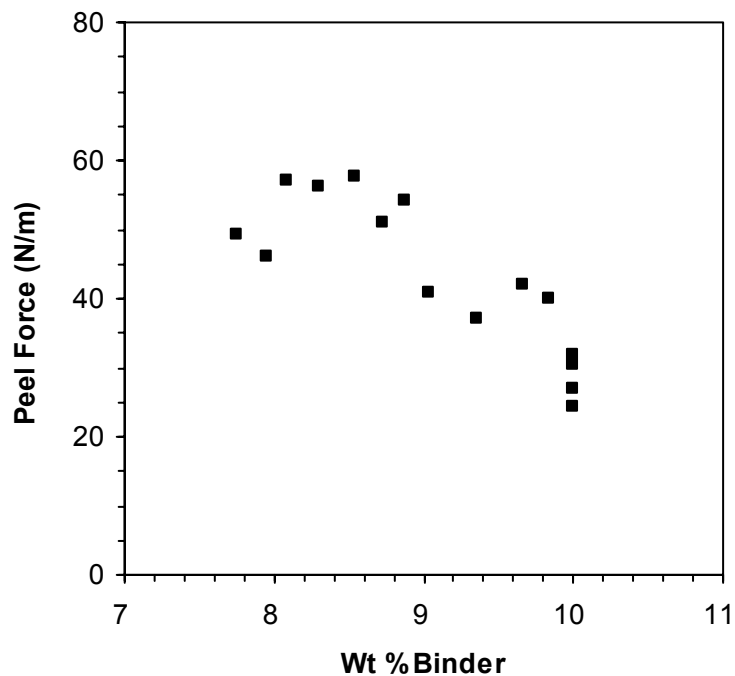
Figure 5. 10   Adhesion strength of two tapes versus binder loading laminated at 7 MPa at 85°C for 10 min.

5.4   CONCLUSIONS

The permeability and adhesion strength of laminated green tapes has been determined.   With increasing lamination conditions of time, temperature, and pressure, the permeability decreases whereas the adhesion strength increases, thus indicating a trade-off between these two properties and the lamination processing conditions.   This trade-off was also evident in the yield of layered samples subjected to different lamination conditions.

5.5　　REFERENCES

1. A. E. Scheidegger, *The physics of flow through porous media*, University of Toronto Press, Toronto (1974).

2. F. A. L. Dullien, *Porous media, fluid transport and pore structure*, Academic Press, New York (1979).

3. J. Bear and J.-M. Buchlin, *Modelling and applications of transport phenomena in porous media*, Kluwer Academic Publishers, Dordrecht (1991).

4. M. Sahimi, *Flow and transport in porous media and fractured rock,* VCH, Weinheim, (1995).

5. P. C. Carman, *Flow of gases through porous media*, Academic Press, NY (1956).

6. H. David, "A Review of Terminology Pertaining to Darcy's Law and Flow through Porous Media," *Journal of Porous Media*, **6** [2] 87-97 (2003).

7. M. D. M. Innocentini, A. R. F. Pardo, V. R. Salvini, and V. C. Pandolfelli, "How Accurate is Darcy's Law for Refractories," *Am. Ceram. Soc. Bull.*, **78** [11] 64-68 (1999).

8. M. D. M. Innocentini, and V. C. Pandolfelli, "Permeability of Porous Ceramics Considering the Klinkenberg and Inertial Effects," *J. Am. Ceram. Soc.,* **84** 941-44 (2001).

9. M. D. M. Innocentini, A. R. F. Pardo, and V. C. Pandolfelli, "Modified pressure-decay technique for evaluating the permeability of highly dense refractories," *J. Am. Ceram.* Soc., **83,** [1] 220-22 (2000).

10. G. P. Brown, A. DiNardo, G. K. Cheng, and T. K. Sherwood, "The Flow of Gases in Pipes at Low Pressures," *J. Appl. Phys.,* **17**, 802-813 (1946).

11. D. S. Scott and F. A. L. Dullien, "Diffusion of Ideal Gases in Capillaries and Porous Solids," *AIChE J.*, **8** [1] 113-117 (1962).

12. D. S. Scott and F. A. L. Dullien, "The Flow of Rarefied Gases," *AIChE J.*, **8** [3] 293-297 (1962).

13. N. Wakao and J. M. Smith, "Diffusion in Catalyst Pellets," *Chem. Eng. Sci.*, **17**, 825-834 (1962).

14. N. Wakao, S. Ontani, and J. M. Smith, "Significance of Pressure Gradients in Porous Materials: Part 1. Diffusion and Flow in Fine Capillaries," *AIChE J.*, **11** [3] 435-439 (1965).

15. S. Ontani, N. Wakao, and J. M. Smith, "Significance of Pressure Gradients in Porous Materials: Part 2. Diffusion and Flow in Porous Catalysts," *AIChE J.*, **11** [3] 439-445 (1965).

16. B. A. Meyer, and D. W. Smith, "Flow through Porous Media: Comparison of Consolidated and Unconsolidated Materials," *Ind. Eng. Chem. Fundam.*, **23**, 360-68 (1985).

17. H. Zhou, "Interlayer Delamination and Adhesion of Coextruded Films," *J. of Appl. Polymer. Sci.* Vol. **92**, 3901-3909 (2004).

18. H. H. Shih and G. R. Hamed, "Peel Adhesion and Viscoelasticity of Poly(ethylene-*co*-vinyl acetate)-Based Hot Melt Adhesion. I. The Effect of Tackifier Compatibility," *J. of Appl. Polym. Sci.* Vol. **63**, 323-31 (1997).

19. M. Fujita, M. Kajiyama, A. Takemura, H. Ono, H. Mizumachi and S. Hayashi, "Effect of Miscibility on Peel Strength of Natural-Rubber-Based Pressure-Sensitive Adhesives," *J. of Appl. Polym. Sci.* Vol. **70**, 777-84 (1998).

20. S. A. Uhland, R. K. Holman, S. Morissette, M. J. Cima, E. M. Sachs, "Strength of Green Ceramics with Low Binder Content," *J. Am. Ceram. Soc.,* **84** [12] 2809-18 (2001).

21. "Standard Test Method for Peel Resistance of Adhesives (T-Peel Test)" *ASTM* Designation: D 1876-01.

22. "Standard Test Method for Peel or Stripping Strength of Adhesive Bonds" *ASTM* Designation: D 903-98.

23. J. W. Yun and S. J. Lombardo, "Fluxes from Slip, Knudsen, and Poiseuille Flow in Narrow Capillaries," MS & T 2006 Conference, Cincinnati, OH., Oct. 15-19 (2006)

24. S. J. Lombardo, J. W. Yun, D. S. Krueger, P. J. Scheuer, "Permeability and adhesion measurements of laminated barium titanate green ceramic tapes," *Ceramic Transactions* 174 (Advances in Dielectric Materials and Electronic Devices), 305-

313 (2006).

25. J.W. Yun, S. J. Lombardo, "Permeability of Green Ceramic Tapes as a Function of Binder Loading," *J. of Am. Ceram. Soc.*, **90** [2], 456-461 (2007)

26. J.W. Yun, S. J. Lombardo, "Permeability of Laminated Green Ceramic Tapes as a Function of Binder Loading," to be submitted in *J. of Am. Ceram. Soc.* (2007)

CHAPTER 6

CONCLUSIONS AND FUTURE WORK

6.1 CONCLUSIONS

The flow of gases in narrow capillaries and porous media has been analyzed in terms of fluid transport models that describe Knudsen, slip, and Poiseuille flow. This analysis has described how the three flow mechanisms contribute to the total flux in porous media as the permeability evolves with binder volume loading. An approximate solution for determining the permeability was very accurate over a range of pore sizes as compared with the exact solution, especially at low pressure.

The permeability of unlaminated and laminated green ceramic tapes was determined as a function of binder loading for binder removed by air oxidation. The flow in porous media through the tapes was analyzed in terms of models for describing Knudsen, slip, and Poiseuille flow mechanisms. The characteristic pore sizes were between 1~2 μm for unlaminated green ceramic tapes and between 0.5~1 μm for laminated green ceramic tapes as a function of binder loading. Poiseuille flow was the dominant transport mechanism contributing to the flux for both the unlaminated and laminated green ceramic tapes. The permeability thus was determined from Darcy's law for flow in porous media. The permeability was also determined from microstructural features such as the specific surface, the pore fraction, and a parameter to account for tortuosity and constrictions. For laminated green ceramic tapes, the permeability also depends on the number of tapes laminated together.

The permeability and adhesion strength of green ceramic tapes were examined as a function of lamination time, temperature, and pressure. The permeability and the adhesion strength both strongly depend on all three variables of lamination. The

adhesion strength increases with increasing lamination conditions of time, temperature, and pressure, whereas the permeability decreased.

6.2   FUTURE WORK

Knowledge of the permeability in green ceramic tapes during binder removal is be very important, because the permeability strongly influences the way in which the products of binder degradation exit the green body and thus relieve the build-up of pressure.   With the help of this study, minimum time heating cycles for binder removal from green bodies can be determined more accurately in that as the binder decomposes and then exits the green body by convection through pores, the pore size increases, which leads permeability increases.

Using the techniques developed in this work, the permeability can also be determined in nanosized porous media, such as for $SrTiO_3$ based ceramic capacitors. For these smaller pore sizes, Knudsen flow may be the dominant transport mechanism contributing to the flux, and thus the equations presented in this work will need to be modified to account for this.

Finally, by optimizing the conditions of lamination, which affects the permeability directly, the thermal binder removal process can possibly be accelerated. This will result in saving energy and reducing process time, which are the ultimate goals of this study.

APPENDIX

EFFECT OF DECOMPOSITION KINETICS AND FAILURE

CRITERIA ON BINDER REMOVAL CYCLES FROM THREE-

DIMENSIONAL POROUS GREEN BODIES

A.1   INTRODUCTION

The development of heating cycles for the thermal removal of binder from porous green components is a difficult problem because of the coupled kinetic and transport phenomena which occur during the process [1-11].   In earlier work, we have developed a convective transport model to describe the pressure distribution in 3-D porous bodies during binder removal [12,13].   This transport model can then be combined with a variational calculus algorithm for specifying the minimum cycle time for binder removal [14,15].   The algorithm predicts that minimum time heating cycles are not a sequence of ramps and holds but rather are a continuous nonlinear increase in the temperature with time.   More recently, we have derived an analytic approximation that accurately describes the minimum time heating cycles [16].

To determine the minimum time heating cycles, a number of quantities must be specified in the model [15,16], and these include the rate law for binder decomposition and the conditions at which failure of the body occurs.   To determine the binder decomposition kinetics, we have demonstrated earlier how weight loss data, as obtained from a thermogravimetric analyzer (TGA), can be used to specify the kinetic parameters that appear in the rate law.   Although it is relatively straightforward to obtain values for the preexponential factor and the activation energy of decomposition that accurately describe the TGA data, the specification of a unique kinetic mechanism is more difficult [14,17,18].   In many instances, it may not be feasible or even possible to unambiguously determine the decomposition mechanism over the full range of binder loading.   In fact, a unique mechanism probably does not exist for many real binder systems, which are composed of multiple organic components with their own individual decomposition

behavior.   In addition, catalytic effects between the ceramic solid (and from metal layers for multilayer ceramic capacitors) also complicate the decomposition mechanism.   It is thus one aim of this work to show how the assumption of a kinetic mechanism for binder decomposition influences the predicted minimum time heating cycles.

Two other inputs into the model are the temperature and pressure at which failure occurs in the green body during the heating cycle.   Although stress ultimately causes failure within the green body, we have shown earlier how the stress within the body is related to the internal pressure within the porous compact [19].   A method is thus also described herein to determine the temperature and pressure at which failure occurs in the green body and what influence these parameters have on binder removal cycles.

A.2 EXPERIMENTAL

The materials used in this study are green tapes composed of $BaTiO_3$ powder (Tamtron® X7R 422H, Ferro Electronic Materials, Niagra Falls, NY), poly(vinyl butyral) (PVB) binder (Butvar B98, Richard E. Mistler, Inc., Yardley, PA), butyl benzyl phthalate plasticizer (Santicizer 160, Richard E. Mistler, Inc., Yardley, PA), and blown Menhaden fish oil (Z-3, Richard E. Mistler, Inc., Yardley, PA). The individual tapes, nominally 100 μm thick, were screen printed with a Pt paste (E1192, Ferro Electronic Materials, San Marcos, CA) at a thickness of nominally 5-10 μm. The tapes were then laminated into multilayer ceramic capacitors (MLCs) at 2-4 MPa and 80-85°C. To determine the kinetics of binder degradation, weight loss experiments were conducted in flowing air with a TGA.

A.3   MODEL

Because the model has been derived in detail elsewhere, we simply present here the important governing equations [15,16]. We specifically treat the thermal decomposition of binder in a 3-D porous medium of parallelepiped geometry where convective flow is the transport mechanism by which the product gases exit the body. We assume that (1) the temperature distribution in the body is uniform; (2) the viscosity, μ, of the gas is constant during the heating cycle; and (3) the dimensions, L_x, L_y, and L_z of the green body do not change during binder removal. Under these circumstances, the normalized maximum pressure occurs in the center of the body, *(P/P$_o$)$_o$*, and is given by [12,13]

$$\left(\frac{P}{P_o}\right)_o = \left(1 + 0.8365 \frac{1}{2\rho_o^2 \kappa} \frac{\mu}{R} \frac{r\rho_b}{M} \frac{T}{T_o^2} \frac{L_x^2 L_y^2 L_z^2}{L_x^2 L_y^2 + L_x^2 L_z^2 + L_y^2 L_z^2}\right)^{\frac{1}{2}} = \left(1 + G\frac{rT}{\kappa}\right)^{\frac{1}{2}} \qquad \text{A-1}$$

Equation A-1 thus describes the pressure in the center of the body in terms of the reaction rate, *r*, permeability, κ, temperature, *T*, and component dimensions. The quantity *G* in Eq. A-1, in light of the model assumptions, is a constant given by

$$G = 0.8365 \frac{\mu\rho_b}{2\rho_o^2 RMT_o^2} \frac{L_x^2 L_y^2 L_z^2}{L_x^2 L_y^2 + L_x^2 L_z^2 + L_y^2 L_z^2} \qquad \text{A-2}$$

where the other symbols are defined in the Nomenclature section.

The permeability, κ, in Eq. A-1 can be represented in terms of the porosity,   , by the Kozeny-Carmen equation as

$$\kappa = \frac{\varepsilon^3}{k(1-\varepsilon)^2 S^2} \qquad\qquad\qquad\qquad\qquad \text{A-3}$$

where k is the Kozeny-Carmen parameter and S is the surface area per unit volume. If slip flow prevails because of the pore size, then Eq. A-3 can be corrected to account for this.

The minimum cycle time, t^*, to remove binder from the green body can then be obtained from variational calculus as [16]

$$t^* = \frac{GT_s kS^2}{P_t^2 - 1} \times \left\{ \ln\frac{1-\varepsilon_s}{1-\varepsilon_s-\varepsilon_{b,o}} - 2\left[\frac{1}{1-\varepsilon_s-\varepsilon_{b,o}} - \frac{1}{1-\varepsilon_s} \right] + \frac{1}{2}\left[\frac{1}{\left(1-\varepsilon_s-\varepsilon_{b,o}\right)^2} - \frac{1}{\left(1-\varepsilon_s\right)^2} \right] \right\} \quad \text{A-4a}$$

$$= \frac{GT_s kS^2}{P_t^2 - 1} \times g(\varepsilon_b) \qquad\qquad\qquad\qquad \text{A-4b}$$

where $g(\varepsilon_b)$ is given by the term in braces in Eq. A-4a. The quantity T_s is the starting temperature for the binder removal cycle, and P_t, the threshold pressure, is the value of $(P/P_o)_o$ in Eq. A-1 corresponding to when failure in the body occurs. Equation A-4 is thus the approximate analytical solution for the minimum time for binder removal in terms of all of the dimensional and transport parameters appearing in the problem.

The minimum time in Eq. A-4 does not explicitly depend on the kinetic parameters of binder degradation such as the pre-exponential factor, A, and activation energy, E. As will be seen shortly, however, T_s, the starting temperature of the binder removal cycle, does depend on the specifics of the kinetic expression. The rate of binder decomposition, r, can be expressed as an activated process which depends on binder concentration, $f(\varepsilon_b)$, as

$$r = -\frac{d\varepsilon_b}{dt} = A\exp(-\frac{E}{RT})f(\varepsilon_b) \qquad\qquad\qquad \text{A-5}$$

To obtain the relationship of temperature versus time for the heating cycle, we first note that an equation of the form of Eq. A-4 can be used to represent the relationship between any time, t, and any volume fraction of binder, ε_b. The relationship between temperature, T, and ε_b, is then given by [16]

$$T(\varepsilon_b) = \frac{-E}{R}\left[\ln\frac{\kappa}{f(\varepsilon_b)}\frac{(P_t^2-1)}{GT_sA}\right]^{-1} \qquad\qquad \text{A-6}$$

The heating cycle $T(t)$ is thus determined via the common intermediate variable ε_b. Because different kinetic expressions will have different forms of $f(\varepsilon_b)$ and values of A and E, the heating cycles predicted by the variational calculus algorithm will depend on these quantities.

To complete the model description, we note that the porosity, ε, is related to volume fraction of solid, ε_s, as

$$\varepsilon = 1 - \varepsilon_s - \varepsilon_b \qquad\qquad\qquad \text{A-7}$$

Equations A-1 through A-7 thus constitute the model that will be evaluated here for predicting the minimum cycle time for binder removal. A number of parameters appear in these equations, and it is the aim of this work to demonstrate some important relationships between the kinetic, transport, and dimensional quantities that appear in the model.

A.4   RESULTS AND DISCUSSION

A.4.1   Kinetic Analysis of TGA Data

The weight loss of binder as a function of temperature is displayed in Fig. A.1 for three different heating rates.   At a heating rate of 5°C/min, two regions of rapid weight loss are evident.   As the heating rate in the TGA experiment is decreased, the weight loss profiles are shifted to lower temperatures and the regions of rapid binder degradation are seen to depend on the heating rate.   Thus, the TGA profiles are not directly useful for specifying heating rates and hold temperatures for binder removal cycles.
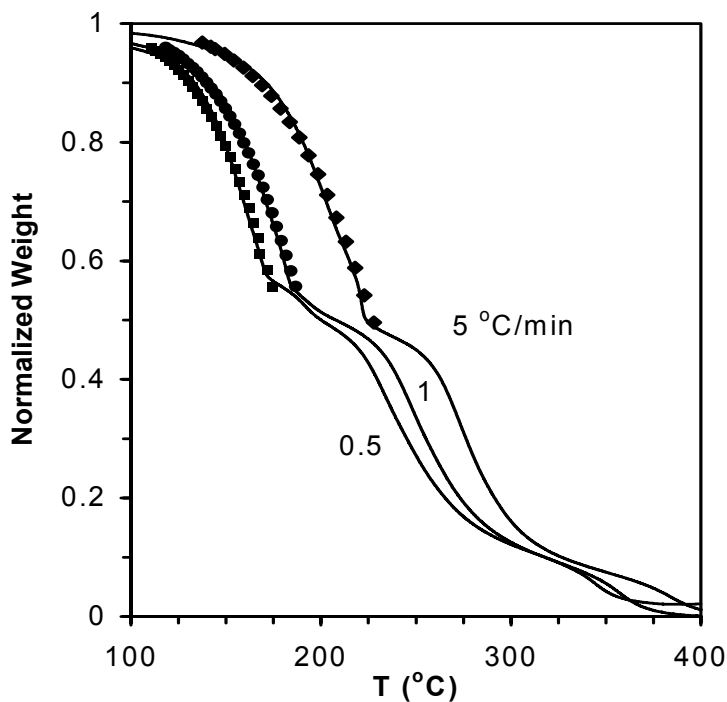
Figure A. 1   TGA weight loss data for a poly(vinyl butyral) and butyl benzyl phthalate binder in the presence of barium titanate and platinum metal heated at different linear heating rates in air.   The predicted kinetics with the first-order mechanism for the first region of decomposition are indicated by the symbols.

To determine values for A and E from the weight loss data in Fig. A.1, we assume or establish a decomposition mechanism as a function of binder concentration and then use an integral form of the kinetic expression. For a general kinetic process, $f(\alpha)$, where $\alpha = 1 - \varepsilon_b / \varepsilon_{b,o}$ is the fraction of reacted binder, the rate expression for a thermally activated process can be represented as

$$\frac{d\alpha}{dt} = A \exp\left[\frac{-E}{RT}\right] f(\alpha) \qquad\qquad \text{A-8}$$

For TGA experiments conducted with a constant heating rate, β, A and E can be determined from [20]:

$$\ln\left[\frac{F(\alpha)}{T^2}\right] = \ln\left[\frac{AR}{\beta(E + 2RT)}\right] - \frac{E}{RT} \qquad\qquad \text{A-9}$$

where $F(\alpha)$ is the integrated form of $f(\alpha)$. Many forms of $f(\alpha)$ and hence $F(\alpha)$ have been proposed [21,22]. Here, we examine first-order kinetics, for which $f(\alpha)=(1-\alpha)$ and $F(\alpha)=-ln(1-\alpha)$, and diffusion-controlled kinetics, for which $f(\alpha)=3(1-\alpha)^{1/3}/2[(1-\alpha)^{-1/3}-1]$ and $F(\alpha)=[1-(1-\alpha)^{1/3}]^2$.

The values of A and E determined from analysis of the TGA data with the two kinetic mechanisms are contained in Table A.1 along with the regression coefficients and the range of conversion evaluated. For each set of three heating rates, the values of A and E are similar, which suggests that the mechanism of decomposition is not changing over the range of heating rates examined here. Figure A.1 also shows the kinetics predicted for the first region of decomposition from the values of A and E for the first-order model. In general, the predicted kinetics agree quite well with the weight loss data recorded in the experiments; similarly good agreement was obtained when the

kinetics parameters determined from the diffusion mechanism were used. We note, however, that poorer agreement between the predicted and measured decomposition behavior is observed if the kinetic parameters obtained at one heating rate are used to predict the TGA data obtained at another heating rate [12].   In addition, the high level of agreement seen between the measured and predicted kinetics in Fig. A.1 arises in part because of the limited conversion range over which the data are fitted, and this point has been discussed in more detail elsewhere [18].   Although, based on these results, we cannot definitively conclude which mechanism is better for representing the actual binder decomposition process, we will next address the ramifications of utilizing one kinetic expression versus the other.

Table A. 1   Kinetics parameters, regression coefficients, and range of conversion determined from the first region of weight loss at different heating rates for barium titanate, platinum metal, and poly(vinyl) butyral and dibutyl phthalate binder using first-order and diffusion-controlled mechanisms.

	β (°C/min)	E (kJ/mol)	A (s^{-1})	R^2 (-)	$1-\alpha$ (-)
	0.5	54	2.68×10^2	0.99	0.95~0.56
First Order	1	52	2.43×10^2	0.99	0.95~0.55
	5	51	3.39×10^2	0.99	0.96~0.48
	0.5	118	1.20×10^9	1.00	0.94~0.52
Diffusion	1	109	9.13×10^7	0.99	0.96~0.54
	5	102	7.56×10^6	0.99	0.98~0.50

A.4.2 Determination of Failure Temperature and Threshold Pressure

During heating cycles for binder removal, the decomposition of binder leads to pressure within the green body, and, depending on the kinetics of decomposition, possibly to failure of the body. One important input to the model is thus the threshold pressure, P_t, which corresponds to the pressure in the center of the body at failure. To the best of our knowledge, no method has been reported on measuring the failure pressure within a porous body, especially for the case where the average pore size is less than 1 μm. To circumvent this difficulty, we have developed a procedure to obtain a value for P_t in the following manner. Components of parallelepiped geometry are subjected to rapid linear heating rates. During the course of the rapid heating cycle, we visually monitor the sample and record the temperature, T_f, at which failure occurs. To determine P_t, we then use Eqs. A.1, A.3, A.5, and A.7 with the known heating rate and calculate $(P/P_o)_o$ as a function of temperature. In performing this calculation, however, we need to assume a decomposition mechanism with associated values of A and E.

Figure A.2 shows the results of this type of calculation for the pressure in the center of the body as a function of temperature when components of cube geometry are heated with a linear heating rate of 5°C/min. The model parameters used for these simulations are in Table A.2 along with the kinetic constants for two decomposition rate laws. As the temperature is ramped, the rate of decomposition increases, and thus the pressure increases and then goes through a maximum as binder is consumed and the body becomes more permeable. The pressure continues to decrease as binder is consumed and the pore space becomes more open. The model parameters used for these simulations are in Table A.2 along with the kinetic parameters for two decomposition rate

laws. These parameters were obtained by simulating TGA data with a first-order mechamism at a heating rate of $1^oC/min$ with $A=200s^{-1}$ and $E=95kJ/mol$ and then analyzing it with first-order and diffusion-controlled mechanisms.   As also seen in Fig. A.2, the pressure profiles determined at a heating rate of $5^oC/min$ from the two kinetic mechanisms differ, and this occurs because the rates predicted by the two mechanisms are slightly different at each temperatures at which the data were analyzed versus the temperature at which they are simulated, i.e., as the difference in the heating rates increases.
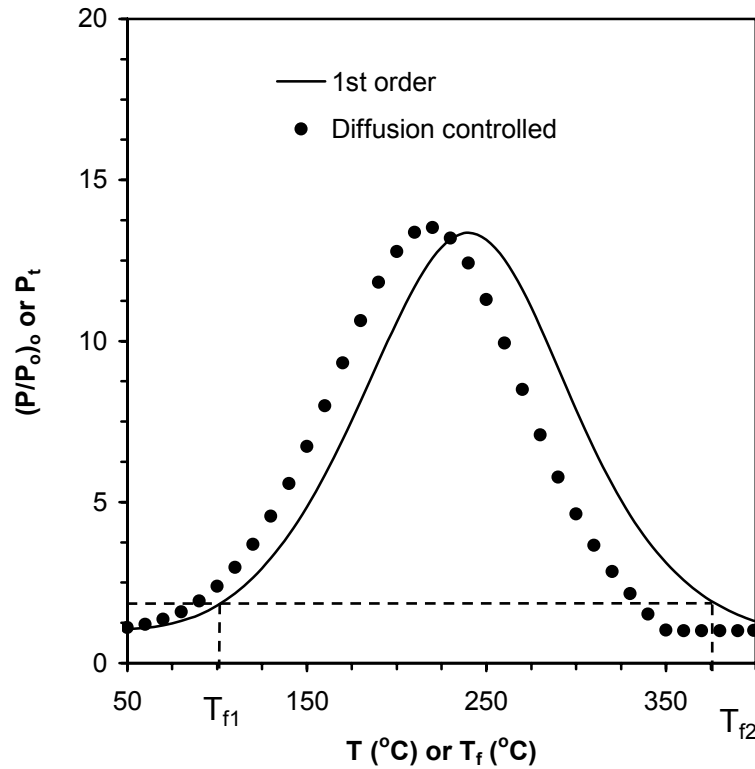
Figure A. 2   The normalized pressure in the center of the body, $(P/P_o)_o$, versus temperature as determined from the model for first-order and diffusion-controlled decomposition kinetics with a heating rate of 10°C/min.   The procedure used to determine failure pressure, P_t, for an observed failure temperature, T_f, for first-order kinetics is also shown.

Table A. 2 Parameters used in the simulations to determine the effect of decomposition kinetics on the minimum cycle times for binder removal.

Symbol (units)	For simulations in Figs. A.2-5		For simulations in Figs. A.7 and A.8
Kinetics	First order	Diffusion	First Order
A (s^{-1})	2.56×10^2	5.9×10^7	2.5×10^3
E (J/mol)	55,061	122,465	68,000
$\varepsilon_{b,o}$ (-)	0.4	0.39995	0.4
ε_s (-)	0.5		0.5
S (m^{-1})	5.0×10^6		2×10^7
L_x (m)	0.01		varies
L_y (m)	0.01		varies
L_z (m)	0.01		varies

Also indicated in Fig. A.2 is that an observed failure temperature of $T_f = 80°C$ corresponds to a threshold pressure of $P_t = 1.31$ for first-order kinetics. With the assumption of diffusion-controlled kinetics, however, the profile of $(P/P_o)_o$, with temperature is different from the first-order case and the value of P_t is now 1.59. The absolute values of P_t thus depend on the kinetic model and for a fixed temperature can differ by up to 25% for the cases examined. We also note that for the case of assumed first-order decomposition with a failure pressure of $P_t = 1.31$, a second temperature exists to the right of the maximum in pressure at which failure may occur, namely at $T_f = 399°C$. Obviously, however, if a body fails at the lower temperature, then the second temperature of failure is not particularly meaningful. This example does indicate, however, that if a green body can survive failure at low temperature for a specific pressure, where the body is full of binder and relatively strong, then it may still fail later in the heating cycle, when the green body contains less binder and hence is weaker.

The above procedure indicates how observation of T_f can be used, with an assumed kinetic model, to determine P_t. Figure A.2 can thus also be interpreted as indicating how threshold pressure varies with T_f, which is explicitly shown in Fig. A.2 with the alternate axis labels T_f and P_t.

A.4.3 Effect of Kinetics on Binder Removal Cycles for Components of Fixed Size

The effects of assuming a kinetic mechanism on the predicted rapid binder removal cycles can now be examined. Because the cycle time is strongly dependent on P_t (see Eq. A.4), which in turn depends on T_f, different heating cycles can arise when first-order and diffusion-controlled mechanisms are used to describe the decomposition behavior. Figure A.3 shows the two minimum time heating cycles arising from use of the two different kinetic mechanisms (see Table A.2 for model parameters) for $T_f = 80°C$. Both cycles start at approximately the same value of T_s and have the same general shape with no hold periods but are of significantly different duration, with the heating cycle corresponding to the diffusion-controlled case being shorter by a factor of three in total time. This comparison indicates that both the assumption of a kinetic model and the establishment of the failure temperature can strongly influence the minimum cycle times for binder removal.

Because it is difficult to determine the failure temperature, it may be tempting in practice to simply assume a failure pressure P_t. For the case of taking $P_t = 1.5$, this failure pressure corresponds to failure temperatures of $T_f = 89.8$ and $76.5°C$ for the first-order and diffusion-controlled kinetics, respectively. Figure A.4 shows the minimum

cycle times predicted for the two different kinetic models. Although the cycles exhibit

qualitatively similar behavior, T_s for the two cycles differs by 15°C.

Figure A. 3 **Temperature profiles with time determined by the variational calculus algorithm for first-order and diffusion-controlled kinetics for T$_f$=80°C**

A third option to determine the minimum time heating cycles is to assume a

constant value of T_s=80°C for the heating cycle, which for first-order and diffusion-

controlled kinetics implies failure pressures of P_f=1.31 and 1.86, respectively. Figure

A.5 shows that minimum time heating cycles predicted with the assumption of constant

T_s exhibit very nearly the same qualitative shape and relationship to the corresponding

curves in Fig. A.3. This arises because T_f and T_s can be close to each other in value, and

this will be explained in more detail in the next section.
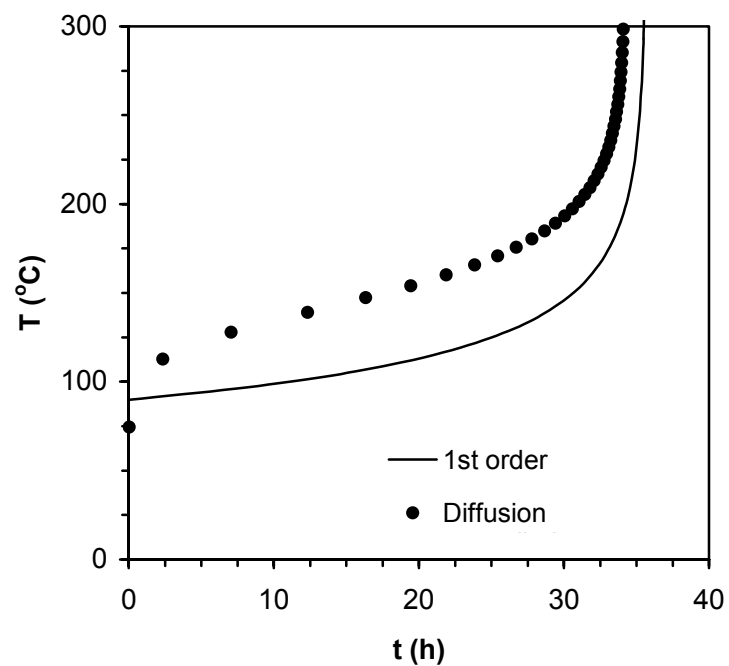
Figure A. 4 Temperature profiles with time determined by the variational calculus algorithm for first-order and diffusion-controlled kinetics for P_f=1.5

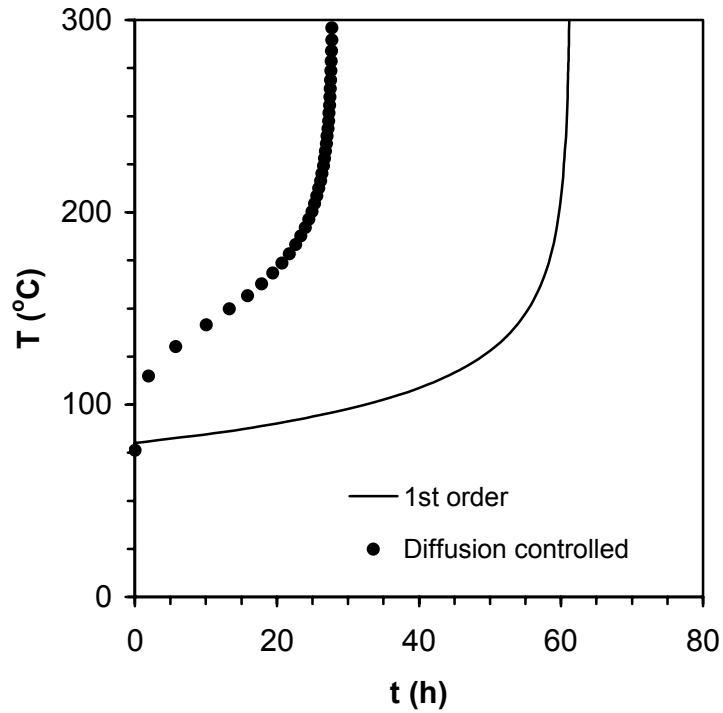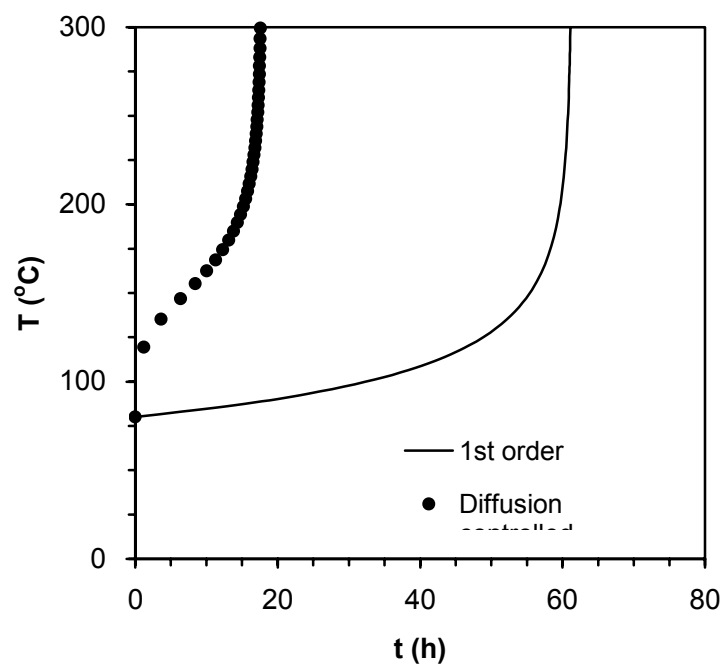**Figure A. 5 Temperature profiles with time determined by the variational calculus algorithm for**

first-order and diffusion-controlled kinetics for $T_s=80^oC$

To summarize this section, we note that the discrepancy in the decomposition behavior arising from the two different kinetic mechanisms may lead to different minimum time binder removal cycles. When more accurate kinetic parameters and mechanisms are determined which are valid over a wider range of temperature, however, differences in the decomposition behavior with temperature and in the curves of $(P/P_o)_o$ in Fig. A.2 become less pronounced, which in turns leads to more similar behavior between the pairs of heating cycles in each of Figs. A.3, A.4, and A,5.

A.4.4   Effect of Component Size on Failure and on Binder Removal Cycles for Fixed Kinetics

The cases examined in Figs. A.2-5 treat a component of fixed size where both the kinetics and another parameter are varied in the model such as T_f, P_t, or T_s; the effect of assumption of a kinetic mechanism is then examined on the predicted binder removal cycles. We now examine the effect of body size on failure criteria and thus on the resulting predicted binder removal cycles.

Table A. 3   Summary of failure temperatures for MLC samples of different dimensions subjected to a linear heating rate of 8°C/min.

$L_x \times L_y \times L_z$ (cm)	$T_f(^oC)$
1×1×0.24	147±3
2×2×0.24	132±3
3×3×0.24	123±3
4×4×0.24	115±3

MLC, multilayer ceramic capacitor.
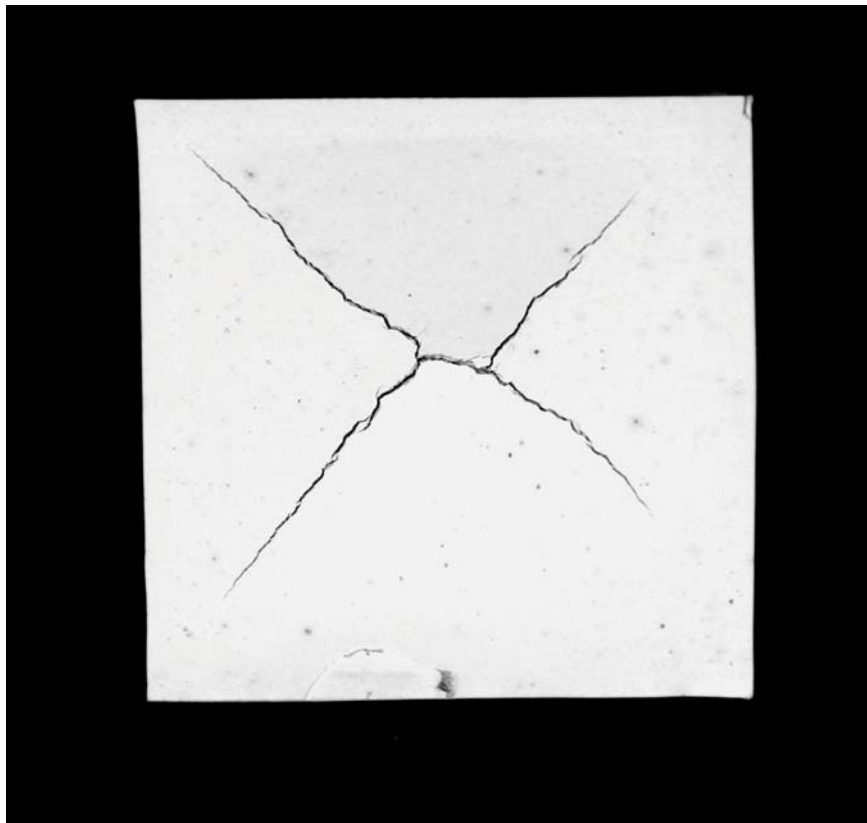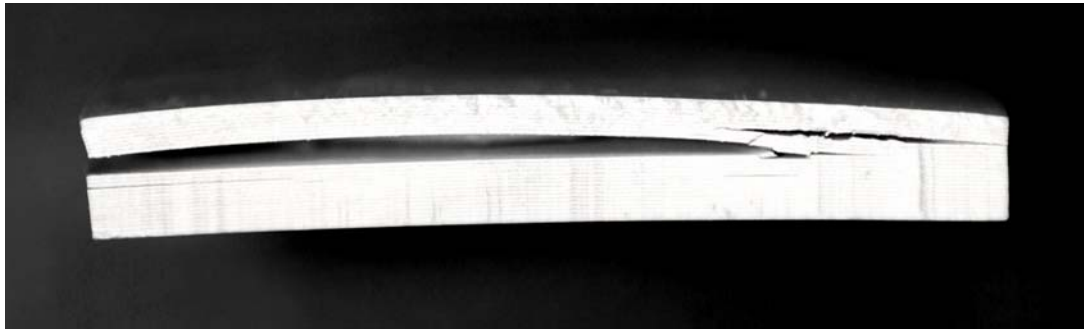
Figure A. 6   Photos of multilayer ceramic capacitors. The sample on the top failed by delamination.

The sample in the middle failed by bloating and the image on the bottom shows the cross-sectional view of the interior of the bloated sample.

For MLC samples heated at 8°C/min, the failure mode typically appeared as surface bloating or delamination in the center region, as seen in Fig. A.6. The cross-sectional view in Fig. A.6 indicates, however, that the apparent surface bloating originates in fact from the core of the sample, which is where the transport model predicts the maximum pressure will occur [12] and where the mechanics model predicts the maximum stress will occur [19]. Table A.3 shows how the failure temperature varies with size of the MLC components. As the component size increases, T_f decreases; the dominant failure mode of bloating or delamination originating from the sample core, however, remains the same. The experimental results suggest that the temperature of failure is not unique for a given ceramic-binder system but rather depends on the dimensions of the body.

The effect of component size on the evolution of pressure within the center of the green body for first-order decomposition kinetics (see Table A.2) is shown in Fig. A.7. The pressure evolution is directly proportional to the size of the component, which can also be seen from Eq. A.1 via the quantity G. In general, we can expect three simple types of behavior between the threshold pressure, P_t, and the dimensions of the body: a) P_t decreases with increasing component size, b) P_t is independent of the component size, or c) P_t increases with increasing component size. These different cases are schematically indicated in Fig. A.7 by the labeled solid lines. For these three cases of assumed failure versus component size, different relationships between P_t, T_f, T_s, and t^* are obtained depending on whether the body fails when it is highly loaded with binder,

i.e., on the left-hand side (LHS) of the maxima in pressures in Fig. A.7 or when the body contains less binder, *i.e.*, on the right-hand side (RHS) of the maxima.
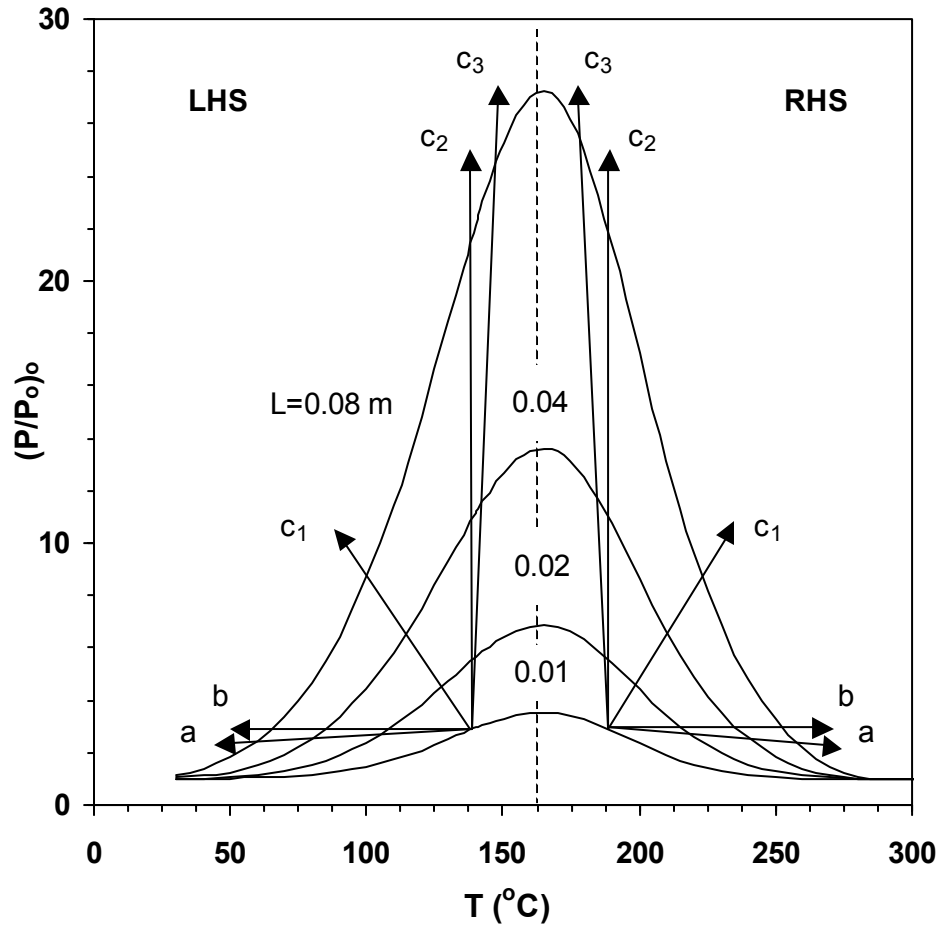
Figure A. 7 **Pressure profiles for cube shaped-components of different dimensions subjected to a linear heating rate of 10°C/min. The diagram is divided into left and right-hand sides and *cases a-c* indicate how the failure temperature and pressure vary with component size.**

Table A.4 shows these relationships of how P_t, T_f, T_s, and t^* vary for the three cases of how P_t depends on component size. For *case a* on the LHS of Fig. A.7, where P_t decreases with increasing component size, T_f also decreases with increasing component size; this is the behavior that was observed for the MLC components in Table

A.3.   Table A.4 also shows that the duration of the minimum time heating cycles, t^*, are longer with increasing component size for *case a*, which is thus in accord with the widely held physical expectation that larger components require longer binder removal cycles. Figure A.8 shows the minimum time heating cycles for components of different size predicted by the variational calculus algorithm for *case a*, which is the case for the failure behavior observed for the MLC components in Table A.3.   In general, the cycles have similar shapes with no temperature holds; each cycle, however, has a different start temperature.
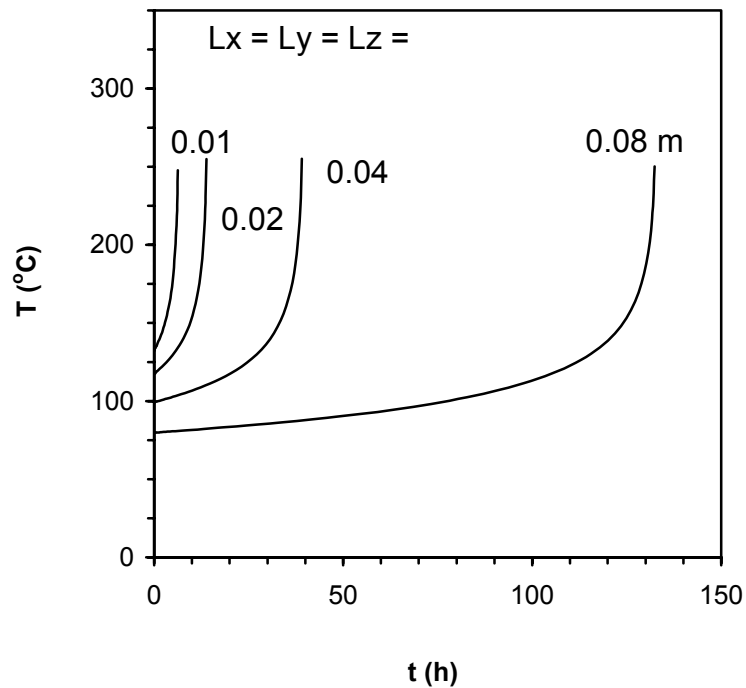
Figure A. 8 Temperature profiles with time determined by the variational calculus algorithm for first-order kinetics for case a, where Tf decreases with increasing component size. The body dimensions Lx=Ly=Lz (m) are indicated

For *case b* on the LHS of Fig. A.7, where P_t is independent of component size, T_f also decreases with increasing size of component.   Table A.4 again shows that the

minimum cycle times are longer for larger components, which again is consistent with the idea that larger bodies require longer cycle times for binder removal.

Table A. 4   Summary of relationships between P_t, T_f, T_s, and t^* as a function of component size and whether the body fails on the left-hand side or right-hand side of Fig. A.7

Case	$L_x=L_y=L_z$ (m)	P_t (-)	Left-Hand Side (LHS)			Right-Hand Side (RHS)		
			T_f ($^{\circ}$C)	T_s ($^{\circ}$C)	t^* (h)	T_f ($^{\circ}$C)	T_s ($^{\circ}$C)	t^* (h)
	0.01	3.00	141.5	133.6	6.3	186.7	133.6	6.3
a	0.02	2.80	106.8	105.8	27.3	217.3	105.8	27.3
	0.04	2.60	81.5	81.3	121.1	239.6	81.3	121.1
	0.08	2.40	59.5	59.4	549.8	257.8	59.4	549.8
	0.01	3.00	141.5	133.6	6.3	186.7	133.6	6.3
b	0.02	3.00	109.6	108.5	23.5	214.8	108.5	23.5
	0.04	3.00	86.4	86.2	88.4	235.2	86.2	88.4
	0.08	3.00	66.4	66.4	334.0	252.5	66.4	334.0
	0.01	3.00	141.5	133.6	6.3	186.7	133.6	6.3
c_1	0.02	4.72	130.0	125.8	9.2	197.1	125.8	9.2
	0.04	6.76	116.0	114.2	17.1	209.3	114.2	17.1
	0.08	8.93	101.0	100.4	37.4	222.3	100.4	37.4
	0.01	3.00	141.5	133.6	6.3	186.7	133.6	6.3
c_2	0.02	5.75	141.5	133.6	6.3	186.7	133.6	6.3
	0.04	11.36	141.5	133.6	6.3	186.7	133.6	6.3
	0.08	22.66	141.5	133.6	6.3	186.7	133.6	6.3
	0.01	3.00	141.5	133.6	6.3	186.7	133.6	6.3
c_3	0.02	5.80	142.1	133.9	6.1	186.2	133.9	6.1
	0.04	11.65	143.2	134.6	6.0	185.2	134.6	6.0
	0.08	23.97	145.5	135.8	5.6	183.1	135.8	5.6

For *case c* on the LHS of Fig. A.7, where P_t increases with increasing component size, three sub cases are evident. For *case c_1*, T_f decreases with increasing size of component and t^* (see Table A.4) increases with increasing component size, which is

again consistent with widespread expectation. *Case c_2* corresponds to a very special case in that the threshold pressure increases with increasing size in such a manner that the failure temperature is constant. For this case, minimum time heating cycles are independent of the component size. Although this latter relationship between size and cycle time is not consistent with the belief that larger bodies require longer cycle times, the type of analysis presented in Fig. A.7 may be valid for bodies in which failure arises from surface defects, such as blisters. Although such behavior was not observed for the MLC samples examined here, components highly loaded with binder may fail by such a mechanism. In such instances, adjusting the binder removal cycle to avoid surface defects may lead to heating cycles that do not depend as strongly on component size.

For the final *case c_3* on the LHS of Fig. A.7, where both P_t and T_f increase with increasing component size, Table A.4 shows that the minimum cycle time for binder removal decreases with increasing body size. This behavior is opposite to larger components requiring longer cycle times.

Cases a-c, including sub-cases, can also be examined for the RHS of Fig. A.7, where the body contains less binder; the values of P_t, T_f, T_s, and t^* for these cases are contained in Table A.4 and summary of the relationships is contained in Table A.5. For *cases a, b,* and c_1, T_f increases with increasing component size and t^* also increases with increasing component size, which is again in accord with expectation. Once again, however, *cases c_2* and c_3 lead to behavior in t^* versus component size that is not consistent with preconceived notions of how the time for binder removal varies with component size.

To summarize this section, we note that Fig. A.7 and Table A.5 illustrate in compact fashion some complicated, and not entirely expected, relationships between body size and failure temperature, failure pressure, and cycle time. In this work and in earlier work by us [9], we have noted that green bodies fail during binder removal relatively early in the heating cycle, when the green body still retains a significant amount of binder. Thus, failure seems to occur more frequently during the part of the binder removal cycle corresponding to the LHS of Fig. A.7, where the permeability in the body is low but the green strength is relatively high. This may be a general observation in the tradeoff between permeability and green strength, in that a higher frequency of failure for bodies with high green strength and low permeability was also observed when green bodies where subject to rapid depressurization from the conditions of supercritical extraction [23].

Table A. 5   Summary of threshold pressure, failure temperature, and minimum cycle time with increasing size of component.

Case	Left-Hand Side (LHS)			Right-Hand Side (RHS)	
	With ↑ size, P_t,	With ↑ size, T_f,	With ↑ size, t^*	With ↑ size, T_f,	With ↑ size, t^*
a	P_t ↓	T_f ↓	t^* ↑	T_f ↑	t^* ↑
b	P_t is constant	T_f ↓	t^* ↑	T_f ↑	t^* ↑
c1	P_t ↑	T_f ↓	t^* ↑	T_f ↑	t^* ↑
c2	P_t ↑	T_f is constant	t^* is constant	T_f is constant	t^* is constant
c3	P_t ↑	T_f ↑	t^* ↓	T_f ↓	t^* ↓

Case a-c are also indicated in Fig. A.7 and depend on whether failure on the left- or right-hand side of the diagram. The cycle time for binder removal for case c2 and c3 are inconsistent with the expectation that longer times are required for larger components.

The data in Table A.4 contain a number of relationships between P_t, T_f, T_s, and t^*,

one of which is that for failure early in the heating cycle, *i.e.*, on the LHS of Fig. A.7, start temperatures tend to be just slightly below failure temperatures, as given by $T_f \approx T_s + \delta$, where δ is a relatively small positive number.   To represent this mathematically, we first note that for a given heating cycle, the relationship between P_t and T_f can be expressed by rewriting Eq. A-1 as

$$P_t = \left(1 + G \frac{r_f T_f}{\kappa_f} \right)^{\frac{1}{2}} \qquad\qquad \text{A-10}$$

where the subscript f denotes the value of the quantity at T_f, the failure temperature.   We can then use Eq. A-6 to obtain a relationship between T_s and T_f for a body of a certain size as

$$\frac{1}{T_f} - \frac{1}{T_s} = -\frac{R}{E} \ln\left[\frac{\kappa_f}{\kappa_s} \frac{f(\varepsilon_b)_s}{f(\varepsilon_b)_f} \frac{T_s}{T_f} \right] \qquad\qquad \text{A-11}$$

where the subscript s denotes the value of the quantity at T_s, the starting temperature. Because the first two ratios in the argument of the natural logarithm of Eq. A-11 must be slightly greater than unity as a consequence of the binder loading being relatively high early in the cycle, and because R/E is less than unity, then $T_f \approx T_s + \delta$ is valid early in the heating cycle, which is what is observed in Table A.4.

For failure during binder removal that occurs on the RHS of Fig. A.7, which corresponds to when more binder has been removed, Eq. A-11 indicates that the starting and failure temperatures will be further apart as compared to when failure occurs on the LHS of Fig. A.7.   This is also the behavior seen in Table A.4.

To see mathematically some of the other relationships in Table 4 between P_t, T_f,

T_s, t^*, and component size, we can evaluate the ratio of cycle times (see Eqs. A-4 and A-10) for two bodies of different sizes, denoted by subscripts 1 and 2. After cancellation of common terms, the ratio of cycle times becomes

$$\frac{t_1^*}{t_2^*} = \frac{T_{s1}}{T_{s2}} \frac{\dfrac{r_{f2}T_{f2}}{\kappa_{f2}}}{\dfrac{r_{f1}T_{f1}}{\kappa_{f1}}} = \frac{T_{s1}}{T_{s2}} \frac{T_{f2}r_{f2}\kappa_{f1}}{T_{f1}r_{f1}\kappa_{f2}} \qquad \text{A-12}$$

which is only in terms of failure values and the ratio of cycle starting temperatures. We note that Eq. A-12 no longer contains the quantity G which explicitly accounts for the size of the component. To further simplify Eq. A-12, we express from Eqs. A-5 and A-6 the ratio of the start temperatures as

$$\frac{T_{s1}}{T_{s2}} = \frac{\kappa_{s1}r_{f1}T_{f1}r_{s2}\kappa_{f2}}{\kappa_{s2}r_{f2}T_{f2}r_{s1}\kappa_{f1}} \qquad \text{A-13}$$

Combination of Eqs. A-12 and A-13 then leads to

$$\frac{t_1^*}{t_2^*} = \frac{\kappa_{s1}}{\kappa_{s2}} \frac{r_{s2}}{r_{s1}} \qquad \text{A-14}$$

which is a relatively simple relationship between the ratio of the cycle times in terms of the starting permeabilities and the starting reaction rates at T_{si}. Because the starting permeability is independent of the body size, Eq. A-14 can be further simplified, and with the use of Eq. A-5, leads to

$$\frac{t_1^*}{t_2^*} = \exp\left[\frac{E}{R}\left(\frac{1}{T_{s1}} - \frac{1}{T_{s2}}\right)\right] \qquad \text{A-15}$$

Equation A-15 thus indicates that if the cycle start temperatures are equivalent, then the cycle times should be of the same duration, independent of body size, as is seen in Table A.4.

Because the starting and failure temperatures are related by Eq. A-11, the ratio of cycle times for two bodies of different sizes can now be written in terms of the quantities at failure as

$$\frac{t_1{}^*}{t_2{}^*} = \exp\left[\frac{E}{R}\left(\frac{1}{T_{f1}} - \frac{1}{T_{f2}}\right) + \ln\left(\frac{\kappa_{f1} f(\varepsilon_b)_{f2}}{\kappa_{f2} f(\varepsilon_b)_{f1}} \frac{T_{s1} T_{f2}}{T_{s2} T_{f1}}\right)\right] \qquad \text{A-16}$$

For bodies which fail early in the heating cycle, *i.e.*, on the LHS of Fig.A.7, the argument of the natural logarithm approaches unity and the ratio of cycle times is thus very approximately given as

$$\frac{t_1{}^*}{t_2{}^*} \approx \exp\left[\frac{E}{R}\left(\frac{1}{T_{f1}} - \frac{1}{T_{f2}}\right)\right] \qquad \text{A-17}$$

which is not directly dependent on the body size, but is dependent on the failure temperature, as is seen in Table A.4. For the special case of c_2 in Table A.4, where the failure temperatures of bodies of different sizes are the same, then the minimum cycle times for binder removal are equivalent, which suggests that the argument in the natural logarithm in Eq. A-16 is identically unity, and thus Eq. A-17 holds exactly. More generally, however, to rationalize the behavior of cycle times for the other cases in Tables A.4 and A.5, where T_f either increases or decreases with increasing component size, Eq. A-16 must be used.

To summarize this work, the specification of binder removal cycles is a difficult task because of the coupling of kinetic, transport, and stress phenomena, and this difficulty is exacerbated by the potential for spatial and temporal changes in important model parameters. For example, both the permeability and the rate of binder decomposition vary over orders of magnitude during the heating cycle, and therefore it is

difficult to ascertain definitively what model should be used and how the parameters appearing therein are to be determined. This work is thus part of a long term effort to make progress in the many different areas which are germane to binder removal.

This work further illustrates some heretofore unanticipated problems in specifying binder removal cycles. It is extremely challenging to determine unambiguously the mechanism of binder decomposition, especially for multicomponent binder blends when catalytic effects from the ceramic and metal electrode materials are operative. As demonstrated here, this ambiguity in the kinetics may lead to significant differences in the predicted minimum time heating cycles. The method of determining the failure temperature and pressures as a function of component size, as demonstrated in Fig. A-7, however, offers some relief in this regard.

Although we have successfully applied the binder removal methodology described herein to reduce the duration of heating cycles, routine application of the method is not yet possible. Unique specification of the decomposition mechanism is still unresolved, as is the evolution of the permeability with binder loading. Future work will thus be directed at these unresolved issues, in order to be able to practically and reliably utilize the proposed methodology for developing rapid cycles for binder removal.

A.5   CONCLUSIONS

The sensitivity for describing binder removal cycles of a previously developed model to kinetic parameters and to failure criteria has been examined.   The minimum time heating cycles depend on the kinetic mechanism and the activation energy and preexponential factor of binder decomposition.   Because it is difficult to ascertain unambiguously the decomposition mechanism, uncertainty is introduced into predicting the minimum time heating cycles.

Another important input into the model is the temperature at which failure occurs in the green body.   A limited amount of experimental data suggests that the failure temperature decreases with increasing size of the component.   A very general methodology has been presented to determine how the failure temperature, failure pressure, and cycle time are related.   This approach can then be used to rationalize under which circumstances the cycle time increases, decreases, or is independent of the component size.

A.6   NOMENCLATURE

A, preexponential factor

E, activation energy

f, as subscript, denoted quantity at the failure temperature

k, Kozeny-Carman parameter

L_i, $i=x,y,z$ dimensions of the body

M, average molecular weight of gas products

P, pressure

P_o, ambient pressure

P_t, threshold pressure in the center of the body

R, *gas constant*

r, rate of binder decomposition

S, surface area per unit volume

s, as subscript, denoted quantity at the start temperature

t, time

t^*, minimum cycle time for binder removal

T, temperature

T_o, initial temperature

T_s, starting temperature of binder removal cycle

α , binder conversion

β , heating rate

ε , porosity

ε_s , volume fraction of solid

ε_b , volume fraction of binder

$\varepsilon_{b.o}$, initial volume fraction of binder

ρ_b , binder density

ρ_o , initial gas density at T_o and P_o

κ , permeability

μ , gas viscosity

A.7   REFERENCES

1. R. M. German, "Theory of Thermal Debinding," *Int. J. Powder Metall.,* **23**, 237-245 (1987).

2. J. A. Lewis, "Binder Removal From Ceramics," *Annual Rev. Mater. Sci.*, **27**, 147-173 (1997).

3. P. Calvert and M. Cima, "Theoretical Models for Binder Burnout," *J. Am. Ceram. Soc.,* **73** [3] 575-579 (1990).

4. G. Y. Stangle, and I. A. Aksay, "Simultaneous Momentum, Heat and Mass Transfer With Chemical Reaction in a Disordered Porous Medium: Application to Binder Removal From a Ceramic Green Body," *Chem. Eng. Sci.,* **45**, 1719-1731 (1990).

5. D.-S. Tsai, "Pressure Buildup and Internal Stresses During Binder Burnout: Numerical Analysis", *AIChE J.,* **37**, 547-554 (1991).

6. S. A. Matar, M. J. Edirisinghe, J. R. G. Evans, and E. H. Twizell, "Effect of Porosity Development on the Removal of Organic Vehicle from Ceramic or Metal Moldings," *J. Mater. Res.,* **8**, 617-625 (1993).

7. J. H. Song, M. J. Edirisinghe, J. R. G. Evans, and E. H. Twizell, "Modeling the Effect of Gas Transport on the Formation of Defects during Thermolysis of Powder Moldings," *J. Mater. Res.,* **11**, 830-840 (1996).

8. A. C. West and S. J. Lombardo, "The Role of Thermal and Transport Properties on the Binder Burnout of Injection Molded Ceramic Components," *Chem. Eng. J.,* **71**, 243-252 (1998).

9. L. C.-K. Liau, B. Peters, D. S. Krueger, A. Gordon, D. S. Viswanath, and S. J. Lombardo, "Role of Length Scale on Pressure Increase and Yield of Poly(vinyl butyral)-Barium Titanate-Platinum Multilayer Ceramic Capacitors During Binder Burnout," *J. Am. Ceram. Soc.,* **83** [11] 2645-2653 (2000).

10. Y. Shengjie, Y.C. Lam, S. C. M. Yu, and K. C. Tam, "Two-Dimensional Simulation of Mass Transport in Polymer Removal from a Powder Injection Molding Compact by Thermal Debinding," *J. of Mat. Res.,* **16,** 2436-2451 (2001).

11. Y. Shengjie, Y.C. Lam, S. C. M. Yu, and K. C. Tam, "Thermal Debinding Modeling of Mass Transport and Deformation in Powder-Injection Molding Compact," *Metallurgical & Materials Transactions B-Process Metallurgy & Materials Processing Science,* **33**, 477-488 (2002).

12. S. J. Lombardo and Z. C. Feng, "Pressure Distribution during Binder Burnout in Three-Dimensional Porous Ceramic Bodies with Anisotropic Permeability," *J. Mat.*

Res., **17**, 1434-1440 (2002).

13. K. Feng and S. J. Lombardo, "Modeling of the Pressure Distribution in Three-Dimensional Porous Green Bodies during Binder Removal," *J. Am. Ceram. Soc.,* **86** [2] 234-240 (2003).

14. R. V. Shende and S. J. Lombardo, "Determination of Binder Decomposition Kinetics for Specifying Heating Parameters in Binder Burnout Cycles," *J. Am. Ceram. Soc.,* **85** [4] 780-786 (2002).

15. S. J. Lombardo and Z. C. Feng, "Determination of the Minimum Time for Binder Removal and Optimum Geometry for Three-Dimensional Porous Green Bodies," *J. Am. Ceram. Soc.,* **6** [12] 2087-2092 (2003).

16. S. J. Lombardo and Z. C. Feng, "Analytic Method for the Minimum Time for Binder Removal from Three-Dimensional Porous Green Bodies," *J. of Mat. Res.,* **18,** 2717-2723 (2003).

17. S. J. Lombardo and R. V. Shende, "Determination of Polymer Decomposition Kinetics to Specify Ramps and Holds for Binder Burnout Cycles for Multilayer Ceramic Capacitors"; pp. 23-31 in Ceramic Transactions, Vol. 131, *Advances in Dielectric Materials and Multilayer Electronic Devices, American Ceramic Society.* Edited by K. M. Nair, A. S. Bhalla, and S.-I. Hirano. American Ceramic Society, Westerville, OH, 2002.

18. S. J. Lombardo, J. W. Yun, and D. S. Krueger "The Influence of Binder Degradation Kinetics on Rapid Binder Removal Cycles"; pp. 191-204 in Ceramic Transactions Vol. 166, *Innovative Processing and Synthesis of Ceramics, Glasses, and Composites, VII.* Edited by N. P. Bansal. American Ceramic Society, Westerville, OH, 2004.

19. Z. C. Feng, B. He, and S. J. Lombardo, "Stress Distribution in Porous Ceramic Bodies During Binder Burnout," *J. of Appl. Mech.*, **69**, 497-501 (2002).

20. T. V. Lee and S. R. Beck, "A New Integral Approximation Formula for Kinetic Analysis of Nonisothermal TGA Data," *AIChE J.*, **30**, 517-519 (1984).

21. C. David, "Thermal Degradation of Polymers," pp. 1-173 in *Comprehensive Chemical Kinetics-Degradation of Polymers*, edited by C. H. Bamford and C. F. H. Tipper, Vol. 14, Elsevier, New York, 1975.

22. H. H. G. Jellinek, "Degradation and Depolymerization Kinetics," pp. 1-37 in *Aspects of Degradation and Stabilization of Polymers*, edited by H. H. G. Jellinek (Elsevier, NY 1978).

23. R. V. Shende, T. R. Redfearn, and S. J. Lombardo, "Defect Formation during Supercritical Extraction of Binder from Green Ceramic Components, *J. Am. Ceram.*

Soc., **87** [7] 1254-1258 (2004).

VITA

Jeong Woo Yun was born on August 22nd, 1975, in Mokpo, South Korea. After attending private high school, he attended Chonnam National University in Kwangju, Korea in 1994 and one year later he joined Korean army. In February 2002, he received a B.S. degree in Applied Chemical Engineering. In August 2002, he came to the University of Missouri-Columbia to pursue higher education. After studying and performing research for 5 years, he will a receive Ph.D. degree in Chemical Engineering and minor in Material Science in May 2007, upon approval of this dissertation. He will join a research group in University of Missouri-Rolla as a post-doctoral scholar.